Black-Hole Mass Measurements in Nearby Galaxies Using Molecular Gas Dynamics

Kyoko Onishi

DOCTOR OF PHILOSOPHY

Department of Astronomical Science
School of Physical Sciences
The Graduate University for Advanced Studies (SOKENDAI)

2016 (Academic Year)

学位論文

Black-Hole Mass Measurements in Nearby Galaxies Using Molecular Gas Dynamics

平成 29 年 1 月博士（理学）申請

総合研究大学院大学　物理科学研究科　天文科学専攻

大西　響子

Abstract

Galaxy evolution is one of the key topics in contemporary astronomy. Gaining a full understanding of it is however challenging, because of the myriad of processes involved. A key result of the 1990s was the realization that supermassive black holes (SMBHs; $M_{\rm BH} = 10^{6-10} M_\odot$) are present in the centres of massive stellar spheroids. More importantly, direct mass measurements of SMBHs in centres of galaxies have become gradually possible in these 2 decades, by using several dynamical methods thanks to both developed observing facilities and mass modelling methods. The derived SMBH masses are revealing a couple of empirical correlations between SMBH mass and host galaxy properties (e.g., stellar velocity dispersion σ km s^{-1}, thus $M_{\rm BH} - \sigma$ relation). The exact form of the correlation is still under debate, but its implication is clear – black holes and galaxies grow hand-in-hand, and the evolutionary process possibly involves a self-regulating mechanism. The idea is now broadly accepted (and debated) as a co-evolutionary process of galaxy and black hole, which has been motivating many theoretical and observational studies of galaxies from nearby to high redshift.

Dynamical measurements of SMBH masses in nearby galaxies have been reported so far, by using ionized gas, stars, and masers to trace the rotational motions in galaxies. We here report an establishment and applications of a new dynamical method uses molecular gas to trace the circular motion of a cold disc inside the galaxy. This new method was first used in 2013, which observed a CO ($J = 2 - 1$) disc in a nearby quiescent early-type galaxy. We first examine the method by using two different molecular species for a barred-spiral galaxy. Both of the molecular species, HCN ($J = 1 - 0$) and HCO$^+$ ($J = 1 - 0$), show very similar rotational motion that requires the same SMBH mass. We thus confirm

the flexibility of this method to use multiple molecular species and to target various types of galaxies.

We then extend this method to implement multiple parameters when fitting the model. So far in previous works SMBH mass and stellar mass-to-light ratio were the only free parameters to describe the mass model. We add free parameters to describe the properties of the disc and fit the model to a data cube of regularly rotating CO ($J = 2 - 1$) disc observed in a nearby early-type galaxy. The refinement on this method allows one to measure SMBH masses with less assumption, but with better confidence.

We then apply this method to another nearby galaxy imaged with a ~ 30 pc spatial resolution, three times as high as the first two. The molecular gas distribution in a form of a thick disc is newly considered to model a realistic gas disc in this spiral galaxy.

Results from our method are finally added to the empirical $M_{\rm BH} - \sigma$ relation. We comment that the results do not conflict with the existing relation, while the number of plots is too small to give a statistically meaningful conclusion. It is necessary to improve the statistics by investigating the origin of the scatter in order to discuss about the coevolutionary process from the $M_{\rm BH} - \sigma$ relation.

Unlike other dynamical methods, the molecular gas method provides a broad range of target galaxy types and SMBH masses. Moreover, gas kinematics sometimes can be observed with a surprisingly short integration time (only a few to several tens of minutes of on-source time for CO detection). We examine and confirm the capability of the molecular gas method to help dramatically increasing the sample for the $M_{\rm BH} - \sigma$ relation. The dynamical method will thus be a powerful tool to help understanding the key question about the co-evolutionary process of galaxy and black hole.

Contents

1 General Introduction **1**

1.1 Coevolution of Galaxy and Black Hole 1

1.1.1 Dynamical Evolution of Galaxy 2

1.1.2 Star Formation and its Quenching – Feedback Processes 3

1.1.3 Formation and Evolution of Black Hole 6

1.1.4 Correlations between SMBH Mass and Host Galaxy Properties . . 9

1.2 Supermassive Black Hole Mass Estimates 12

1.2.1 The nearest case – our galaxy 12

1.2.2 Dynamical modelling of nearby galaxies – megamaser systems . . 17

1.2.3 Dynamical modelling of nearby galaxies – stellar dynamcis . . . 19

1.2.4 Dynamical modelling of nearby galaxies – ionized gas dynamics . 20

1.2.5 Dynamical modelling of nearby galaxies – molecular gas dynamics 21

1.2.6 SMBH Mass Estimates at High Redshift 22

1.2.7 Cross Checks Between SMBH Mass Measuring Methods 24

1.3 Road Map 27

2 A Development of SMBH Mass Measuring Method **28**

2.1 Abstract of the Chapter 28

2.2 Introduction 29

2.2.1 The Target – NGC 1097 30

2.3 Observation 32

2.4 Method 35

2.4.1 Dynamical Modelling 35

2.4.2 Fitting and the Result 39

2.5 Discussion 41

2.5.1 The Proper Stellar Luminosity Profile without the Dust Effect . . 41

2.5.2 Effect from the Inclination Angle 45

2.5.3 SMBH Mass Estimation from Other Molecular Species 48

2.6 Conclusion 50

3 Some improvements on the method – application to NGC 3665 51

3.1 Abstract of this Chapter 51

3.2 Introduction 52

3.2.1 The target – NGC 3665 53

3.3 Observation and Data Reduction 54

3.4 Method 58

3.4.1 Velocity Model 58

3.4.2 Creating the Model Data Cube 61

3.4.3 Fitting 62

3.4.4 Results 64

3.5 Discussion 68

3.5.1 CO Morphology 68

3.5.2 AGN Properties 69

3.5.3 Other Error Sources for the SMBH Mass 70

3.5.4 Rotation Curve Fit 72

3.6 Conclusions 77

4 SMBH mass measurement in NGC 5064 **79**

4.1 Abstract of this Chapter 79

4.2 Introduction 79

4.2.1 The target – NGC 5064 80

4.3 Observations and Data Reduction 81

4.4 Method 83

4.4.1 The Mass Model 83

4.4.2 Velocity Model Calculation and the Result 83

4.5 Discussion – Velocity Dispersion of the Gas Disc 92

4.6 Conclusion 92

5 General Discussion – $M_{\mathrm{BH}} - \sigma$ Relation and Future Prospects **94**

6 General Conclusion **99**

Acknowledgment **101**

Bibliography **104**

Chapter 1

General Introduction

1.1 Coevolution of Galaxy and Black Hole

Galaxies are the main visible building blocks in the universe. Formation and evolution of those is thus crucial to understand the progression of the universe to date. Observations for over many decades and theoretical researches have been done to search for this major topic in contemporary astronomy, while gaining a full understanding is challenging because of the myriad of processes involved. A key result of the 1990s was the realisation that supermassive black holes (SMBHs; $M_{\rm BH} = 10^{6-10} M_{\odot}$) are present in the centres of most massive galaxies. Following the galaxy formation scenarios involving galaxy mergers, growth of the SMBH can be expected to proceed together with the galaxy evolution. The idea of the coevolutionary process is supported by some observed evidence such as relations between SMBH mass and properties of their host galaxy. Here I summarize a known scenario of galaxy evolution and the role of SMBH, studied both from observational and theoretical aspects.

1.1.1 Dynamical Evolution of Galaxy

The theory of cold dark matter (CDM; see, e.g., Peebles, 1982; Blumenthal et al., 1984) has nowadays become the most accepted explanation for the origin and evolution of the universe. A rough sketch of this scenario is that a density fluctuation in the early universe evolves into dense core of baryon, and then eventually consist stars and thus galaxies.

Navarro et al. (1997) numerically simulated the collapse and growth of dark matter halo to show the profile that can be written as in equation 1.1, regardless of dark matter mass, initial density fluctuation spectrum, or of cosmological parameters.

$$\rho(r)/\rho_{\rm crit} = \frac{\delta_c}{(r/r_s)(1+r/r_s)^2} \tag{1.1}$$

Here r_s is the scale radius, δ_c is the characteristic density, and $\rho_{\rm crit} = 3H^2/8\pi G$ is the critical density of the dark matter halo.

As the dark matter halos merge and form larger halos, baryons condense and provokes birth of dwarf galaxies at the centre of the halo. White & Rees (1978) analytically described a two-stage theory for galaxy formation and clustering. A density fluctuation in the gas cloud grows with an assumption of a self-similar clustering process. In this scenario, however, the clouds will be destroyed by relaxation effects and reform an amorphous system within a short time scale. This explain the needs of gas cooling and dissipation, so to remain some gas in the surrounding and eventually fuel the luminous inner part of galaxies as seen in nearby universe.

More realistic approaches are nowadays taken by using semi-analytic modelling (SAM; see, e.g., White & Frenk, 1991; Springel et al., 2005; Baugh, 2006; Croton et al., 2016, and references therein). This computationally inexpensive technique allows to include star formation, black hole growth, supernova feedback, active galactic nuclei (AGN) feedback and reionization process from the UV background radiation, in addition to the gas cooling in its model. N-body and hydrodynamic simulations also accurately compute the

galaxy formation process (see e.g., Somerville & Davé, 2015, for a review). Fundamental equations such as gravitation, hydrodynamics, radiative cooling and radiative transfer are normally considered to mitigate the assumption.

Although detailed formation and evolutionary process of galaxy is under debate, the implication is clear. Current universe cannot be explained with a mere dynamical collapse of a cloud. Additional effects such as gas cooling, feedbacks from inside and so on are crucial to reproduce the universe.

1.1.2 Star Formation and its Quenching – Feedback Processes

Aiming to shed light into the unknown process of galaxy formation and evolution, many studies have altogether revealed the importance of physical processes such as star formation and feedback processes. While the formation process itself cannot be directly observed, multi-wavelength observations allow us to study on galaxies at multiple distances, so as multiple ranges of their age.

Evolution of galaxy star formation rate density is one of the key findings in the past two decades (see, e.g., Madau et al., 1996; Hopkins & Beacom, 2006; Madau & Dickinson, 2014). The so-called Madau plot (see Figure 1.1) clearly shows the galaxy star formation to be very active at the epoch of redshift $z = 2 - 3$. In this "cosmic noon", the star formation rate density is ~ 10 times higher than at present. The low star formation rate density at $z > 3$ can be explained when considering dwarf galaxies that are dominant at the epoch. Supernova explosion can blow the gas with a galactic wind to expand the gas, so as the star formation becomes inefficient. In order to stop the star formation activity at $z < 2$, the system needs to eject or use up the gas before $z = 0$.

Possible explanations for the quenching are: 1). gas stripping due to ram pressure in galaxy clusters (see, e.g., Abadi et al., 1999; McCarthy et al., 2008; Tecce et al., 2010;

Guo et al., 2011; Heß & Springel, 2012; Steinhauser et al., 2016); 2). gas ejection by galactic wind from a supernova explosion (see, e.g., Arimoto & Yoshii, 1987; Hopkins et al., 2012); and 3). gas ejection due to the active galactic nuclei (AGN) feedback process (see, e.g., Silk & Rees, 1998; Di Matteo et al., 2005; Sijacki et al., 2007; Di Matteo et al., 2008; Fabian, 2012; Barai et al., 2013; Heckman & Best, 2014).

Ram pressure stripping is one of the most commonly accepted processes to explain observed variation of galaxy morphologies between cluster and field galaxies. The stripping process itself is observationally confirmed by tens of kpc tails associated to several cluster galaxies (e.g., Crowl et al., 2005; Vollmer et al., 2005; Sun et al., 2007). Numerous hydrodynamic simulations and semi-analytic modellings have been done, both focused on stripping of cold gas discs (e.g., Abadi et al., 1999; Tecce et al., 2010) and of hot gas haloes (e.g., McCarthy et al., 2008; Guo et al., 2011). Overall the ram pressure stripping explains the observed lower star formation rates in cluster galaxies compared to field galaxies, but obviously does not explain the star formation rate density evolution for galaxies regardless of their environment.

Galactic wind occurs when energy of supernova explosion exceeds the binding energy of the galaxy. The wind drives the gas out of the system to eventually quench the star formation. Arimoto & Yoshii (1987) calculated an evolution of spectra from elliptical galaxies with various mass by considering the galactic wind. They reported the wind helps to reproduce the trend of the observed colour-magnitude diagram, that the elliptical galaxies become redder for higher luminosity. In recent studies, supernovae do not only eject gas but recycle, photoheat, or photoionize the gas to slow down the star formation (but not to completely quench). These effects are altogether called as star-formation feedback or supernova feedback, that is well summarized in Hopkins et al. (2012). Hopkins et al. (2012) used numerical simulations of isolated galaxies and claimed that giant star-

forming clumps observed at high-redshift can be disrupted (as seen in low redshift), only when considering the stellar feedback mechanism. This feedback event can happen in every galaxy, while ram pressure stripping requires a specific environment. It is however difficult to eject gas from a heavy galaxy, hence high binding energy, by only considering this supernova feedback mechanism.

The amount of energy that can be released from a central SMBH well exceeds the binding energy of the host galaxy (Silk & Rees, 1998). This means the AGN feedback process is the possible explanation to eject enough amount of gas from a giant galaxy. AGNs are often observed as a very bright core in nearby giant galaxies at a broad range of wavelength. Although exact formation process of the AGN is yet to be observed, N-body and hydrodynamic simulations suggest an excessive gas fuelling to the supermassive black hole (SMBH) at the galaxy centre, provoked by galaxy merger (e.g., Di Matteo et al., 2005). Once the gas is transported to the galactic centre and form an accretion disc extends till tens of Schwarzschild radii around the SMBH, the gaseous disc becomes very luminous by releasing gravitational energy through friction and will be observed as a bright point source at the galaxy centre (AGN). After the luminosity becomes enhanced, its radiative pressure blows the gas out as often observed in a form of outflow. This AGN feedback process thus regulates the SMBH growth by itself, together with quenching the star formation of its entire galaxy. Di Matteo et al. (2005) shows a significant role of AGN feedback to decrease the star formation rate in their numerical simulation – a run with AGN feedback results in 10^{-2} times smaller star formation rate compared to the run without AGN feedback (see Figure 1.2). In some of the studies, ejected gas eventually falls back into the host galaxy to form stars or to again fuel the central SMBH (see, e.g., Sijacki et al., 2007; Di Matteo et al., 2008; Barai et al., 2013). Same as the supernova feedback, this mechanism can slow down the star formation and gradually quench, rather than blowing all the gas away at once.

The first two quenching processes (ram pressure stripping and supernova feedback) do not require the central SMBH to affect their host galaxies. While these processes are promising for cluster galaxies and dwarf or low-mass galaxies, these would not be enough effective for field giant galaxies. AGN feedback process is thus necessary to explain the existence of field giant ellipticals. The process can couple high enough energy to the gas , while the efficiency of the energy transportation is still uncertain. As a consequence, all of the three processes likely occur in combination to gradually slow down the star formation and to form the universe at present.

1.1.3 Formation and Evolution of Black Hole

Although we are still not able to observe the black hole itself, much indirect evidence suggests the existence of black holes, particularly SMBHs at galaxy centres. For example, AGNs are observed at any epoch from local universe to high redshift (as quasars). The very bright source is known to be very compact, and has a spectral energy distribution quite different from that of stars. AGNs are required to be very massive not to be unbound by its energy emitted by its own, that is observed as high bolometric luminosity. Typically AGN sources are required to be heavier than $10^6 M_\odot$ (see, e.g., Ferrarese & Ford, 2005), which is difficult to explain without a SMBH. Quiescent galaxies also have indications of SMBH existence. Firstly, the SMBH mass density falls from high redshift to local universe too quickly, by at least two orders of magnitudes, if we assume SMBHs only in active galaxies. The rest should reside in local quiescent galaxies, because it is quite unnatural for the SMBHs to disappear. Secondly, growing number of observations show galactic rotation curves which require a central compact massive object. The detection of Keplerian motion requires the target to be nearby, most of which are not powerful AGNs. Historical progress in SMBH indirect detection is reviewed in Kormendy & Ho (2013).

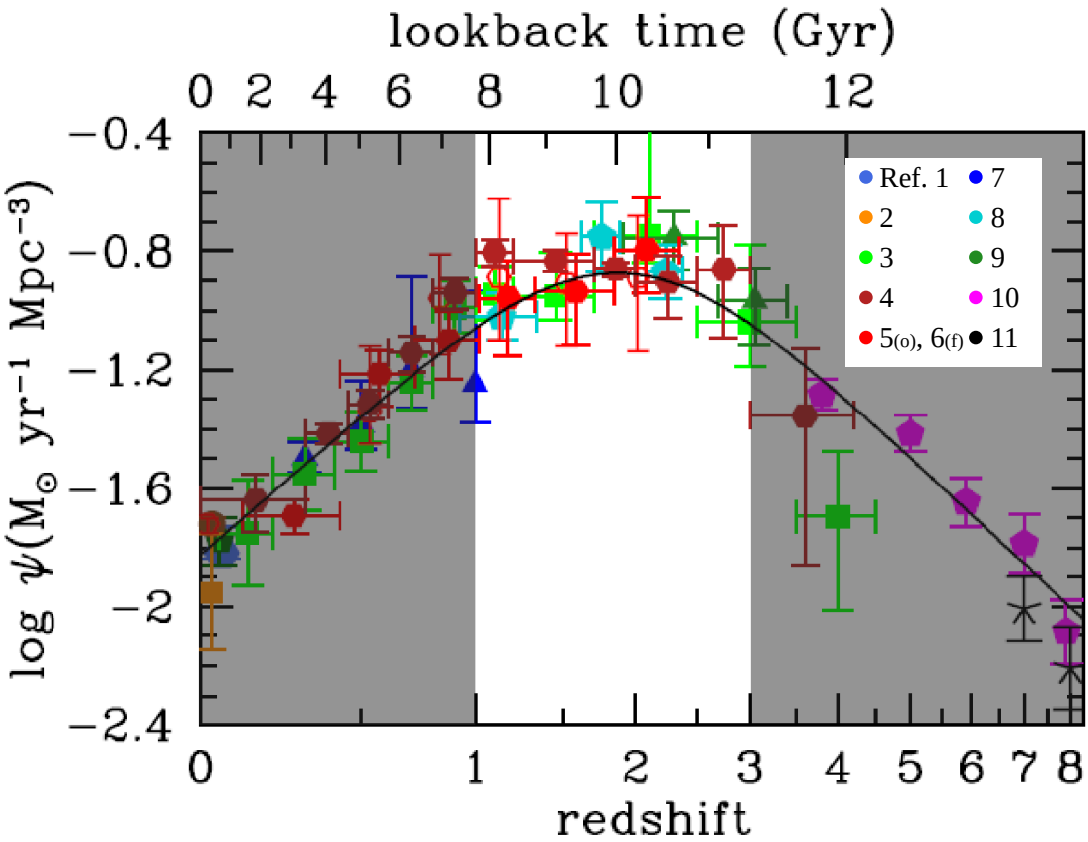

Figure 1.1: **The history of cosmic star formation rate density (SFRD):** The grey shaded areas indicate epoch of lower star formation rate, suggesting the enhancement and quenching of such activity. The original figure is from Madau & Dickinson (2014), which assembled observations at UV and IR wavelength. The plots are taken by the references as follows. *References:* (1) Wyder & GALEX Science Team (2005), (2) Takeuchi et al. (2003), (3) Cucciati et al. (2012), (4)Gruppioni et al. (2013), (5)Magnelli et al. (2011) for open symbols, (6)Magnelli et al. (2013) for filled symbols, (7)Schiminovich et al. (2005), (8)Dahlen et al. (2007), (9)Reddy & Steidel (2009), (10)Bouwens et al. (2012a,b), (11)Schenker et al. (2013)

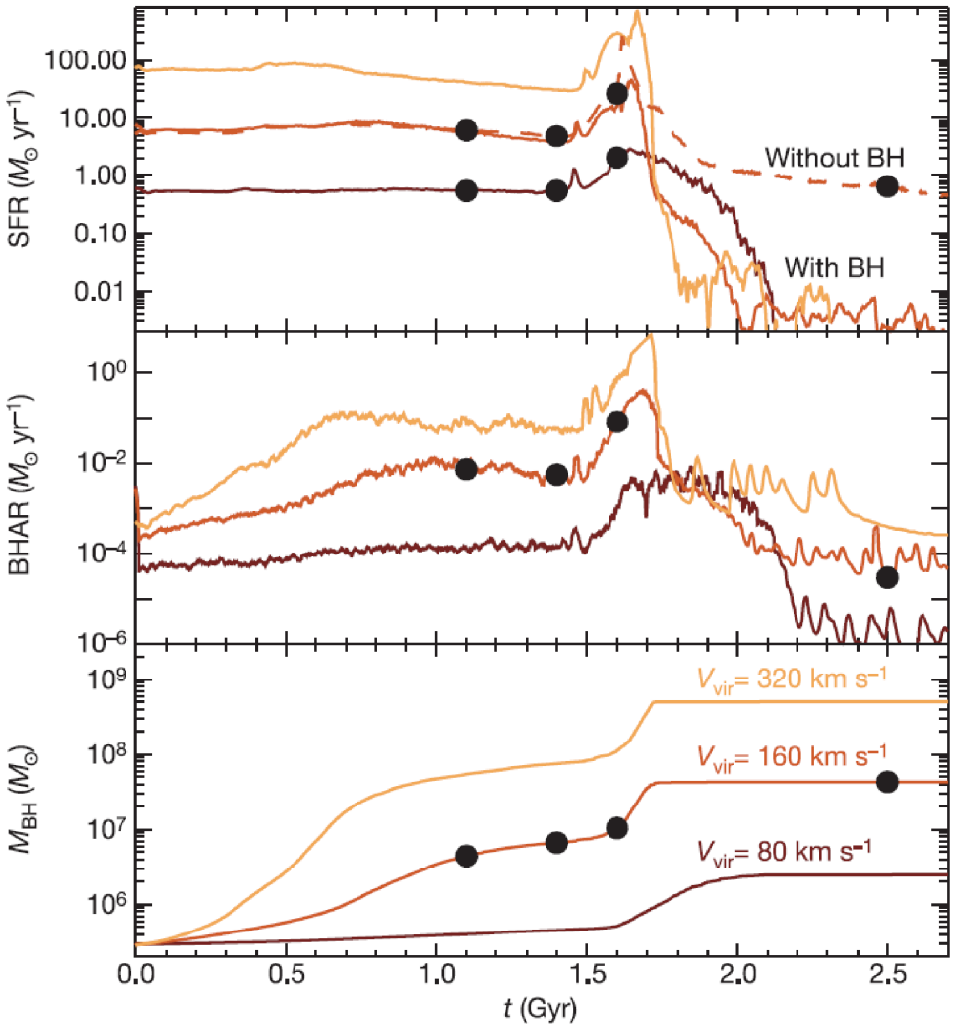

Figure 1.2: **Time evolution of star formation rate (SFR; upper panel), black hole accretion rate (BHAR; middle panel), and SMBH mass (lower panel):** These plots are calculated and presented in Di Matteo et al. (2005). The three lines correspond to models with galaxies of virial velocity $V_{\rm vir}$ =80, 160, and 320 km s^{-1}, as indicated in the lower panel. The SFR drops rapidly after the peak of BHAR when considering the SMBH (solid lines). The AGN feedback process decreases the SFR to around 100 times smaller compared to the model without SMBH (dashed line).

Formation of SMBHs is still an unresolved issue. Simulations normally assume remnants of Population Ⅲ stars or direct collapse of very low angular momentum gas to create a seed black hole. These seed black holes can grow by accreting gas with its angular momentum negligible, or by yielding gas from an accretion disc that decreases angular momentum by its viscosity and gravitational torques (see, e.g., Somerville & Davé, 2015; Hopkins & Quataert, 2010). Observations for more than two decades at the SMBH in our galaxy (see, e.g., Genzel et al., 2010, for a review) still do not detect any feeding event so far. Observations towards other nearby galaxies sometimes show complex velocity structures of gas, which can be explained with inflowing and outflowing motion along the gas disc (García-Burillo et al., 2003; Riffel et al., 2006; Diniz et al., 2015; Smajić et al., 2015). These observations help to estimate inflow rates towards central few tens of parsecs by assuming disc morphology and gas density. Although the observing facilities are substantially improved to date, transportation of gas towards the central SMBH is not observed. The growing process of black hole is thus not well understood, while there are some clear indications of a connection between SMBH growth and galaxy evolution (see Section 1.1.4 for details).

1.1.4 Correlations between SMBH Mass and Host Galaxy Properties

In the nearby universe a variety of host galaxy properties are known to be correlated with the central SMBH mass. For instance there is a tight correlation between the SMBH mass and the bulge luminosity ($M_{\rm BH} - L_{\rm bulge}$ relation, e.g., Kormendy & Richstone, 1995; McConnell & Ma, 2013; Kormendy & Ho, 2013), the galaxy total luminosity ($M_{\rm BH} - L_{\rm tot}$ relation, e.g., Läsker et al., 2014), the bulge mass ($M_{\rm BH} - M_{\rm bulge}$ relation, e.g., Magorrian et al., 1998; Marconi & Hunt, 2003; Beifiori et al., 2012; Kormendy & Ho, 2013), and the central velocity dispersion ($M_{\rm BH} - \sigma$ relation, e.g., Ferrarese & Merritt, 2000; Gültekin

et al., 2009; McConnell & Ma, 2013; Kormendy & Ho, 2013). van den Bosch (2016) shows not only SMBH, but all range of black holes from zero to 10 billion solar masses falls into a fundamental plane of black hole mass, size of the host stellar spheroid, and its luminosity. These empirical correlations do have scatter, but the implication is clear– black holes and galaxies evolve together by influencing each other (coevolution of galaxy and black hole).

Recent studies are suggesting that the correlation between the SMBH mass and bulge/host galaxy properties are more complex than originally thought. For instance McConnell & Ma (2013) showed that different coefficients for the $M_{\rm BH} - \sigma$ relation can be fit to early- and late-type galaxy samples (see Figure 1.3). Early-type $M_{\rm BH} - \sigma$ relation ($\log_{10}(M_{\rm BH}/M_{\odot}) = 8.39 + 5.20\log_{10}(\sigma/200$ km s$^{-1})$, red line in Figure 1.3) gives a SMBH mass of typically two times larger than the late-type $M_{\rm BH}-\sigma$ relation ($\log_{10}(M_{\rm BH}/M_{\odot}) = 8.07 + 5.06\log_{10}(\sigma/200$ km s$^{-1})$, blue line in Figure 1.3), at a given velocity dispersion. Kormendy & Ho (2013) in contrast claimed that no such correlations are seen for galaxies hosting psuedo-bulges. These claims are yet to be accepted nor declined, due to an insufficient amount of sample with their SMBH mass measured with small enough error.

Motivated by the unobserved coevolutionary process and its suggestive evidence from the empirical relations such as the $M_{\rm BH} - \sigma$ relation, many theoretical studies have been carried out (e.g., Silk & Rees, 1998; Di Matteo et al., 2005; Sijacki et al., 2007, etc.). Their models calculate the galaxy merger process under the assumption that seed black holes already exist in high redshift galaxies and grow self-consistently. When the black holes grow as the galaxies merge, it reaches a critical size expelling the surrounding gas by its radiation energy and quenching the growth (AGN/quasar mode feedback process). In this way the BH growth is self-regulated, gravitationally affecting the surrounding stellar spheroid. The numerical simulation of galaxy mergers by Di Matteo et al. (2005) takes

this AGN feedback process into account to successfully reproduce the $M_{\rm BH} - \sigma$ relation in the local universe. Sijacki et al. (2007) extended the quasar mode feedback process to a simple model for radio mode feedback, which assumes an AGN-driven bubble to be created when SMBH mass increases by a certain fraction $\Delta M_{\rm BH}/M_{\rm BH}$ lower than the quasar. The bubble energizes the surrounding gas thermodynamically, leading to the regulation of BH growth. In this simulation, the BH affects the surrounding gas and spheroid of stars with a smaller accretion rate than in model with only the quasar mode feedback. This simulation also reproduces the $M_{\rm BH} - \sigma$ relation in the local universe. These numerical studies suggest the observed $M_{\rm BH} - \sigma$ relation can be reproduced by a coevolutionary process that includes self-regulating mechanisms. Having said that, correlations between SMBH mass and host galaxy properties can evolve together with redshift, reflecting the evolutionary stage of galaxies at each age.

Observational studies on the redshift evolution of the correlations have not been done for the $M_{\rm BH} - \sigma$ relation, but for others such as $M_{\rm BH} - L_{\rm bulge}$ relation. Observations towards high redshift galaxies makes it difficult to determine a central velocity dispersion σ, due to their complex structure and the observational constraints. Instead of that, Peng et al. (2006a,b) explored the $M_{\rm BH} - L_{\rm bulge}$ relation for quasar host galaxies at $z \leq 2$. They showed the $M_{\rm BH} - L_{\rm bulge}$ relation does not have a redshift evolution from $z = 1$ to 2, although their galaxy samples are biased to the high mass SMBH hosts ($M_{\rm BH} > 10^8 M_\odot$) (see Figure 1.4). Numerical simulations are also used to show that the $M_{\rm BH} - \sigma$ relation evolves from $z = 1$ to 3 at the low BH mass end ($M_{\rm BH} \sim 10^6 M_\odot$), while massive BHs ($M_{\rm BH}$ larger than $10^8 M_\odot$) from $z = 1$ to 3 stay close to the local $M_{\rm BH} - \sigma$ relation (e.g., Sijacki et al., 2007, Figure 1.5).

Correlations between SMBH mass and host galaxy properties suggests a self-regulating coevolutionary mechanism of galaxy and black hole. It is, however, still unclear if these

correlations evolve along redshift, if different correlations exist for different galaxy types, or if these correlations can be applied for psudobulge hosts. These empirical correlations are discussed with 78 galaxies at this point. Increasing the number of SMBH mass measurements is thus of great importance to shed more light into this unknown coevolutionary process of galaxy and black hole.

1.2 Supermassive Black Hole Mass Estimates

After some convincing evidence for the existence of SMBHs in galaxy centres, mass estimations of SMBHs have been done in many ways (see, e.g., Kormendy & Ho, 2013, for a review). Recent significant development of observing facilities gradually allowed one to dynamically measure the SMBH mass in nearby galaxies. The number of direct measurements of SMBH mass is now growing, giving us expectations for getting to the bottom of the coevolutionary process of galaxy and black hole. Here I summarize the direct measurements and other major methods to estimate SMBH mass in various galaxies.

1.2.1 The nearest case – our galaxy

Being the closest (distance of 8.28 ± 0.33 kpc, Genzel et al., 2010), vicinity of the SMBH in our galaxy can be observed at the highest spatial resolution.

Historically the radio source Sgr A* was at first assumed to be the galactic centre, although it was uncertain (Genzel et al., 1994). Using the dynamics of neutral and ionized gas near the galactic centre, dynamical mass was already estimated to be $10^6 M_\odot$ in the 1990s by assuming the observed velocity is a circular velocity (Genzel et al., 1994; Kormendy & Richstone, 1995). Ten years later to that, it has become gradually accepted that the mass distribution at the central few parsecs can be described by a combination of a

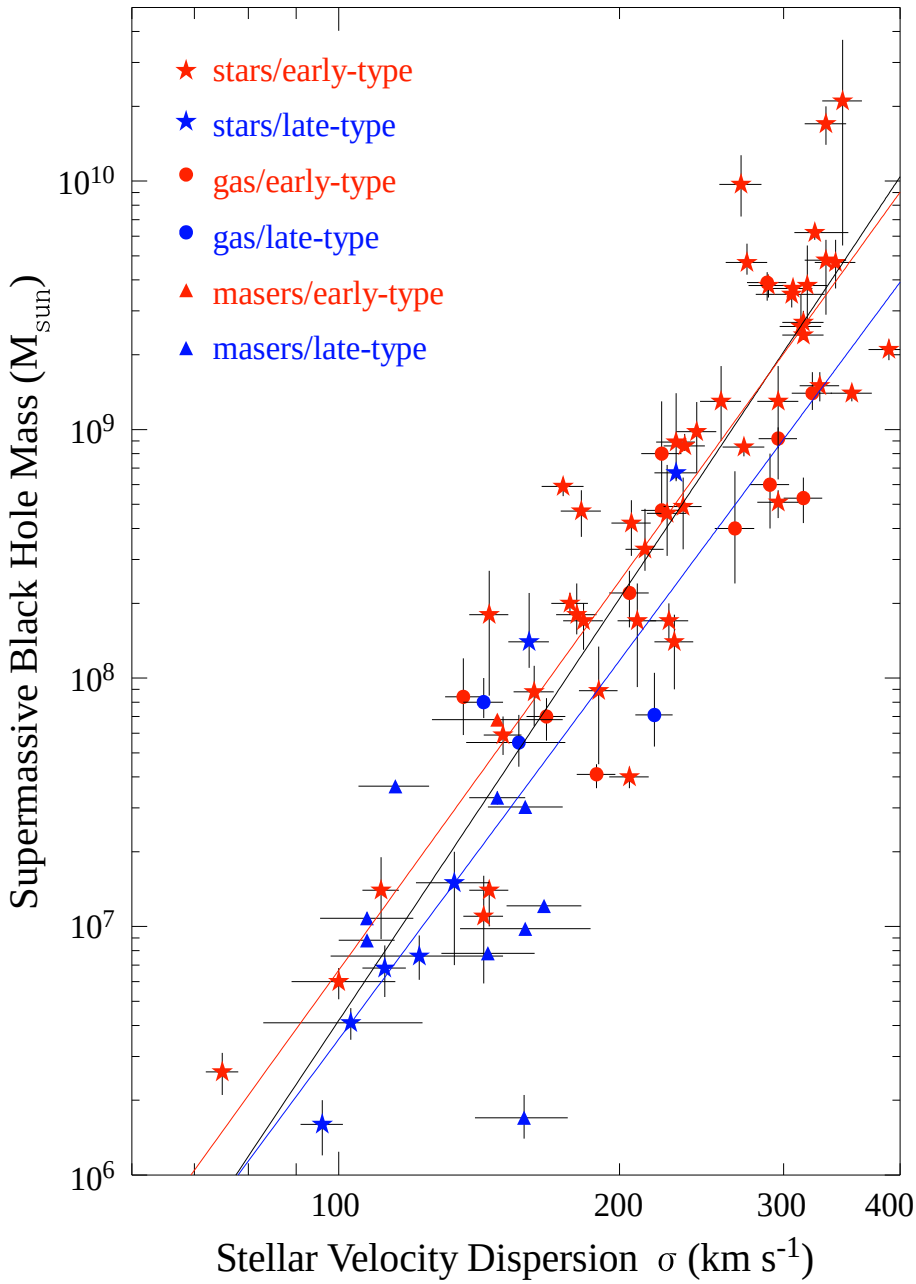

Figure 1.3: **Empirical $M_{\rm BH} - \sigma$ relation:** 78 galaxies with dynamical SMBH mass measurements, summarized by McConnell & Ma (2013). Elliptical and lenticular galaxies are plotted in red, and late-type spiral galaxies are in blue. Different symbols show different dynamical methods (see also Section 1.2) that are used to measure the SMBH masses. The black line ($\log_{10}(M_{\rm BH}/M_\odot) = 8.32 + 5.64\log_{10}(\sigma/200\ {\rm km\ s^{-1}})$) shows a fit to the entire sample. Separate fit for early-type and late-type galaxies are shown in red line ($\log_{10}(M_{\rm BH}/M_\odot) = 8.39 + 5.20\log_{10}(\sigma/200\ {\rm km\ s^{-1}})$) and blue line ($\log_{10}(M_{\rm BH}/M_\odot) = 8.07 + 5.06\log_{10}(\sigma/200\ {\rm km\ s^{-1}})$), respectively.

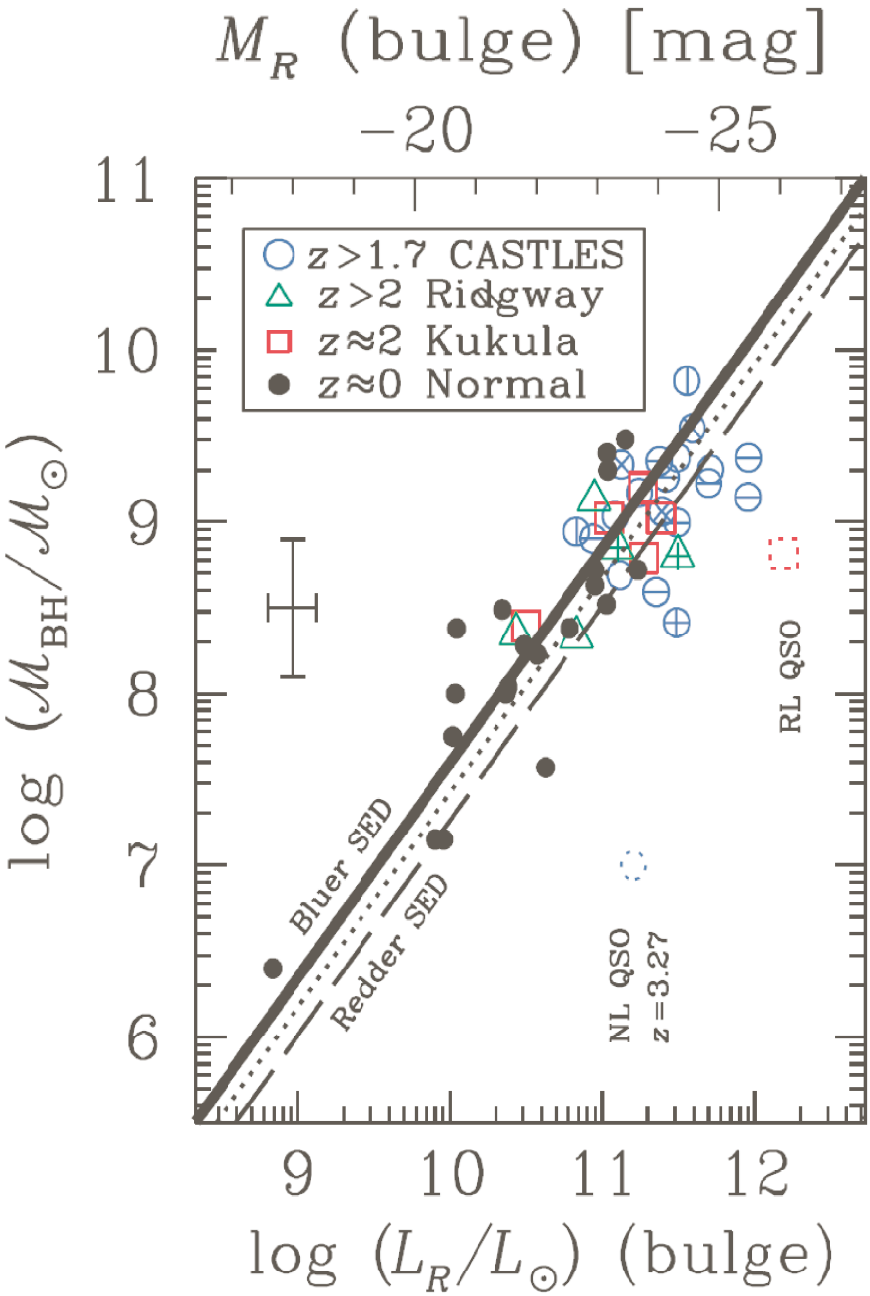

Figure 1.4: $M_{\rm BH} - L_{\rm bulge}$ **relation at high redshift:** Observational results from $z \sim$0 to $z >$2, as shown in Figure 8 of Peng et al. (2006b). The filled circles are the local comparison sample, and the solid line is the best-fit local $M_{\rm BH} - L_{\rm bulge}$ relation. The high-redshift quasar hosts are shown with open blue circles ($z >$1.7), open green triangles ($z >$2), and open red squares ($z \sim$ 2). The dotted line and the dashed line shows the best-fit relation for the high-redshift galaxies. Two lines differ with the SED template to make the $k-$ corrections (Sbc for the dotted line and E/S0 or Im for the dashed line).

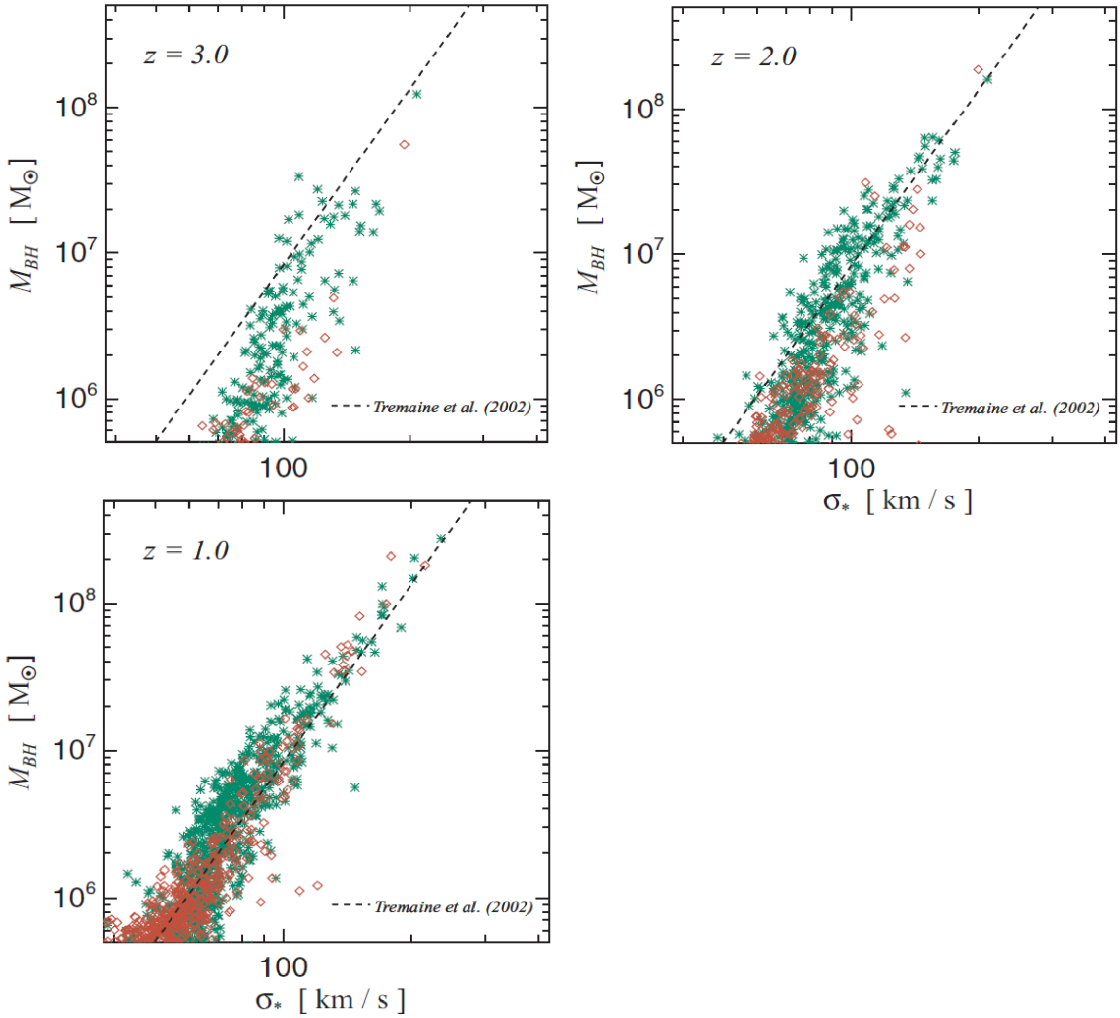

Figure 1.5: **Redshift evolution of the $M_{\rm BH} - \sigma$ relation:** $M_{\rm BH} - \sigma$ relation from z = 1 to 3 are computed and shown in Figure 15 of Sijacki et al. (2007). Green points show galaxies without galactic winds. Galaxies with galactic winds are shown in red. Local $M_{\rm BH} - \sigma$ relation is shown in black dot line (Tremaine et al., 2002). The relation evolves at low mass end ($M_{\rm BH} \sim 10^6 M_\odot$), but massive black holes ($M_{\rm BH}$ larger than $10^8 M_\odot$) do not seem to evolve from $z = 1$ to 3.

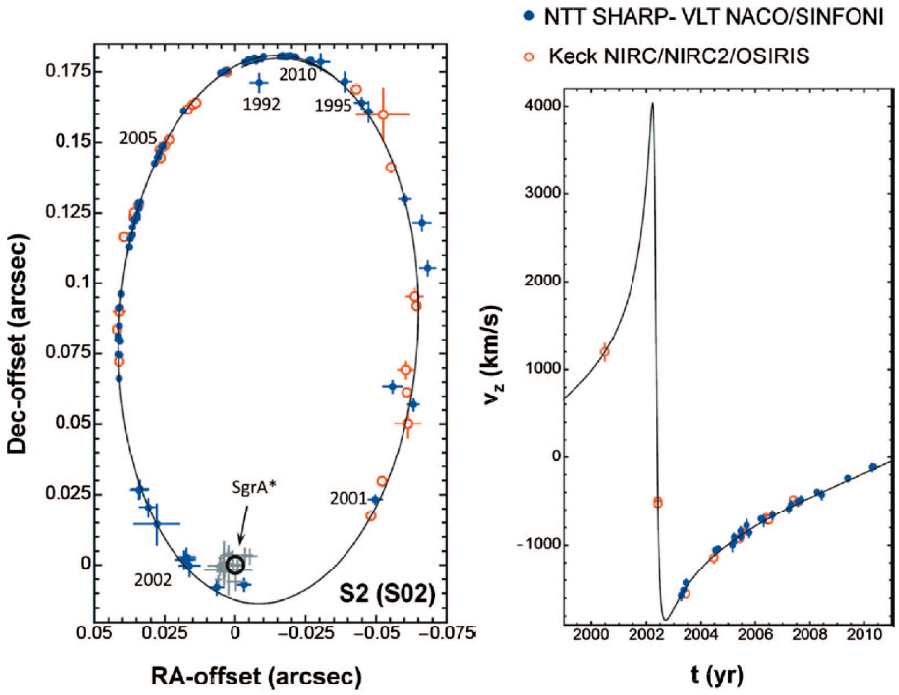

Figure 1.6: **Orbit of a star S2 around the Sgr A*:** S2 on the sky (left panel) and in radial velocity (right panel) plotted in Figure 17 of Genzel et al. (2010). Observations with ESO New Technology Telescope (NTT) and Very Large Telescope (VLT) are plotted in blue. Red circles are the data observed with Keck. The grey crosses are the positions of Sgr A* IR flares.

compact massive object at the position of Sgr A* and a dense nuclear star cluster (Genzel et al., 2010, and references therein). The central compact mass is proved by observing motions of gas (Crawford et al., 1985; Serabyn et al., 1988; Roberts et al., 1996) and stars (Rieke & Rieke, 1988; Krabbe et al., 1995; Genzel et al., 1996), and the most clearly by tracing the stellar orbits(Genzel & Eckart, 1999; Ghez et al., 2008; Gillessen et al., 2009).

The breakthrough of tracing more than one complete orbit (Figure 1.6, Genzel et al., 2010) defined the position of a compact massive object coincides with that of Sgr A* to 2 milliarcsecond. It gives the SMBH mass of $(4.30 \pm 0.30) \times 10^6 M_\odot$ (Genzel et al., 2010), the error of which is dominated by the uncertainty of its distance.

1.2.2 Dynamical modelling of nearby galaxies – megamaser systems

Unlike the case of our galaxy, extragalactic objects do not allow one to resolve individual stars around the SMBH. The Keplerian rotation of a circumnuclear gas disc, however, can be observed by using very high-angular resolution observations realized with VLBI (Very Long Baseline Interferometer). Miyoshi et al. (1995) observed water maser emission from a circumnuclear disc at the centre of NGC 4258 to establish the method of SMBH mass measurement ($M_{\rm BH} = 3.6 \times 10^7 M_\odot$, see Figure 1.7). Herrnstein et al. (2005) reported a follow-up observation for this source and fitted a warped-disc geometry to the maser positions to find that the inclination varies from 81.4 to 91 deg (see Fig 1.8). This slightly changed the measured SMBH mass to $(3.81 \pm 0.01) \times 10^7 M_\odot$. Both of these are a correct fit *assuming the model is correct*. Kormendy & Ho (2013) recalculated the error budget by considering the RMS of the mass determinations from the pure Keplerian fit, the central cluster model, thee massive disc model, and the preferred warp model. The result was reported to be $M_{\rm BH} = (3.81 \pm 0.04) \times 10^7 M_\odot$, the error budget of which is still very small.

Greene et al. (2010) and Kuo et al. (2011) expanded this method to other megamaser sources. Despite the amount of observations to search for relevant targets (see, e.g., van den Bosch et al., 2016), the number of galaxies with their SMBH mass measured from this method is only 10. Also, SMBH mass in megamaser systems are biased to low mass (less than $10^8 M_\odot$) for unknown reason. Megamaser systems are quite rare, making this method not very helpful to increase the number of galaxies in the empirical $M_{\rm BH} - \sigma$ relation (see Section 1.1.4).

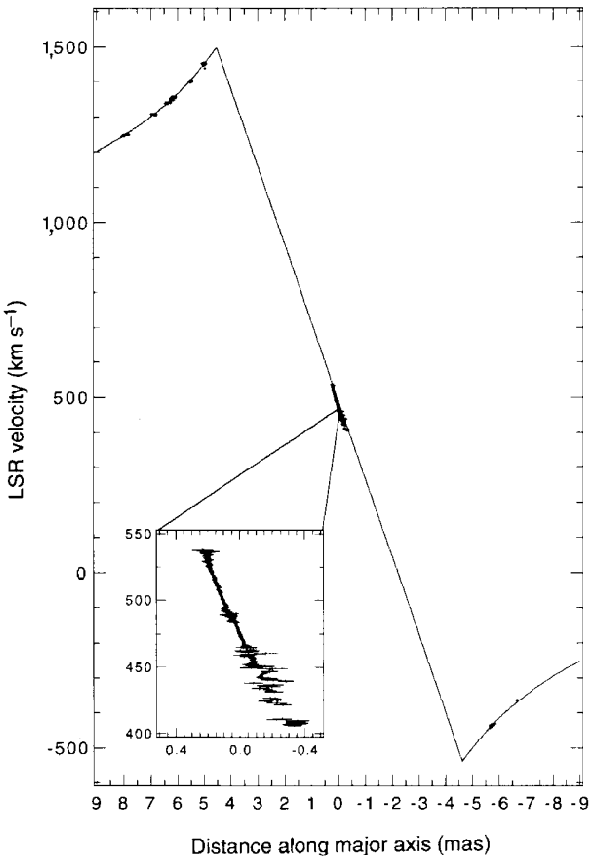

Figure 1.7: **A radial velocity profile of the water masers:** The Keplerian motion of water masers, as shown in Figure 3 of Miyoshi et al. (1995). The black line shows the model and the black dots are the observation.

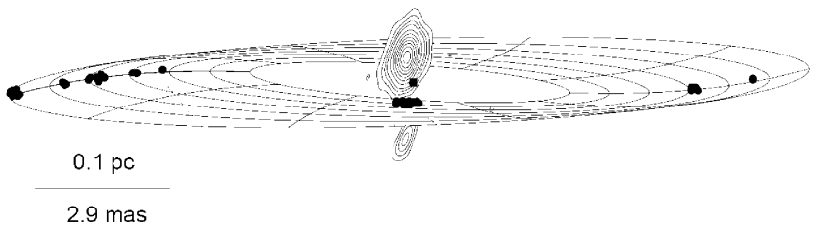

Figure 1.8: **A warped disc model for NGC 4258:** Masers (black dots) and continuum (contours), as shown in Figure 1 of Herrnstein et al. (2005).

1.2.3 Dynamical modelling of nearby galaxies – stellar dynamcis

The most powerful method at this point, in terms of increasing the number of direct SMBH mass measurements, is the stellar dynamical method. Over 65% of the whole sample in Figure 1.3 is measured by using this method. The sample ranges from relatively low-mass SMBH to the heaviest SMBH (ten-billion solar mass) discovered at present.

Details of this method is summarized in Kormendy & Ho (2013) and very well described in many of the works (see, e.g., Dressler & Richstone, 1988; van der Marel & van den Bosch, 1998; Cappellari et al., 2002; Gebhardt et al., 2003; Valluri et al., 2005; McConnell et al., 2011; van den Bosch et al., 2012; Rusli et al., 2013). The brief summary is given below. In the method, line-of-sight velocity distributions (LOSVD) of stars are observed with ground-based two-dimensional spectroscopes. The orbit superposition model (Schwarzschild, 1979) is applied to model the galaxy. A gravitational potential is defined as a sum of central point mass and a stellar mass distribution, often modelled by a stellar luminosity distribution multiplied by stellar mass-to-light ratio (M/L). All possible orbits are then calculated within the potential, to give three-dimensional distribution of densities, velocities, and velocity dispersions, all averaged over time. Comparing the result with the observed LOSVD, the best-fit potential field will be chosen, thereby determining the mass profile including the SMBH mass. Details of the method varies among studies. For example Gebhardt & Thomas (2009) considered a dark matter mass profile in addition to SMBH and stars, while McConnell et al. (2013) considered a spatial distribution for the stellar M/L by using observations at different band.

Although careful treatments for the accuracy is given for this established method, it does not help to complete the sample of the $M_{\rm BH} - \sigma$ relation. The dynamical modelling tools are relatively complex and the model is often restricted to be axisymmetric. The sample for this method is heavily biased to early-type galaxies, due to this modelling

tools. Triaxial modelling is becoming popular after the development by van den Bosch et al. (2008) and known to be needed especially for core elliptical galaxies with near-face-on inclination (see, e.g., van den Bosch & de Zeeuw, 2010, for details). Triaxial models are however not often used due to its expensiveness.

1.2.4 Dynamical modelling of nearby galaxies – ionized gas dynamics

This method using dynamics of ionized gas has a larger number of potential targets compared to other methods. Other than its broad range of targets, this method has advantages on both observation and modelling. Ionized gas kinematics is relatively easy to trace, compared to observations of stellar absorption lines. Radial velocity distribution of the ionized gas ([N II] line, for example, in de Francesco et al. 2008) can be observed by taking spectra from multiple slits (de Francesco et al., 2008) or recently by using integral field units (IFUs; e.g., Neumayer et al., 2007). In nearby galaxies, an angular resolution required for this method is feasible with both ground-based facilities (e.g., Cappellari et al., 2002; Shields et al., 2007) and *HST* (e.g., Ferrarese et al., 1996; Barth et al., 2001; Dalla Bontà et al., 2009; Walsh et al., 2010). Dynamics of ionized gas is relatively easy to model, compared to the expensive modelling used in stellar dynamics method (Section 1.2.3). If the gas is in a dynamically cold disc, as normally assumed, the circular motion can be simply calculated in an axisymmetric gravitational potential (see, e.g., Cappellari et al., 2002). The mass distribution is modelled to be a summation of SMBH (point mass) and surrounding stars, described by a luminosity distribution multiplied by a stellar M/L. Dark matter halos are normally neglected in the model. The best-fit is picked to match the observed velocity field and surface brightness distribution.

Despite the above advantages, the number of measured SMBH mass from this method is only 13 objects over 72 in Figure 1.3. The difficulty to measure SMBH mass by using

this method comes from a couple of requirements that are not practical for gas. First, gas must be distributed within the radius of the SMBH sphere of influence (SOI) and properly sampled. Further, the velocity distribution has to trace circular motion. Ionized gas in reality, is not dynamically settled to the rotating motion, but sensitively corresponds to the non-gravitational perturbations such as turbulence, shocks, radiation pressure, pressure gradient, and magnetic field, to show non-circular motions (see, e.g., Shapiro et al., 2006). The turbulence of gas made it quite difficult to correctly model the velocity structure from slit observations. Recent development of IFUs are solving this problem in some cases, although the observations still cannot avoid the uncertainty from dust extinction effect.

1.2.5 Dynamical modelling of nearby galaxies – molecular gas dynamics

Kinematics of molecular gas can be observed at millimeter/sub-millimeter wavelengths, which enables to avoid the dust extinction effect. SMBH mass measurement using its dynamics can be simply done by assuming a thin molecular gas disc at the galaxy centre, as observed in many nearby galaxies (Young et al., 2011). The method has its potential target across the Hubble sequence, and is straightforward. Molecular gas discs are known to be dynamically cold in most galaxies (see, e.g., Young et al., 2011; Alatalo et al., 2013), and this decreases the assumption of the dynamical modelling.

Nevertheless, this method was never possible before Davis et al. (2013). Recent improvements of mm-wavelength interferometers reached an angular resolution and sensitivity high enough to trace the precise kinematics of molecular gas, allowing one to measure SMBH mass. After the first report, the dynamics of molecular gas probed at mm/sub-mm wavelengths has emerged as a very promising method (see, e.g., Davis et al., 2013; Onishi et al., 2015; Barth et al., 2016a,b; Onishi et al., 2016), particularly be-

cause of the exquisite angular resolution and sensitivity afforded by the Atamaca Large Millimeter/sub-millimeter Array (ALMA).

The major advantage of this method is the enormous potential for increasing the number of sample in the $M_{\rm BH} - \sigma$ relation. For instance, Davis (2014) showed ALMA with its full capability can measure SMBH masses in $\approx 35,000$ local galaxies. The sphere of influence (SOI; $R_{\rm SOI} \equiv GM_{\rm BH}/\sigma^2$, where G is the gravitational constant) of the largest SMBHs ($M_{\rm BH} \geq 10^{8.5}\ M_\odot$) is spatially resolvable across the whole of cosmic time. Needless to say, the molecular gas method also has a potential to redress the current bias against late-type galaxies in $M_{\rm BH} - \sigma$ studies (now only $\approx 30\%$ of the sample).

Given the potential and its advantages for this method, it is of great importance to first prove the method is valid in both early- and late-type galaxies, and to establish the method by well addressing its possible error sources.

1.2.6 SMBH Mass Estimates at High Redshift

SMBH mass measurements of nearby galaxies can be done in several dynamical methods as described above, while it is crucial to know SMBH mass at high redshift in order to discuss on SMBH growth as a part of the coevolutionary process of galaxy and black hole.

SMBH mass estimates for AGN hosts utilize a method called reverberation mapping. The method has been developed and originally used (see, e.g., Blandford & McKee, 1982; Netzer & Peterson, 1997) to measure the size of the broad-line region (BLR, see Figure 1.9 for a schematic view) around the central SMBH, for objects at $z \leq 0.5$. The light-travel time delay is measured by taking light curves of continuum emission and broad emission line. By assuming the BLR geometry to be as sketched in Figure 1.9, the distance between the ionizing continuum source and the ionized gas, thus the characteristic size of the BLR can be calculated.

It is difficult to observe the light curve of sources at higher-redshift ($z \geq 2$). Instead of that, the empirical correlation between the BLR radius and optical continuum luminosity ($R_{\rm BLR} \propto L_{5100\mathring{\rm A}}^{0.65-0.7}$, Kaspi et al., 2005) is used to estimate the BLR size. With an assumption that the broad emission line width is showing the virial motion by the gravitational potential of a central massive object, the BLR size and the observed line width together gives an estimate of the SMBH mass (see, e.g., Peterson & Wandel, 1999; Vestergaard, 2002; Kaspi et al., 2005; Netzer et al., 2007).

The method is straightforward and allows to estimate a large number of SMBH masses for objects with unresolvable SMBH SOI. The estimated SMBH masses, however, require careful treatment. Lower-redshift sources ($z \leq 0.3$), such as in Kaspi et al. (2005), are measured their gas velocity by using Hβ line width. Considering uncertainties on BLR size, variable source luminosity, BLR geometry and error of the line width, the derived SMBH masses have factor of ~ 2 uncertainty (Netzer et al., 2007). In case of higher redshift sources ($1 \leq z \leq 6$), the gas velocity is measured from a line width of $C_{\rm IV}$ λ1549 (e.g., Vestergaard, 2002; Park et al., 2013), $Mg_{\rm II}$ λ2798, (e.g., McLure & Jarvis, 2002; Shen et al., 2008; Trakhtenbrot & Netzer, 2012) and Hα (e.g., Greene & Ho, 2005; Shen & Liu, 2012). A large uncertainty on the derived SMBH mass is pointed out when using $C_{\rm IV}$ line in combination with a continuum emission at ~ 1400Å(see, e.g., Baskin & Laor, 2005; Sulentic et al., 2007). Precision of the results from these emission lines are still under discussion (e.g., Mejía-Restrepo et al., 2016).

Another way to estimate the SMBH mass in high redshift galaxies is to use a gravitational lens effect. Tamura et al. (2015) and Wong et al. (2015) used high-resolution ALMA observations and archival *HST* imaging to model a gravitational lens H-ATLAS J090311.6+003906 and independently derived the innermost mass distribution of the foreground lensing galaxy. Tamura et al. (2015) constrained the lower limit of the SMBH

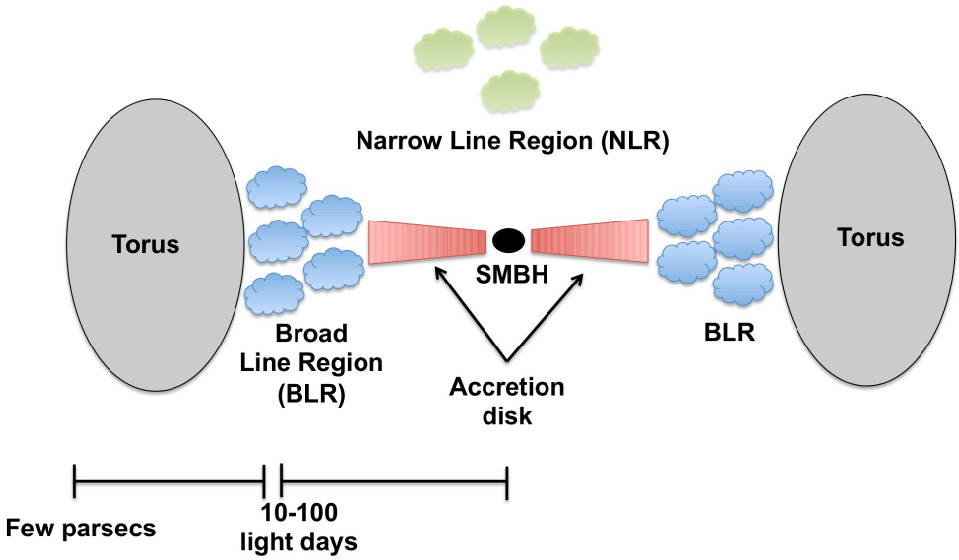

Figure 1.9: **A schematic view of an AGN:** A typical structure of AGN, provided by a website of Dr. C. Ricci [1]. The BLR emits the broad optical/UV lines. The accretion disc is considered as the continuum emission source. The reverberation mapping technique measures the inner radius of the BLR to be typically 10-100 light days.

mass to be $3.0 \times 10^8 M_\odot$, and Wong et al. (2015) ruled out the SMBH mass of less than $3.16 \times 10^8 M_\odot$. An estimate of the SMBH mass by using the $M_{\rm BH} - \sigma$ relation (Kormendy & Ho, 2013) and $\sigma \sim 265$ km s^{-1} is given in Tamura et al. (2015) to be $M_{\rm BH} \sim 1.0 \times 10^9 M_\odot$, and both of the results are consistent with this estimate. Upper limit of the SMBH mass can be given with deeper ALMA observations to detect the CO emission from the foreground galaxy.

1.2.7 Cross Checks Between SMBH Mass Measuring Methods

A couple of SMBH mass measuring methods are now being developed and used. The results needs to be verified by independent methods. The cross check has been done so far for 12 objects by using multiple SMBH mass measuring methods. The results can be

[1] http://www.isdc.unige.ch/ricci/Website/Active_Galactic_Nuclei.html

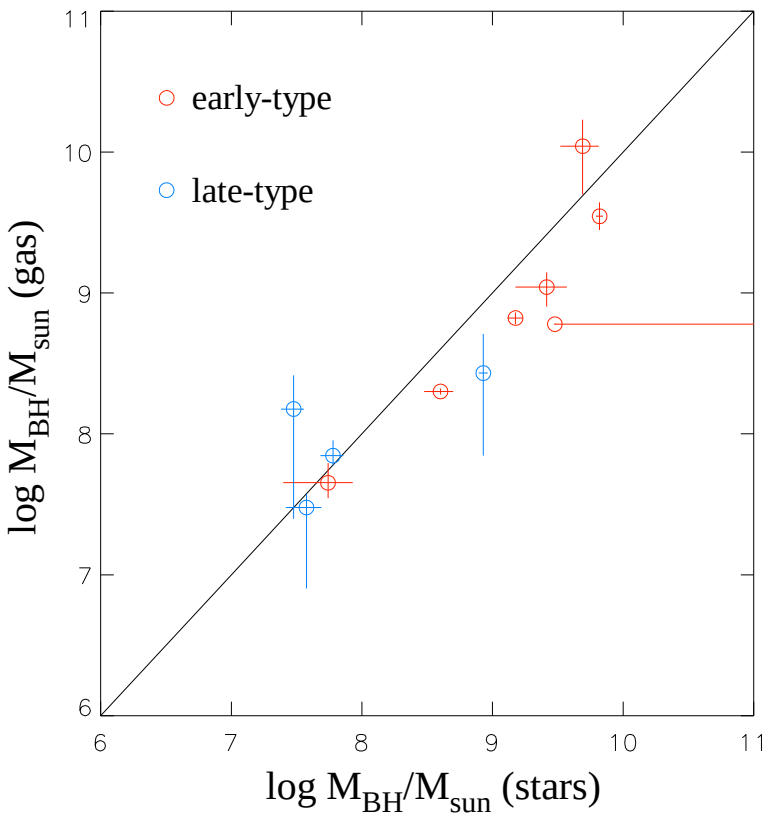

Figure 1.10: **Cross checks between SMBH mass measuring methods:** 11 Examples of cross checks done so far between ionized gas dynamics method and stellar dynamics method. Red points represent early-type galaxies and late-types are in blue. The plots are also summarized in Table 1.1. Despite the scatter, most of the data are clearly below the line of $x = y$, thus suggesting that ionized gas method derives systematically lower SMBH masses compared to stellar dynamics method.

compared in Table 1.1 and Figure 1.10. As discussed and summarized in Kormendy & Ho (2013) with less plots, gas dynamical measurement seem to underestimate the SMBH mass, although the small sample prevents us from giving a statistically good enough conclusion. The molecular gas method will not only increase the sample, but enables to give a cross check for all other methods. This supports the importance of developing the method, which will be described in Chapter 2 (see also Onishi et al., 2015), Chapter 3 (see also Onishi et al., 2016) and in Chapter 4 (Onishi et al. 2017 in prep.).

Table 1.1: SMBH mass measurements with multiple methods

Galaxy	Type	SMBH mass ($M_\odot$)	Method	Reference
IC 1459	E3	$(2.6 \pm 1.1) \times 10^9$	stars	Cappellari et al. (2002)
		$(1.1 \pm 0.3) \times 10^9$	gas(i)	Cappellari et al. (2002)
M 81	SA	$(6.0 \pm 1.2) \times 10^7$	stars	Bower et al. (2000)
		$(7^{+2}_{-1}) \times 10^7$	gas(i)	Devereux et al. (2003)
M 87	E	$(6.6 \pm 0.4) \times 10^9$	stars	Gebhardt et al. (2011)
		$(3.5^{+0.9}_{-0.7}) \times 10^9$	gas(i)	Walsh et al. (2013)
NGC 1277	S0	$(4.9 \pm 1.6) \times 10^9$	stars	Walsh et al. (2015)
		$(5 - 17) \times 10^9$	gas(m)	Scharwächter et al. (2016)
NGC 1332	S0	$(1.5 \pm 0.2) \times 10^9$	stars	Rusli et al. (2011)
		$(6.64^{+0.65}_{-0.63}) \times 10^8$	gas(m)	Barth et al. (2016b)
NGC 3227	SAB	$(0.7 - 2.0) \times 10^7$	stars	Davies et al. (2006)
		$(7.63^{+1.62}_{-1.72}) \times 10^6$	reverb	Denney et al. (2010)
NGC 3379	E1	$(4 \pm 1) \times 10^8$	stars	van den Bosch & de Zeeuw (2010)
		$(2.0 \pm 0.1) \times 10^8$	gas(i)	Shapiro et al. (2006)
NGC 3998	SA0	$(8.5 \pm 0.7) \times 10^8$	stars	Walsh et al. (2012)
		$(2.7^{+2.4}_{-2.0}) \times 10^8$	gas(i)	de Francesco et al. (2006)
NGC 4151	SAB	$(3.76 \pm 1.15) \times 10^7$	stars	Onken et al. (2014)
		$(3.00^{+0.75}_{-2.20}) \times 10^7$	gas(i)	Hicks & Malkan (2008)
		$(3.57^{+0.45}_{-0.37}) \times 10^7$	reverb	Onken et al. (2014)
NGC 4258	SAB	$(2.4 - 3.6) \times 10^7$	stars	Siopis et al. (2009)
		$(2.5 - 26) \times 10^7$	gas(i)	Pastorini et al. (2007)
		$(3.9 \pm 0.1) \times 10^7$	masers	Herrnstein et al. (2005)
NGC 4335	E	$\geq 3 \times 10^9$	stars	Verdoes Kleijn et al. (2002)
		$\sim 6 \times 10^8$	gas(i)	Verdoes Kleijn et al. (2002)
NGC 5128	S0	$(5.5 \pm 3.0) \times 10^7$	stars	Cappellari et al. (2009)
(Cen A)		$(4.5^{+1.7}_{-1.0}) \times 10^7$	gas(i)	Neumayer et al. (2007)

Column 1 is the object name; Column 2 is the Hubble type; Column 3 is the SMBH mass measured with method shown in Column 4; Column 4 shows the method. gas(i) stands for ionized gas, and gas(m) means molecular gas. Column 5 is the reference for SMBH mass measurements.

1.3 Road Map

I have described so far the importance of the SMBH mass measurement to unveil the coevolutoinary process of galaxy and black hole. Dynamical measurements of SMBH masses have been done for ~ 80 galaxies by using a handful of methods. Providing a broad range of target galaxy types and SMBH masses, the molecular gas method will help dramatically increasing the sample for the $M_{\rm BH} - \sigma$ relation, and will thus be a powerful tool to help understanding the key question in contemporary astrophysics.

This work focuses on the method development to measure the SMBH mass in various nearby galaxies observed with radio interferometers. The first SMBH mass measurement from ALMA observation (Onishi et al., 2015) is described in Chapter 2. By utilizing a more sophisticated fitting procedure, another SMBH mass measurement by Onishi et al. (2016) is described in Chapter 3. Observing with higher angular resolution, we repeat the method at a different galaxy to measure the SMBH mass and included a velocity dispersion distribution in our model (Chapter 4, Onishi et al. 2017 in prep.).

As a general discussion, the $M_{\rm BH} - \sigma$ relation is renewed and explored in Chapter 5. Possible discussions on the connection between the coevolutionary process of galaxy and black hole, and the relation itself is described in the section. I finally conclude our work in Chapter 6.

Chapter 2

A Development of SMBH Mass Measuring Method

2.1 Abstract of the Chapter

Citing from our work (Onishi et al., 2015), I here present a measurement of the mass of the supermassive black hole (SMBH) in the nearby type-1 Seyfert galaxy NGC 1097 using Atacamma Large Millimeter/Submillimeter Array (ALMA) observations of dense gas kinematics. Dense molecular gas dynamics are traced with $\mathrm{HCN}(J = 1 - 0)$ and $\mathrm{HCO^+}(J = 1 - 0)$ emission lines. Assuming a host galaxy inclination of $46°$, we derive a SMBH mass, $M_{\mathrm{BH}} = 1.40^{+0.27}_{-0.32} \times 10^8 M_\odot$, and an I-band mass to light ratio to be $5.14^{+0.03}_{-0.04}$, using $\mathrm{HCN}(J = 1 - 0)$. The estimated parameters are consistent between the two emission lines. The measured SMBH mass is in good agreement with the SMBH mass and bulge velocity dispersion relationship.

This work established the SMBH mass measuring method using molecular gas dynamics, and the result demonstrated ALMA's potential for deriving accurate SMBH masses, especially for nearby late-type galaxies. Larger samples and accurate SMBH masses will

further elucidate the relationship between the black hole (BH) and host galaxy properties and will constrain the coevolutionary growth of galaxies and BHs.

2.2 Introduction

As discussed in Chapter 1, dynamical measurements of SMBH mass are done by observing the kinematics of masers (see Section 1.2.2), stars (see Section 1.2.3), or ionized gas (see Section 1.2.4). Recent development of observing facilities, especially of millimeter/submillimeter interferometers have enabled to resolve the gravitational sphere of influence of a SMBH in nearby galaxies. This led to the first SMBH mass measurement using kinematics of CO gas in a nearby S0 galaxy NGC 4526, presented in Davis et al. (2013).

This new method is expected to give a broad range of sample, in terms of galaxy type, and to increase the number of sample. We therefore use the method initially employed by Davis et al. (2013) and extend it to measure the SMBH mass in a barred spiral galaxy. Also, aiming to confirm the method, we use two different molecular gas species, $\mathrm{HCN}(J = 1 - 0)$ and $\mathrm{HCO^+}(J = 1 - 0)$, to trace the gas kinematics and measure the SMBH mass from each. Our target here is a nearby barred spiral galaxy NGC 1097, observed with ALMA (Project code = 2011.0.00108.S; PI = K. Kohno).

The observations and data reduction are described in Section 2.3. The SMBH mass measurement method is explained in Section 2.4. Section 2.5 contains discussions about the effect of dust extinction on the derived SMBH mass (Section 2.5.1), how the inclination angle of NGC 1097 affects the result (Section 2.5.2), the dependence of SMBH mass on the molecular gas species used to trace the dynamics (Section 2.5.3). The conclusions are summarized in Section 2.6.

2.2.1 The Target – NGC 1097

NGC 1097 is a nearby Type-1 Seyfert galaxy at a distance of 14.5 Mpc (Tully, 1988) ($\sim$ 70 pc arcsecond^{-1}). The position of the nucleus is determined by the peak position of the 6 cm continuum emission (Hummel et al., 1987): $RA(\mathrm{J2000.0}) = 02^{\mathrm{h}}46^{\mathrm{m}}18^{\mathrm{s}}.96$, $DEC(\mathrm{J2000.0}) = -30°16'28''.9$. The peak position of the 860 μm continuum emission coincides with the 6 cm peak (Izumi et al., 2013). Properties of NGC 1097 are summarized in Table 2.1.

The SMBH mass in NGC 1097 is estimated to be $(1.2 \pm 0.2) \times 10^8 M_\odot$ by Lewis & Eracleous (2006) using the empirical $M_{\mathrm{BH}} - \sigma$ relation from Tremaine et al. (2002) with an observed $\sigma = 196 \pm 5$ km s^{-1}. The uncertainty in this estimate is large, depending on the assumed $M_{\mathrm{BH}} - \sigma$ relation. The latest $M_{\mathrm{BH}} - \sigma$ relation [$\log_{10}(M_{\mathrm{BH}}/M_\odot) = 8.32 + 5.64 \log_{10}(\sigma/200$ km s^{-1}), McConnell & Ma (2013)] would yield SMBH mass of $(1.9 \pm 0.3) \times 10^8 M_\odot$. Note that this relation is a fit to both late-type and early-type galaxies. When selecting only the late-type galaxies, the $M_{\mathrm{BH}} - \sigma$ relation becomes $\log_{10}(M_{\mathrm{BH}}/M_\odot) = 8.07 + 5.06 \log_{10}(\sigma/200$ km s^{-1}) (McConnell & Ma, 2013) and the estimated SMBH mass becomes $(1.1 \pm 0.3) \times 10^8 M_\odot$.

The enclosed mass in 40 pc radius has been studied by (Izumi et al., 2013) to be $2.8 \times 10^8 M_\odot$, using the dynamics from $\mathrm{HCN}(J = 4-3)$ emission line. In contrast, Fathi et al. (2013) report a dynamical mass in 40 pc radius as $8.0 \times 10^6 M_\odot$ from the same data of Izumi et al. (2013). The difference occurs because Fathi et al. (2013) assume a thin disc and extracts the non-circular motions of the gas while Izumi et al. (2013) assume a simple Keplerian rotation. Note but the dynamical mass of Izumi et al. (2013) includes all the mass within that radius, not showing the intrinsic SMBH mass. A more detailed study of NGC 1097 is thus necessary to precisely measure the SMBH mass.

Table 2.1: Properties of NGC 1097

Parameter	Value	Reference
Morphology	SB(s)b	de Vaucouleurs et al. (1991)
Nuclear activity	Type 1 Seyfert	Storchi-Bergmann et al. (1993)
Position of nucleus		Hummel et al. (1987)
R. A.(J2000.0)	$02^{\mathrm{h}}46^{\mathrm{m}}18^{\mathrm{s}}.96$	
DEC.(J2000.0)	$-30^{\circ}16'28''.9$	
Systemic velocity (km s^{-1})	1253[1]	Onishi et al. (2015)
Position angle (°)	130	Onishi et al. (2015)
Inclination angle (°)	46±5	Ondrechen et al. (1989)
Distance (Mpc)	14.5	Tully (1988)
Linear scale (pc $arcsec^{-1}$)	70	Tully (1988)
I-band luminosity (mag)	8.09	Springob et al. (2007)

[1] Systemic velocity here is a heliocentric velocity determined with molecular lines. Koribalski et al. (2004) shows the heliocentric velocity to be 1271 km s^{-1} determined with HIPASS observation.

2.3 Observation

NGC 1097 was observed with the band 3 receiver on ALMA using the two sideband dual-polarization setup as a cycle 0 observation (Project code = 2011.0.0108.S; PI = K. Kohno). The observations were conducted on 2012 Jul 29 and 2012 Oct 19 with an hour angle from -4 to 2 and a total on-source time of 105.24 minutes. The antennas were in the Cycle 0 extended configuration (400m baselines) which resulted in a synthesized beam of $1''.60 \times 2''.20$ at a position angle $-81.2°$ ($\sim$ 112 pc $\times$ 154 pc). The receivers were tuned to cover the frequency range from 87.275 GHz to 100.917 GHz with two spectral windows each in the upper sideband (USB) and the lower sideband (LSB). Each spectral window had a bandwidth of 1.875 GHz with 3840 channels. The channel separation was 0.488 MHz. Observational parameters are summarized in Table 2.2. The field of view (full width half maximum of the primary beam) at these frequencies was $69''$. The data were reduced and imaged using CASA (Common Astronomy Software Applications) 4.0 with a robustness parameter of 0.5. We binned the data by 2 channels to improve the signal to noise ratio and our final resolution is 0.976 MHz or ~ 3 km s^{-1}. Molecular gas emission is detected over 560 km s^{-1} ($\mathrm{HCN}(J = 1 - 0)$ emission is seen from 88.1524-88.3467 GHz and $\mathrm{HCO^+}(J = 1 - 0)$ from 88.7139-88.9082 GHz). The integrated intensity moment zero and intensity weighted velocity maps were made using Karma (Gooch, 1996). These are shown in Figure 2.1. The noise in the integrated intensity maps is 22 (mJy beam^{-1} km s^{-1}) in the $\mathrm{HCN}(J = 1 - 0)$ and 26 (mJy beam^{-1} km s^{-1}) in the $\mathrm{HCO^+}(J = 1 - 0)$ maps respectively. The peak flux is detected at 52σ in the $\mathrm{HCN}(J = 1 - 0)$ map and at 29σ in the $\mathrm{HCO^+}(J = 1 - 0)$ map respectively. The data clearly show the rotation dominated kinematics of the molecular gas around the SMBH.

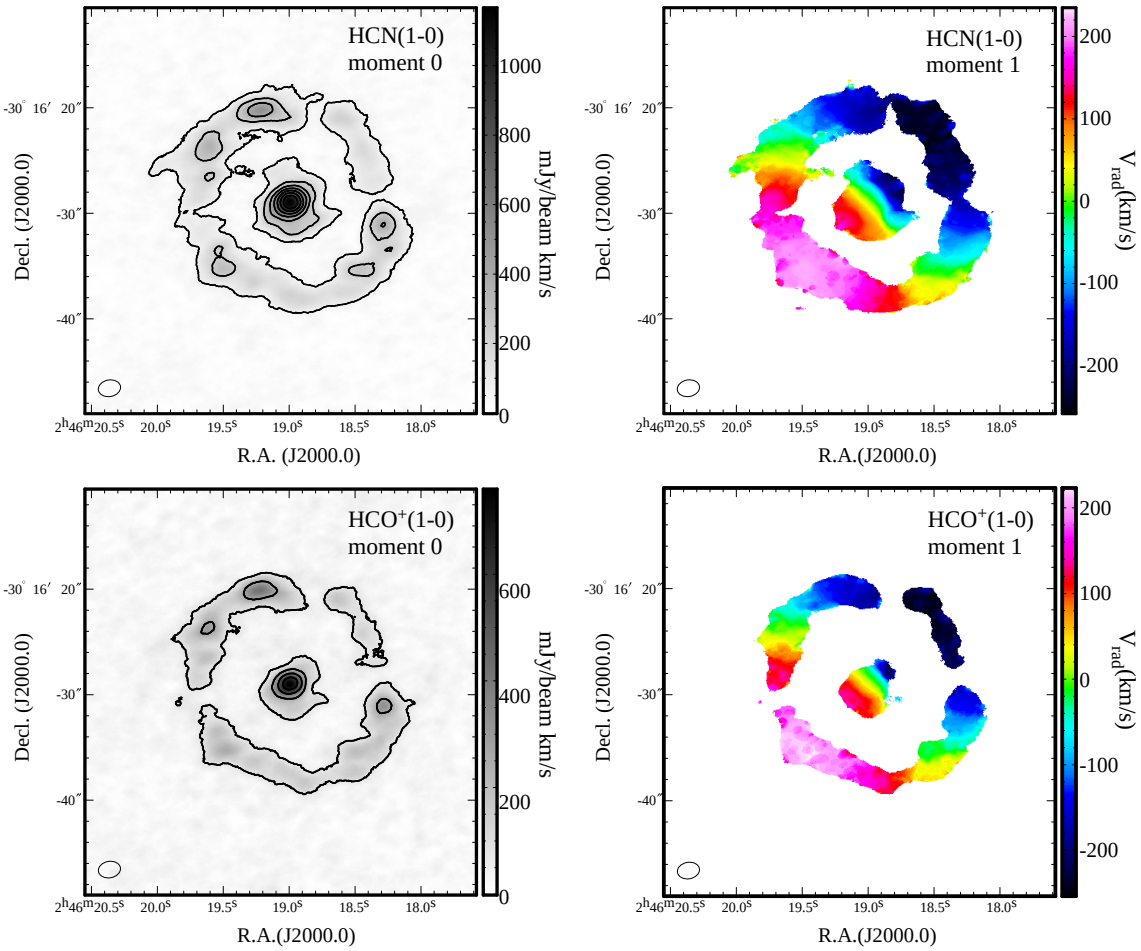

Figure 2.1: **NGC 1097 Moment 0 and 1 Maps of** $\mathrm{HCN}(J = 1-0)$ **and** $\mathrm{HCO^+}(J = 1-0)$**:** *(Left side)* Integrated intensity map (moment 0) for $\mathrm{HCN}(J = 1-0)$ (upper panel, integrated for 88.1524-88.3467 GHz) and $\mathrm{HCO^+}(J = 1-0)$ (lower panel, 88.7139-88.9082 GHz). The rms noise level (1σ) in each integrated intensity map was 22 (mJy beam^{-1} km s^{-1}) in $\mathrm{HCN}(J = 1-0)$, and 26 (mJy beam^{-1} km s^{-1}) in $\mathrm{HCO^+}(J = 1-0)$. The map is shown in grey scale with contour levels 3σ to 45σ in steps of 7σ for $\mathrm{HCN}(J = 1-0)$ (upper panel), and 3σ to 24σ in steps of 7σ for $\mathrm{HCO^+}(J = 1-0)$ (lower panel). The synthesized beam size ($1''.60 \times 2''.20$ at $PA = -81.2°$) is shown as the ellipse at the bottom left of each panel. *(Right side)* The intensity weighted velocity map for $\mathrm{HCN}(J = 1-0)$ (upper panel) and $\mathrm{HCO^+}(J = 1-0)$ (lower panel). Lower limit of the intensity is set to each map as 3σ. The velocity resolution of each image is approximately 3.3 km s^{-1}.

Table 2.2: ALMA observation parameters

Parameter		
Date	2012 Jul 29, Oct 19	
On-source time	105.24 minutes	
Configuration	extended (Cycle 0)	
Phase center:		
R. A.(J2000.0)	$02^{\mathrm{h}}46^{\mathrm{m}}19^{\mathrm{s}}.06$	
DEC.(J2000.0)	$-30^{\circ}16'29''.7$	
Primary beams	$69''$	
	LSB	USB
Frequency coverage (GHz)	85.400-89.104	97.271-100.917
Velocity resolution (km s^{-1})	1.7	1.5
Central frequency of		
each spectral window (GHz)	86.338, 88.166	98.209, 99.979

2.4 Method

The measurement procedure for the SMBH mass and its result are described in this section. We model a mass distribution of the galaxy with multiple Gaussians to express the combination of stellar mass profile and the SMBH mass. The gravitational potential is derived by following the equations described in Cappellari et al. (2002), which uses a Multi Gaussian Expansion (MGE) method. Circular velocity is calculated from the gravitational potential field by using MGE_circular_velocity code, which is in the JAM modelling package[2] of Cappellari (2008). The SMBH mass is estimated from the total mass profile, which gives a velocity field best matched to the observed result. When comparing the derived velocity profile with the observational results, we use the KINematic Molecular Simulation (KinMS, Davis et al., 2013) in order to consider disc properties (e.g., disc thickness, position angle, and inclination) and the observational effect of beam-smearing. We show the details of each procedure in the following sections.

2.4.1 Dynamical Modelling

(1) The Mass Model

We express the mass distribution as a summation of the SMBH mass and the stellar mass profile, expressed as the stellar luminosity distribution multiplied by a constant I-band stellar mass-to-light (M/L) ratio. Assuming that the galaxy is axisymmetric, the stellar luminosity distribution along the galaxy major axis is modelled as a superposition of Gaussian components, using the idea of Multi-Gaussian Expansion (Emsellem et al., 1994). The major axis defined here is at a position angle of 130° from de Vaucouleurs et al. (1991). We use an I-band image observed with the Advanced Camera for Surveys Wide

[2] http://purl.org/cappellari/idl

Field Channel F814W filter on *Hubble Space Telescope* (*HST*) to obtain the luminosity distribution at the major axis (black line in Figure 2.2). We subtract the contribution from the Active Galactic Nucleus (AGN) and flatten the starburst dominated region (both are shaded in Figure 2.2) in order to estimate the underlying stellar luminosity profile. The AGN profile is calculated by the convolution of a delta function with the Point Spread Function (PSF), measured to be $0''.2$ (full width half maximum, FWHM) from five unresolved stars in the same image. The PSF is also checked by using "Tiny Tim" package (version 6.3) developed by Krist et al. (2011). The luminosity value of the delta function is determined to obtain the residual luminosity distribution larger than 0 at any radius. Note that the AGN subtraction does not gravely affect the SMBH mass estimation. Even the peak before subtraction gives a mass of less than $6.00 \times 10^6 M_\odot$ for a M/L ratio 5.14, and it is at least one digit smaller than the SMBH mass we put in the model. The starburst ring region is determined to be in the range of radii from $-11''$ to $-7''$ and from $8''$ to $13''$ along the major axis. The ring includes younger stars than inside or outside of the ring, and is bluer in colour. We model the stellar luminosity profile by calculating the least-square value with the luminosity distribution without the ring and the AGN. The model (blue line in Figure 2.2), therefore, consists mainly of old stars, but does not include younger stars on the ring. See also Table 2.3 for MGE parameters we give for the data. The mass profile is simply modelled by multiplying the constant I-band M/L ratio to the modelled stellar luminosity profile and adding the assumed SMBH point mass in the center. Note again that we model older stars, by which means we are assuming that the radial difference of the M/L ratio is negligible.

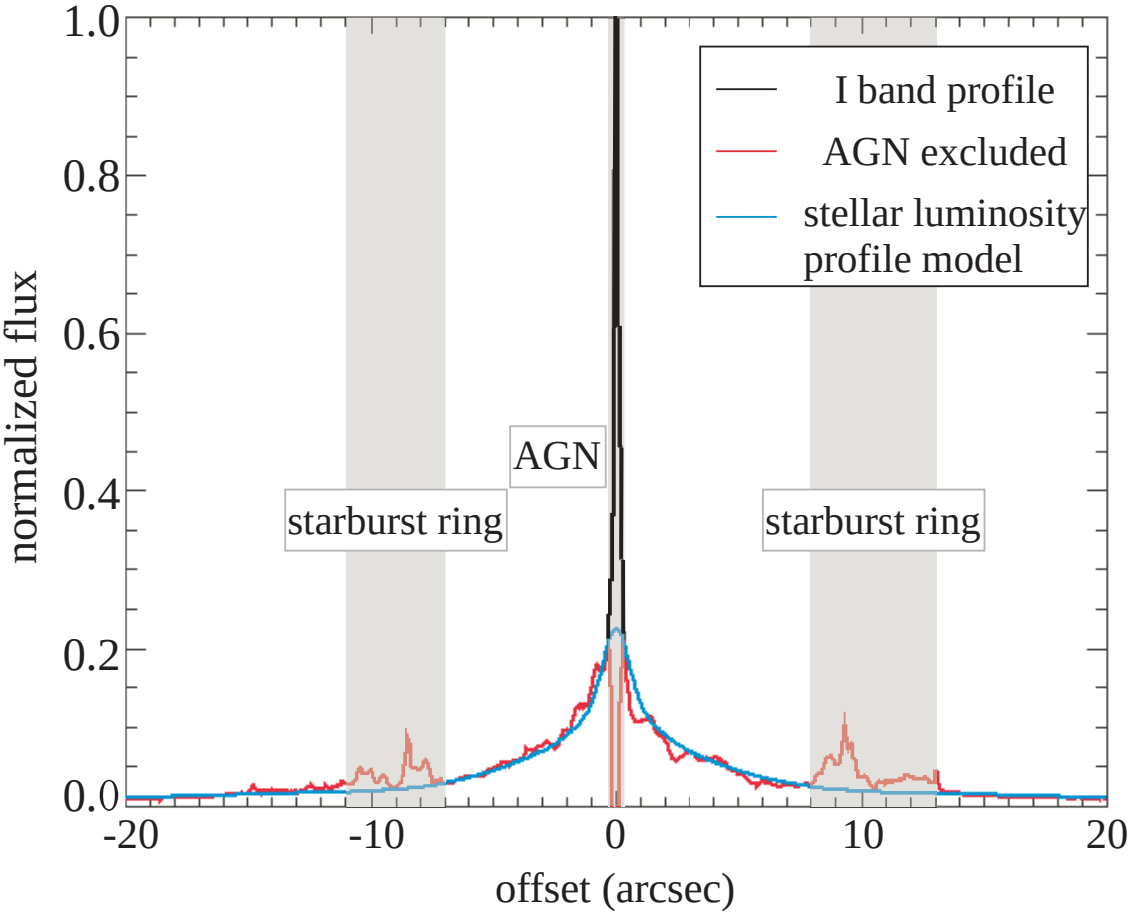

Figure 2.2: **NGC 1097 *HST* I-Band Luminosity Profile and Its Model:** The observed I-band luminosity distribution of *HST* F814W (black line), the distribution with the AGN subtracted (red line), and the modelled stellar luminosity profile (blue line). We run the least-square value calculation at all radii excluding the coloured regions to obtain the model profile. The starburst ring dominated regions (from $-11''$ to $-7''$ and from $8''$ to $13''$) and the central area where seems to have the luminosity dominated with the AGN (from $-0''.5$ to $0''.5$) are coloured with grey.

Table 2.3: MGE Parameters for the Stellar Luminosity Obtained from WFC F814W Surface Brightness of NGC 1097

j	$I_j(L_{\odot,I}/\mathrm{pc}^{-2})$	σ_j(arcsec)	q_j
1.....	7451.23	0.500	0.900
2.....	5122.72	3.50	0.700
3.....	3725.62	1.25	0.900
4.....	1862.81	16.0	0.700

See text for how we deal with the AGN and the starburst region.

(2) Velocity Field Calculation

With a given mass profile from Section (1), we calculate the velocity field from a gravitational potential field derived with equations from Cappellari et al. (2002). We use MGE_circular_velocity code, which is in the JAM modelling package of Cappellari (2008). The inclination angle is set to be $46°$ (Ondrechen et al., 1989). See Section 2.5.2 for more details regarding the inclination angle.

(3) Modelling a Position-Velocity Diagram (PVD)

We calculate a position-velocity diagram (PVD) model along the galaxy major axis by assuming that the observed molecular gas follows the velocity field obtained by our calculation. The observational effects are taken into account by utilizing KinMS (Davis et al., 2013). We convolve the model cloud distribution with our beamsize ($1''.60 \times 2''.20$) to express the beam-smearing, and assume the molecular gas disc to be an axisymmetric thin disc. The position angle of the galaxy major axis is set to be $130°$ (de Vaucouleurs et al., 1991), which is consistent with the kinematical position angle estimated from our observational data. The position angle is also consistent with the one calculated by Spitzer

Survey of Stellar Structure in Galaxies (S4G, Sheth et al., 2010), $-52°$, and global properties calculated via their pipeline 3 by Muñoz-Mateos et al. (2015). Note that we can mostly avoid the region with non-circular motion pointed out by Fathi et al. (2013) by using a PVD along the galaxy major axis. We assume that the streaming motion remaining in the PVD is negligible. We can also comment that when considering the error propagation for a simple equation of $v^2/2 = GM/r$, 10 percent error in the velocity could result in 20 percent error for the SMBH mass, which is consistent the error bar we derive from Figure 2.5.

2.4.2 Fitting and the Result

The observed PVD of $\mathrm{HCN}(J = 1 - 0)$ is shown in the upper panel of Figure 2.3 with colour filled contours. We set the kinematical position angle to be $130° \pm 5°$. The centre of the galaxy is assumed to be the peak of 6 cm observation (Hummel et al., 1987), 860 μm, and $\mathrm{HCN}(J = 4 - 3)$ observation (Izumi et al., 2013). We fit the observed PVD with PVD models calculated with 2 free parameters, the I-band M/L ratio and the SMBH mass. We find the two parameters to be around $M/L \sim 5.0$ and $M_{\mathrm{BH}} \sim 1.0 \times 10^8 M_\odot$ by initial robust-grid calculation. Then the finer grid of model parameters is set to be from $M/L = 4.80$ to 5.35 in steps of 0.01 and $M_{\mathrm{BH}} = 0.5 \times 10^8 M_\odot$ to $2.5 \times 10^8 M_\odot$ in steps of $0.1 \times 10^8 M_\odot$. We calculate an optimal rotation curve from the observed PVD above $3\sigma \sim 8$ mJy as follows: we make two cuts – one in the horizontal and one in the vertical direction. A cut in the vertical direction gives us a spectrum at the pixel whereas a cut in the horizontal direction gives us an intensity profile at that velocity. Peak positions for both are determined with the Gaussian fit. We use the points when the two are consistent, but abandon when they do not match. In the latter case the spectrum is not well characterized by a Gaussian because the asymmetric distribution of the molecular gas and the

beam smearing effect is skewing the profile. 106 points are extracted from the observed PVD (see Figure 2.3). The error bar along the velocity axis for each representative points of the PVD is defined to be a sum in quadrature of the channel width (3.284 km s^{-1}) and the error from Gaussian fitting. After fitting a Gaussian, to the spectrum at each position, we determine the error budget to be the range of all the channels which has an observed value within the difference of half of the noise level from the maximum value of the fitted Gaussian.

Chi-square values (χ^2) are calculated for each model for the 106 points in the observed PVD. Note that the degree of freedom becomes 104, because we have two free parameters, the SMBH mass and the I-band M/L ratio. Figure 2.4 shows the χ^2 value distribution in the parameter space. The contour level is defined to be $(2, 3, 4, 5, 6, 8, 12) \times (\chi^2_{\rm min})$. The smallest χ^2 of 113 (reduced χ^2; $\chi^2_{\rm red}$ is 1.09 when divided with the degree of freedom) is realized with parameters of $M_{\rm BH} = 1.40 \times 10^8 M_\odot$ and the I-band M/L ratio$= 5.14$. See Figure 2.3 to compare three PVD models in black contours and lines calculated with different values of parameters ($M_{\rm BH} = 0$, I-band M/L ratio$= 5.14$ for the left column, $M_{\rm BH} = 1.40 \times 10^8 M_\odot$, I-band M/L ratio$= 5.14$ for the middle column, $M_{\rm BH} = 7.00 \times 10^8 M_\odot$, I-band M/L ratio$= 5.05$ for the right column). The red contour in the upper panel shows the observed PVD by $\rm HCN(J = 1 - 0)$. Red dots in the middle panel represent the extracted points from the observed PVD. Residuals are plotted in the lower panels. The χ^2 are 244, 113, and 1090 ($\chi^2_{\rm red}$ are 2.35, 1.09, and 10.5) for each.

We determine the error bar for each parameter, M/L ratio and SMBH mass, by taking the parameter value within 99.73% confidence level ($\Delta\chi^2 \leq 9$, where $\Delta\chi^2 \equiv \chi^2 - \chi^2_{min}$). Figure 2.5 show the polynomial fit to the $\Delta\chi^2$ distribution for each parameter. In the left panel, the SMBH mass is thus estimated to be $1.40^{+0.27}_{-0.32} \times 10^8 M_\odot$ by considering all the values below the black straight line. The M/L ratio is estimated to be $5.14^{+0.03}_{-0.04}$ by

also considering values below the black straight line in the right panel. Note here that the derived SMBH mass is consistent with the one presumed from the $M_{\rm BH} - \sigma$ relation reported in (McConnell & Ma, 2013) and the central velocity dispersion (196 ± 5 km s^{-1}, Lewis & Eracleous, 2006)(see also Section 2.2.1).

2.5 Discussion

While we determine the SMBH mass and the I-band M/L ratio from the molecular gas dynamics, there are some uncertainties coming from the assumption we made when calculating the model. We discuss the effect of the observing band we use to model the stellar luminosity distribution in Section 2.5.1, how the inclination angle affects the result (Section 2.5.2), and what if we use a different emission line to observe the molecular gas dynamics (Section 2.5.3).

2.5.1 The Proper Stellar Luminosity Profile without the Dust Effect

We estimate the expected stellar mass profile by excluding the bright AGN profile and luminosity enhancement by the starburst ring (Section (1)), but we could not avoid the dust extinction effects, which could be important for this starburst galaxy with its prominent dust lane around the starburst ring. One way to mitigate the dust extinction effects is to observe at longer wavelengths such as the near infrared. NICMOS on *HST* has a narrow band filter F190N which observes at 1.9 microns. We calculate a velocity field from the assumed SMBH mass and the stellar mass profile derived from the luminosity profile of 1.9 microns, and obtain a PVD by following the method described in Section (3). We then compare the two PVDs calculated from the F190N luminosity profile and the F814W luminosity profile. Both luminosity profiles need to have the same PSF for a proper

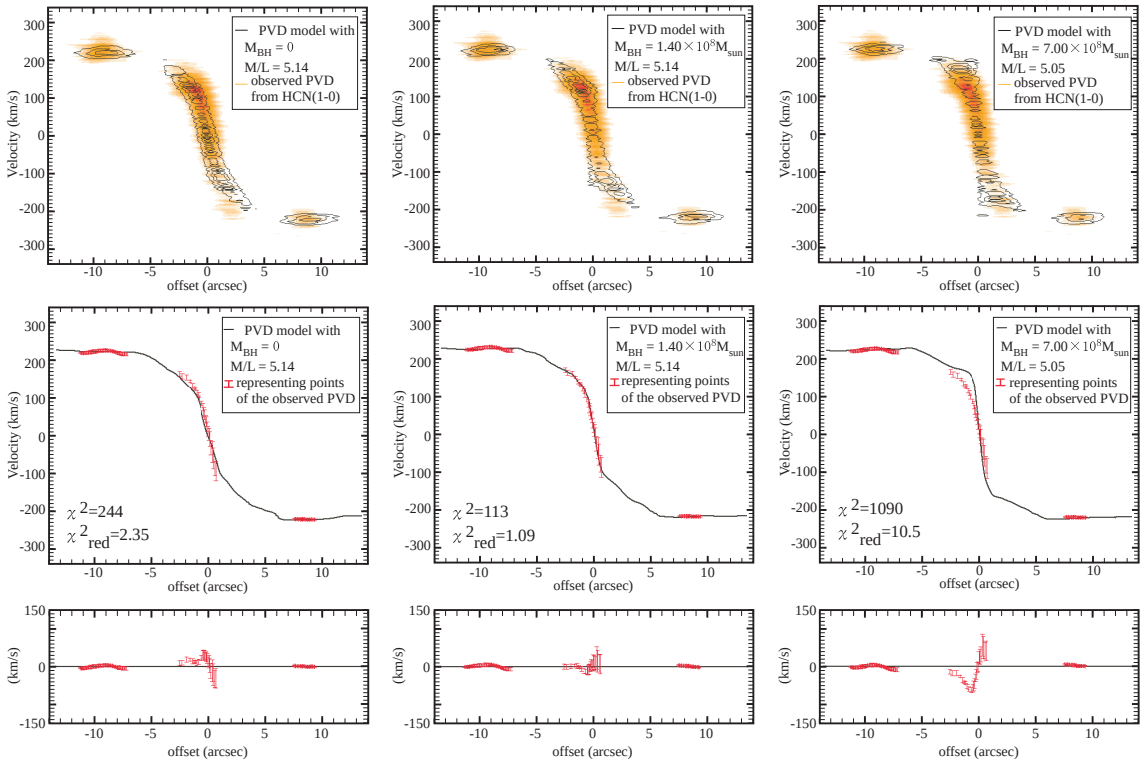

Figure 2.3: **PVDs and Velocity Fields of Different Parameter Sets:** *(Upper panels)* PVDs calculated with the parameter set of $M_{\rm BH} = 0$, M/L=5.14 (left), $M_{\rm BH} = 1.40 \times 10^8 M_\odot$, M/L=5.14 (middle), and $M_{\rm BH} = 7.00 \times 10^8 M_\odot$, M/L=5.05 (right). Black contours are for the modelled PVD, while colour filled contours show the observed PVD for $\rm HCN(J = 1 - 0)$. *(Middle panels)* Each black line shows the PVD model and grey dots show the representative points of the observed PVD. The points are extracted from the grey contours in the upper panel by fitting a Gaussian to the spectrum at each position. Here we fix the lower luminosity limit to represent the observed PVD as $3\sigma \sim 8.0\rm mJy$. We obtain $\chi^2 = 113$, which is the minimum value, for $M_{\rm BH} = 1.40 \times 10^8 M_\odot$ and M/L=5.14 (middle), while $\chi^2 = 244$ and 1090 for $M_{\rm BH} = 0, \rm M/L = 5.14$ (left), and $M_{\rm BH} = 7.00 \times 10^8 M_\odot, \rm M/L = 5.05$ (right). We also put the reduced chi-square value, which is a χ^2 divided with the degree of freedom of 104, as $\chi^2_{\rm red}$. *(Lower panels)* Residual between the black line and plots in the above panels of each.

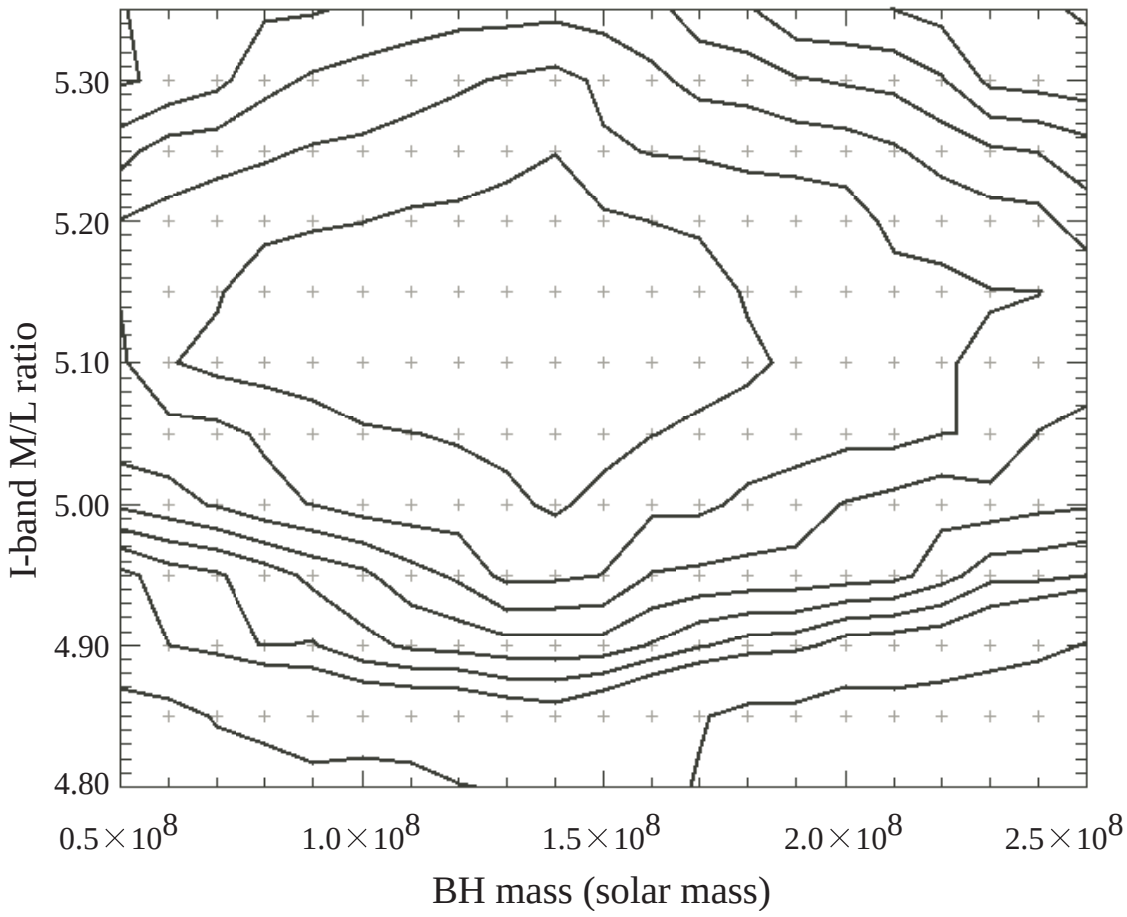

Figure 2.4: **Chi-square Distribution for $M_{\rm BH}$ and M/L Ratio:** χ^2 distribution of the grid calculation with two free parameters, the SMBH mass and the I-band M/L ratio. The inclination angle is fixed to $i = 46^\circ$ (Ondrechen et al., 1989). Grey dots show the parameter pair for modelling the PVD. The SMBH mass and the M/L ratio are fixed respectively with the range of $M_{\rm BH} = 0.50 \times 10^8 M_{\rm sun}$ to $2.50 \times 10^8 M_{\rm sun}$ in step of $0.50 \times 10^8 M_\odot$ and M/L=4.80 to 5.35 in step of 0.01. Contour levels are set to be $(2, 3, 4, 5, 6, 8, 12) \times \chi^2_{\rm min}$, where $\chi^2_{\rm min} = 113$ is determined by the minimum χ^2, realized with parameters of $M_{\rm BH} = 1.40 \times 10^8 M_\odot$ and M/L=5.14. We determine the error bar for each parameter by using Figure 2.5.

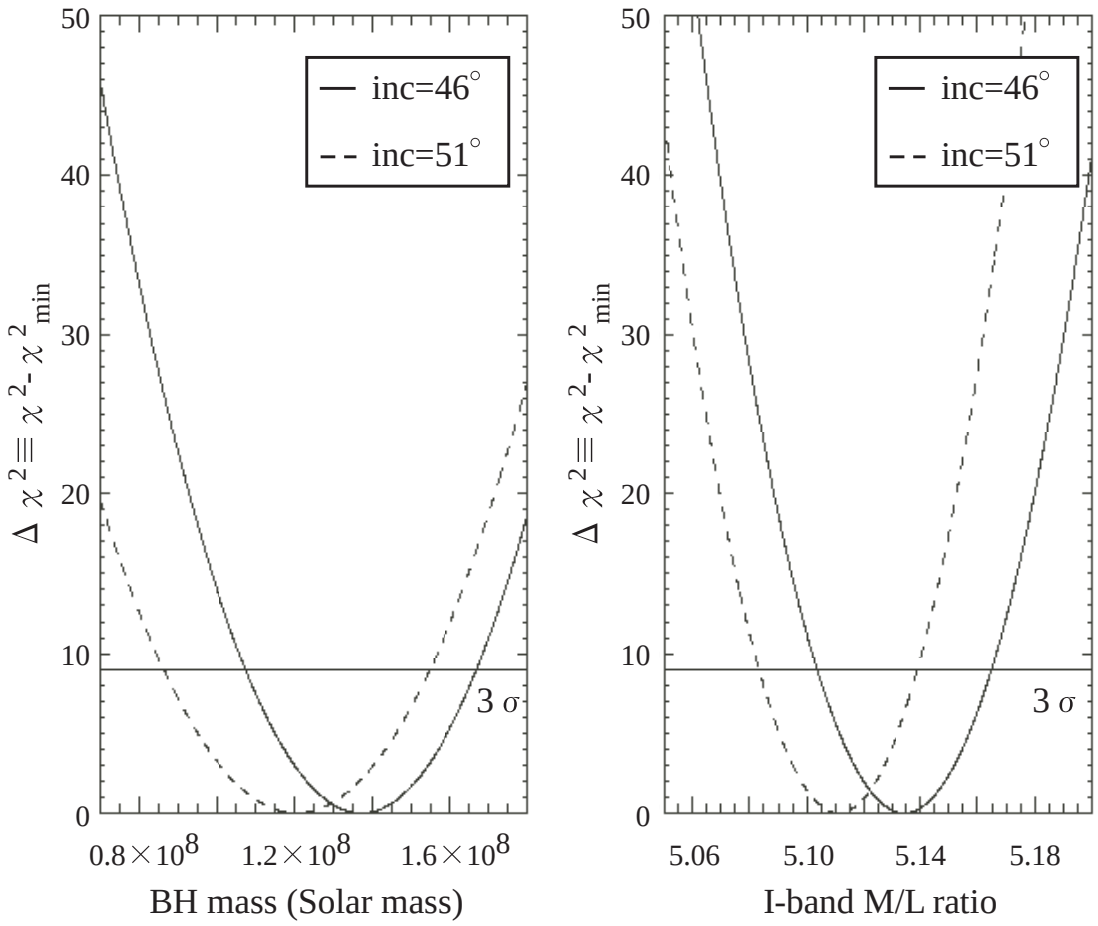

Figure 2.5: **Polynomial Fittings to the Chi-square Distribution:** Distributions of the $\Delta\chi^2 \equiv \chi^2 - \chi^2_{\rm min}$ for each parameter, the SMBH mass (left panel) and the I-band M/L ratio (right panel). Solid black curve shows the distribution calculated at the inclination angle of 46°. Dashed curve stands for the calculation for 51°. The error bar at 99.73% confidence level for each parameter is taken to be the values under solid straight line (3σ line, where $\Delta\chi^2 = 9$). For the inclination angle of 46°, the error bar for each is determined to be $M_{\rm BH} = 1.40^{+0.27}_{-0.32} \times 10^8 M_\odot$ and M/L= $5.14^{+0.03}_{-0.04}$, while $M_{\rm BH} = 1.20^{+0.35}_{-0.34} \times 10^8 M_\odot$ and M/L= 5.11 ± 0.03 for the inclination angle of 51°.

comparison. For the NICMOS data, which have a small field of view and no feasible stars available for a measurement of the PSF, we refer "Tiny Tim" package (version 6.3 Krist et al., 2011) and assume the shape as a Gaussian with its FWHM of $0''.4$. We convolve the I-band luminosity distribution with this PSF. Figure 2.6 shows the luminosity distribution of the PSF-convolved I-band and 1.9 microns normalized by each maximum value (upper panel) and the difference of two profiles (lower panel). This comparison already shows that the difference between the two luminosity profiles is negligible. We also examine the S4G data at 3.6 microns to compare the stellar profile with the *HST* data but the *Spitzer* Infrared Array Camera (IRAC) PSF is too large ($\sim 1''.8$) to do any detailed comparison.

We normalize the peak luminosity at 1.9 microns to the I-band peak, and then subtract the luminosity enhancement of the AGN, as described in Section (1). We also ignore the starburst region and use the same M/L ratio to calculate the velocity field for the two stellar mass profiles. We find that a $M_{\rm BH} = 1.40 \times 10^8 M_\odot$ and M/L$= 5.14$ gives the best-fit value for an inclination of $46°$. The PVDs calculated as such are shown in Figure 2.7. Black and gray contours in Figure 2.7 are the PVD calculated from two stellar mass profile models – these do not differ much between the two luminosity profiles. We therefore conclude that the dust extinction effect with the F814W filter is not too serious for the measurement of the SMBH mass.

2.5.2 Effect from the Inclination Angle

We discuss briefly on the difference coming from how we set the inclination angle. The accuracy of the inclination angle is critical for calculating the velocity and therefore crucial for the SMBH mass estimation. It is however not straightforward to determine the inclination angle when comparing observations at different field of view. Previous studies of NGC 1097 have determined a dynamical inclination angle of $46 \pm 5°$ (HI observations

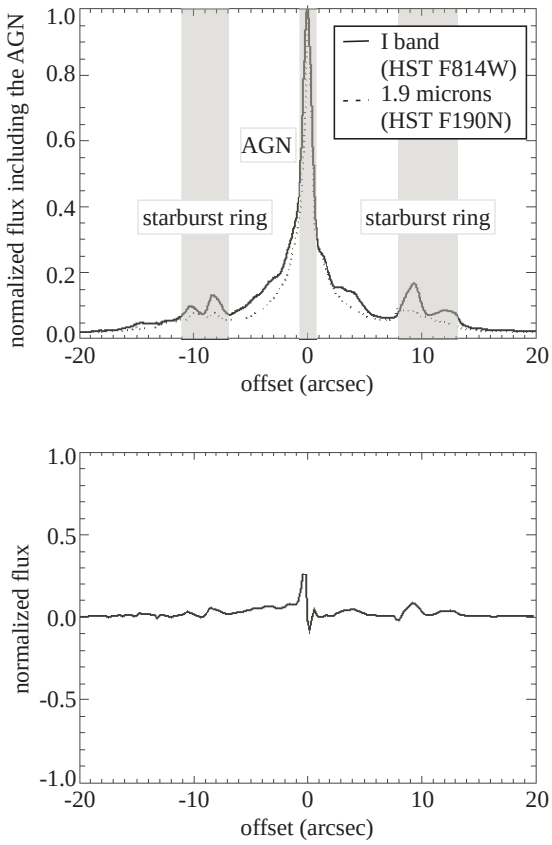

Figure 2.6: **NGC 1097 *HST* Luminosity Profile at Two Bands:** *(Upper panel)* The observed luminosity profile of I-band (indicated with solid line, *HST* F814W observation) and 1.9 microns (dotted line, *HST* F190N observation). The luminosity value is normalized to compare the intrinsic profile. I-band (F814W) profile is convolved with the assumed point spread function (PSF) of F190N. As discussed in Section (1), we shade the starburst ring region and the AGN dominated region. *(Lower panel)* Residual of the two luminosity distribution showing a good agreement of the two.

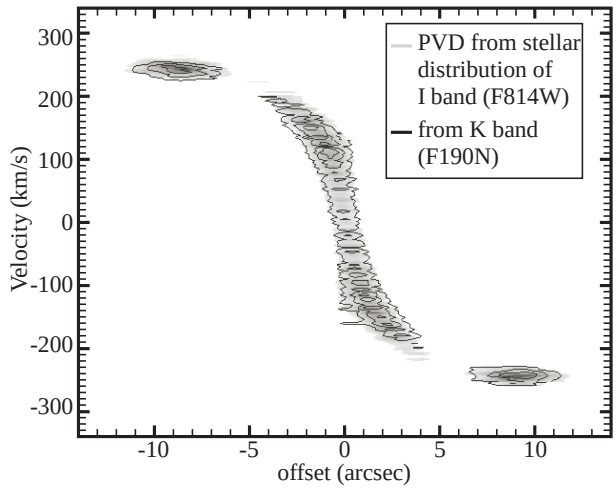

Figure 2.7: **NGC 1097 PVDs From Two Stellar Mass Distributions:** Grey filled contours show the PVD calculated from I-band luminosity profile multiplied by the M/L ratio and black contours are the one from 1.9 microns luminosity profile multiplied by the M/L ratio. Parameters for the calculation is set to be $M_{\rm BH} = 1.40 \times 10^8 M_\odot$ and M/L=5.14, the best-fit value at the inclination $46°$. PVD does not largely differ between the two stellar distribution obtained from different wavelength.

at 3 kiloparsec scales, Ondrechen et al., 1989), or $34°$ (Hα line profile study, Storchi-Bergmann et al., 2003). Hsieh et al. (2011) reported that the inclination angle of NGC 1097 is $41.7 \pm 0.6°$ using the kinematic parameters of $^{12}\mathrm{CO}(J = 2 - 1)$ observed with Submillimeter Array (*SMA*). They argue that the circumnuclear ring is nearly circular for the inclination of $\sim 42°$, by which means the ring has an intrinsic elliptical shape in the galactic plane, of which case is not symmetric to the axis. Though the suggested asymmetry is interesting to note, we would like to leave it as a further discussion, since in this work we assume an axisymmetric distribution for stars and molecular gas when calculating the circular velocity field. This time we assume the galaxy inclination angle to be $46 - 51°$ by referring to Ondrechen et al. (1989) and the axis ratio of the HST I-band observation. We evaluate the SMBH mass to be $1.40^{+0.27}_{-0.32} \times 10^8 M_\odot$ and the the I-band M/L ratio to be $5.14^{+0.03}_{-0.04}$ at the inclination angle of $46°$, with $\chi^2 = 113$ ($\chi^2_{\rm red} = 1.09$ when divided with the degree of freedom 104). We also follow the same process in Section 2.4 with the

inclination angle of 51° and evaluate the SMBH mass to be $1.20^{+0.35}_{-0.34} \times 10^8 M_\odot$ and the I-band M/L ratio to be 5.11 ± 0.03 with $\chi^2 = 117$ ($\chi^2_{\rm red} = 1.13$). See also dashed curves in Figure 2.5 for the χ^2 distribution, used to determine the error bar for each parameter.

We can also consider the case of the inclination angle is $34 - 41^\circ$ by multiplying a factor of $\sin(i_{\rm intrinsic})/\sin(46^\circ) \sim 0.78 - 0.91$ to the velocity where we write $i_{\rm intrinsic}$ as an inclination angle of the observed component. Under the simplified assumption that the SMBH mass is proportional to the square of the velocity, we can estimate the change of the SMBH mass to be smaller than $0.31 \times 10^8 M_\odot$, which is mostly included in the error bar of our result $1.40^{+0.27}_{-0.32} \times 10^8 M_\odot$. We therefore consider that it is not crucial to count this error into our error budget. Note that, however, this galaxy could have a warped or a misaligned structure, which could be interesting to investigate but requires a calculation for an asymmetric potential field.

2.5.3 SMBH Mass Estimation from Other Molecular Species

Our main result is obtained using the HCN line because it had the highest signal-to-noise ratio (SNR). It is important to measure the SMBH mass from other molecular species as well for consistency. We therefore repeat our method using the $\mathrm{HCO^+}(J = 1 - 0)$ emission line.

We apply the fitting procedure described in Section 2.4.2 to the PVD for $\mathrm{HCO^+}(J = 1-0)$, and estimate the SMBH mass to be $(1.40 \pm 0.30) \times 10^8 M_\odot$ and the I-band M/L ratio to be 5.15 ± 0.03 with a galaxy inclination of 46°. These derived values are consistent with the measurement using $\mathrm{HCN}(J = 1 - 0)$. From Figure 2.8, we see that the observed PVDs of two molecular gases are in good agreement, indicating that the fitting parameters will be consistent between the two.

Reaching the velocity structure from multiple molecular species is one of the partic-

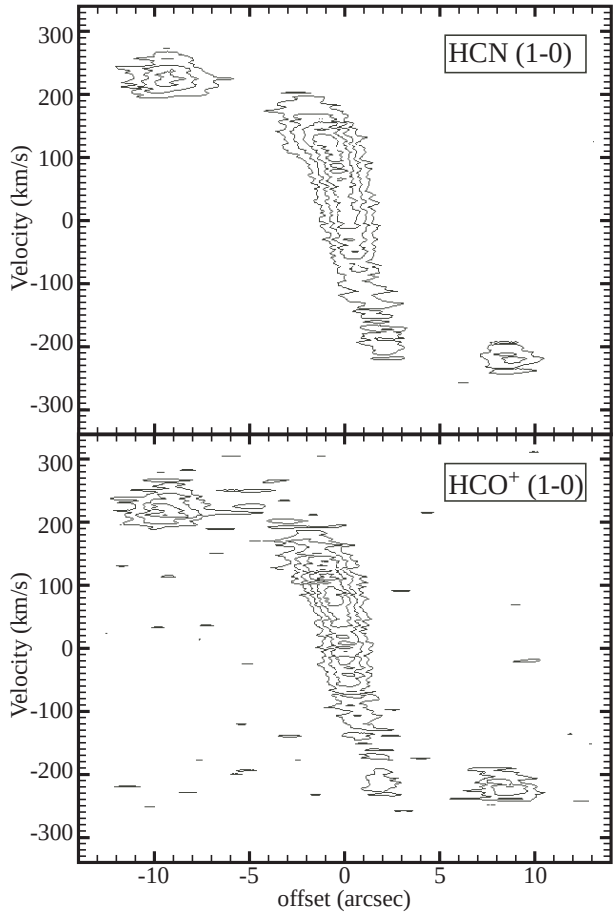

Figure 2.8: **NGC 1097 PVD of** $\mathrm{HCN}(J = 1 - 0)$ **and** $\mathrm{HCO}^{+}(J = 1 - 0)$**:** The observed PVD of $\mathrm{HCN}(J = 1 - 0)$ (upper panel) and $\mathrm{HCO}^{+}(J = 1 - 0)$ (lower panel) is respectively shown with black contours. The contour level of both is from 1σ to 4σ where $1\sigma = 4.6$ mJy for $\mathrm{HCN}(J = 1 - 0)$ and $1\sigma = 3.2$ mJy for $\mathrm{HCO}^{+}(J = 1 - 0)$. The velocity structure of these two PVDs are in good agreement.

ular benefit of the SMBH mass measurement with millimeter/submillimeter wavelength observation, which enable one to observe more than two molecular species at the same frequency band.

2.6 Conclusion

We derive the SMBH mass in NGC 1097 to be $1.40^{+0.27}_{-0.32} \times 10^8 M_\odot$ by using dense molecular gas dynamics traced with $\mathrm{HCN}(J = 1 - 0)$ and $\mathrm{HCO}^+(J = 1 - 0)$ observed with ALMA. The value of SMBH mass is measured with two emission lines is in good agreement, indicating the applicability of this method to any nearby galaxy with detectable molecular gas. Furthermore, the mass is consistent with $M_{\mathrm{BH}} - \sigma$ relation (McConnell & Ma, 2013) from the velocity dispersion observed by Lewis & Eracleous (2006). We can comment that the derived mass does not coincide with the $M_{\mathrm{BH}} - \sigma$ relation for early-type galaxies, but for mixed samples and for late-type galaxies.

The dust extinction effect does not significantly affect the measurement of the SMBH mass. The inclination angle, however, could affect the SMBH mass when we observe the rotational motion with better resolution. In this work we assumed the molecular gas disc morphology and only used the rotation curve when comparing the model and observation. This can be refined with more parameters, while the work requires computationally an expensive fitting process.

As millimeter/submillimeter interferometers develop their angular resolution and sensitivity, this method will provide more samples, especially late-type galaxies with their central gas dynamically well relaxed, to correlations between SMBH mass and galaxy properties such as $M_{\mathrm{BH}} - \sigma$ relation. Increasing the number of galaxy samples in $M_{\mathrm{BH}} - \sigma$ relation will lead us to higher accuracy of the correlation, which suggests the coevolution process of galaxies and BHs.

Chapter 3

Some improvements on the method – application to NGC 3665

3.1 Abstract of this Chapter

Citing from our work (Onishi et al., 2016), I here present a measurement of the mass of the supermassive black hole (SMBH) in a nearby fast-rotator early-type galaxy NGC 3665. We obtained Combined Array for Research in Millimeter Astronomy (CARMA) B and C array observations of the ^{12}CO$(J = 2 - 1)$ emission line with a combined angular resolution of $0''.59$. We analyse and model the three-dimensional molecular gas kinematics, obtaining a best-fit SMBH mass $M_{\rm BH} = 5.75^{+1.49}_{-1.18} \times 10^8\ M_\odot$, a mass-to-light ratio at H-band $(M/L)_H = 1.45 \pm 0.04\ (M/L)_{\odot,H}$, and other parameters describing the geometry of the molecular gas disc (statistical errors, all at 3σ confidence). We estimate the systematic uncertainties on the stellar M/L to be $\approx 0.21\ (M/L)_{\odot,H}$, and on the SMBH mass to be $\approx 0.4 \times 10^8\ M_\odot$.

The measured SMBH mass is consistent with that estimated from the latest correlations with galaxy properties. Following works described in Davis et al. (2013) and Onishi

et al. (2015), we also analysed and modelled the kinematics using only the major-axis position-velocity diagram (PVD), and conclude that the two methods are consistent.

3.2 Introduction

Motivated by the importance of measuring SMBH masses to further constraint the $M_{\rm BH} - \sigma$ relation, we have established a method to use dynamics of molecular gas (Davis et al., 2013; Onishi et al., 2015). Both of the works derived the SMBH mass by using PVDs and rotation curves extracted by the PVD. The SMBH masses were constrained with good accuracy (e.g., 20% error for Onishi et al. 2015), although some assumptions are made for the model. For instance, Onishi et al. 2015 reported the molecular gas disc property as a possible error source.

We thus improve our fitting method to use the entire data cube for the fitting, and to explore a larger parameter space including molecular gas disc properties. Aiming to expand the possible applicable galaxy types, we select a nearby fast-rotator early-type galaxy NGC 3665, observed at ^{12}CO$(J = 2 - 1)$ emission line with CARMA. The new fitting method will improve to estimate a more realistic error budget, and will further generalize the SMBH mass measurement.

The observations and data reduction are described in Section 3.3. The SMBH mass measurement method is explained in Section 3.4. Section 3.5 contains a discussion of galaxy morphology (Section 3.5.1), AGN activity (Section 3.5.2), possible error sources on the SMBH mass (Section 3.5.3), and a comparison of the SMBH masses derived using different fitting methods (Section 3.5.4). The conclusions are summarized in Section 3.6.

3.2.1 The target – NGC 3665

NGC 3665 is a nearby fast-rotator early-type galaxy (Emsellem et al., 2011). We adopt a distance of 34.7 Mpc, estimated from the Tully-Fisher relation by Theureau et al. (2007), yielding a scale of ≈ 167 pc arcsec^{-1}. This distance is in good agreement with the estimate of 33.1 Mpc from its recession velocity[1] by Cappellari et al. (2011). Basic properties of the galaxy are summarised in Table 3.1. Twin jets emanating from the galaxy nucleus were observed with arcsecond resolution at 1.5 GHz using the Very Large Array (VLA; Parma et al. 1986), while a point-like structure was observed with 2 milli-arcsecond resolution at 5 GHz using the Very Long Baseline Array (VLBA; Liuzzo et al. 2009), both proving the existence of a central SMBH. We adopt the position of this point-like structure as the galaxy centre: RA=11:24:43.624, Dec=38:45:46.278 (Liuzzo et al., 2009).

Hubble Space Telescope (*HST*) observations in H-band (NICMOS F160W; see the left panel of Fig. 3.1) show prominent and regular dust lanes circling the galaxy centre, suggesting a gaseous disc-like structure extending to a radius of at least $8''$ from the nucleus. Previous CARMA observations revealed a regularly rotating molecular gas disc of the same radius (Alatalo et al., 2013). We therefore expect a central SMBH surrounded by a relaxed molecular gas disc, ideal to measure the SMBH mass using molecular gas kinematics.

NGC 3665 does not have a SMBH mass measurement yet, but has an effective stellar velocity dispersion of $\sigma_{\rm e} = 216 \pm 10$ km s^{-1}, reliably measured through integral-field spectroscopy (Cappellari et al., 2013a). Adopting the $M_{\rm BH} - \sigma$ relation of McConnell & Ma (2013), this suggest a SMBH mass of $\approx 3 \times 10^8\ M_\odot$ and thus a SMBH sphere of influence (SOI; $R_{\rm SOI} \equiv GM_{\rm BH}/\sigma^2$, where G is the gravitational constant) of ≈ 30 pc or

[1]The choice of the distance does not influence our conclusions but sets the scale of our models in physical units. Specifically, lengths and masses scale as D, while M/Ls scale as D^{-1}.

Table 3.1: NGC 3665 properties.

Parameter	Value	Reference
Morphology	fast rotator early type	Emsellem et al. (2011)
Position		Liuzzo et al. (2009)
R. A. (J2000.0)	$11^{\mathrm{h}}24^{\mathrm{m}}43\overset{\mathrm{s}}{.}624$	
DEC. (J2000.0)	$38°45'46''.278$	
Systemic velocity (km s^{-1})	2069	Cappellari et al. (2011)
Position angle (°)	26	Onishi et al. (2016)
Inclination angle (°)	$69.9^{+0.51}_{-0.39}$	Onishi et al. (2016)
Distance (Mpc)	34.7 ± 6.8	Theureau et al. (2007)
Linear scale (pc arcsec^{-1})	167 ± 33	Theureau et al. (2007)

$\approx 0''.2$, that is 3 times smaller than the synthesised beam size of the current observation (see Section 3.3).

3.3 Observation and Data Reduction

NGC 3665 was observed at the wavelength of the ^{12}CO$(J = 2 - 1)$ line using CARMA in the B (baselines 63–947 m) and C (baselines 26–370 m) arrays. Observations were carried out from April 11th to 21st 2013 (B array) and from November 26th to December 14th 2013 (C array). Total on-source time was 1610.6 min in the B array and 290 min in the C array. The receivers were tuned to cover the frequency range 214.404–215.373 GHz and 228.576–229.545 GHz in the lower (LSB) and upper (USB) sidebands, respectively, with 4 spectral windows per range. With 31 channel per spectral window, the frequency resolution was thus 7.812 MHz per channel. The field of view (full width at half maximum, FWHM, of the primary beam) at these frequencies was $31''$ for the 10-m antennae.

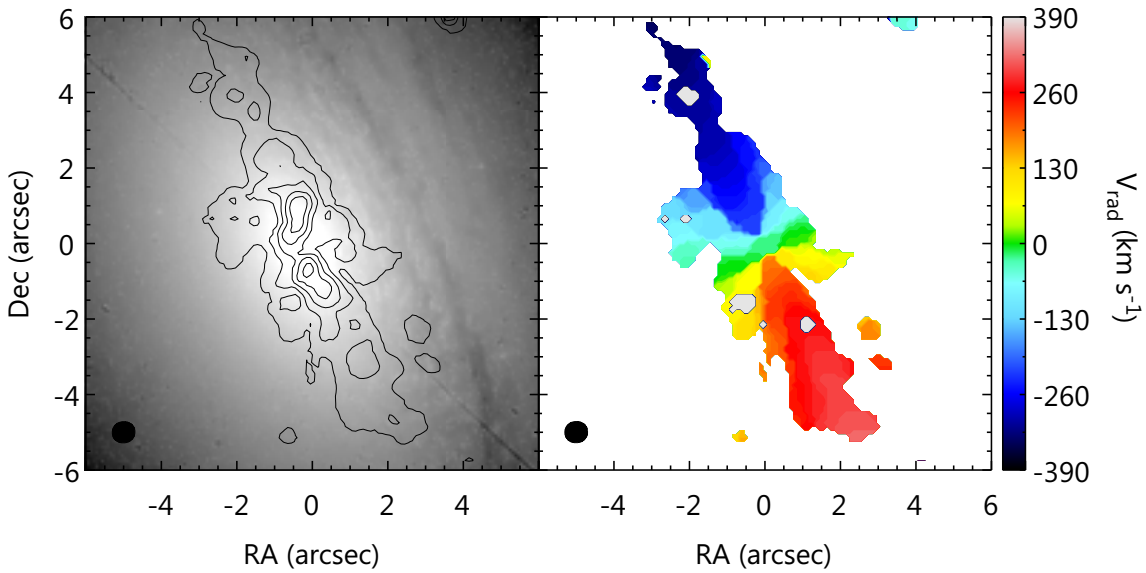

Figure 3.1: **NGC 3665 Moment 0 and 1 Maps:** *Left panel:* Integrated intensity map of CO$(J = 2 - 1)$ in NGC 3665 (contours), overlaid on an *HST* H-band (NICMOS F160W) unsharp-masked image. Contour levels are 0.3, 0.9, 1.5, 2.1 and 2.7 Jy beam^{-1} km s^{-1}, while the peak flux is 3.3 Jy beam^{-1} km s^{-1}. *Right panel:* Intensity weighted (mean) velocity map of CO$(J = 2 - 1)$. The map extent is set to the lowest contour level of the integrated intensity map. The synthesised beam ($0''.60 \times 0''.56$ at a position angle of $-81°$) is shown in the bottom-left corner of each panel.

Table 3.2: CARMA Observation Parameters.

Parameter	B array	C array
Date	Nov-Dec 2013	Apr 2013
On-source time (min)	1610.6	290
Phase center:		
RA(J2000.0)	$11^{\rm h}24^{\rm m}43\overset{\rm s}{.}6$	
DEC(J2000.0)	$38°45'46''.278$	
Primary beam	$31''$	

	LSB	USB
Frequency coverage (GHz)	214.404–215.373	228.576–229.545
Velocity resolution (km s^{-1})	10.9	10.2

The observational parameters are summarized in Table 3.2.

We followed the data reduction and analysis method described in Alatalo et al. (2013) using the Multichannel Image Reconstruction Image Analysis and Display (MIRIAD) package (Sault et al., 1995). The visibility data were first edited and calibrated using Mars, MWC 349, and 3C 273 as flux calibrators and 1153+495 as phase calibrator. The bandpass calibrator was 3C 279 or 3C 273. We then subtracted the continuum by assuming the CO emission to be present from -450 to 450 km s^{-1} with respect to the galaxy systemic velocity of 2069 km s^{-1} (Cappellari et al., 2011), and subtracting a linear fit to the line-free channels. The resulting cube was cleaned using the MIRIAD task MOSSDI2 with a threshold of 1.5 times the rms noise, measured in line-free regions of the cube. For imaging, we set the robustness parameter to 0.5, yielding a synthesised beam FWHM of $0''.60 \times 0''.56$ (≈ 100 pc $\times$ 93 pc) at a position angle of $-81°$, that was

properly sampled with $0''.2 \times 0''.2$ pixels. This provides a compromise between angular resolution and sensitivity, and the rotational motion of the molecular gas in the galaxy nucleus is then clearly detected. We did not bin the velocity channels, yielding a velocity resolution of 7.8 MHz or $\approx$ 10 km s^{-1} per channel, and the average rms noise per channel was 4.1 mJy beam^{-1}. Molecular gas emission was finally detected from -370 to 380 km s^{-1}.

Integrated intensity (moment 0) and intensity-weighted (mean) velocity (moment 1) maps can be created directly from this cube, but as most of the cube is devoid of emission, the resulting maps are of poor quality. Instead, we optimised the moments by first Hanning-smoothing the data cube in velocity and then smoothing it spatially with a Gaussian of FWHM equal to that of the synthesised beam. A mask was then created by selecting all pixels in the smoothed data cube above a threshold of 0.75 times the rms noise in each channel. The adopted integrated intensity and mean velocity maps, shown in Figure 3.1, were then created by calculating the moments of the original unsmoothed data cube within the mask region only.

The integrated intensity map reveals a centrally-concentrated molecular gas distribution, rapidly decreasing with radius. However, the inner $\approx 2''$ clearly show two separate concentrations on either side of the nucleus (see Fig. 3.1, left panel). This suggests a void in the very centre of the galaxy, where the intensity may remain above zero simply due to the angular extent of the synthesised beam. This central hole is confirmed by our modelling and further discussed in Section 3.5.1. The mean velocity map (Fig. 3.1, right panel) reveals very regular disc-like rotation with a total velocity width of ≈ 750 km s^{-1} and no evidence of any significant non-circular motion, warp or kinematic twist.

Interestingly, the molecular gas distribution and dust lanes revealed by *HST* are not very well associated with each other (see Figure 3.1, left panel). The kinematic major axis

of the molecular gas and the major axis of the dust lanes are however aligned, suggesting that the molecular gas disc and dust are nevertheless in the same plane. Both also align well with the large-scale photometric major axis, suggesting that this plane is also the large-scale equatorial plane of the galaxy. The differing distributions of the molecular gas and dust may thus be due to missing flux in the interferometric data, due to the lack of truly short baselines. Indeed, comparing the flux from our observations integrated over the CO$(2-1)$ Institut de Radioastronomie Millimetrique (IRAM) 30-m telescope beam (42.3 Jy km s^{-1}) to an actual IRAM 30-m integrated flux measurement (67.1 Jy km s^{-1}; Young et al. 2011), our CARMA high-resolution observations may be resolving out $\approx 40\%$ of the flux in extended structures.

3.4 Method

In this section, we describe the procedures employed to measure the SMBH mass in NGC 3665 and state our results. To summarise, we modelled the three-dimensional stellar mass distribution of the galaxy by deprojecting a two-dimensional model of the observed surface brightness and assuming a constant mass-to-light ratio M/L. The circular velocity curve arising from this mass model and a putative SMBH was then fed into a code simulating the resulting data cube, taking into account the molecular gas distribution and instrumental effects. The SMBH mass was then determined by simply comparing a range of models to the observations.

3.4.1 Velocity Model

The galaxy mass distribution is assumed to be the sum of a central SMBH and the large-scale stellar body of the galaxy. The SMBH is treated as a point mass whose mass is

free. For the stars, we combine *HST* (NICMOS F160W) and Two Micron All-Sky Survey (2MASS) H-band images, allowing to accurately trace the stellar surface brightness to a radius of $\approx 40''$. We adopt the Multi Gaussian Expansion (MGE) method (Emsellem et al., 1994; Cappellari et al., 2002) and fit this two-dimensional image with a sum of Gaussians (MGE_FIT_SECTORS procedure[2] of Cappellari (2002)). Given an inclination each Gaussian can be deprojected analytically, and the three-dimensional light distribution of the model can thus be trivially reconstructed. Here all the Gaussians are constrained to have the same position angle and inclination, resulting in an axisymmetric light model.

The point spread function (PSF) of each image is also fit with a sum of (circular) Gaussians and used as input during the MGE fit to obtain a deconvolved light model of the galaxy. We use the Tiny Tim package (version 6.3) developed by Krist et al. (2011) to measure the *HST* NICMOS PSF of the F160W filter. The FWHM of the 2MASS H-band PSF was assumed to be $2''.8$[3]. The prominent dust lane seen in the *HST* image is masked to mitigate the effects of dust obscuration, and the region outside a radius of $6''$ in the *HST* image is ignored and overwritten with the 2MASS image. Figure 3.2 shows a comparison of the best-fitting MGE model and the observed surface brightness distribution of the galaxy, from both 2MASS and *HST*. We follow the photometric calculation described in Section 5.2 of Thatte & et al. (2009) to convert the flux units from counts pixel^{-1} second^{-1} to $L_\odot$ pc^{-2}, and the resulting MGE parameters are listed in Table 3.3. We adopt an H-band solar Vega magnitude $M_{\odot,H} = 3.32$ from Table 1 of Blanton & Roweis (2007).

The gravitational potential of the galaxy is calculated from the summation of the MGE model components multiplied by a constant M/L and the SMBH modelled as

[2]Available from http://purl.org/cappellari/software

[3]http://spider.ipac.caltech.edu/staff/roc/2mass/seeing/seesum.html

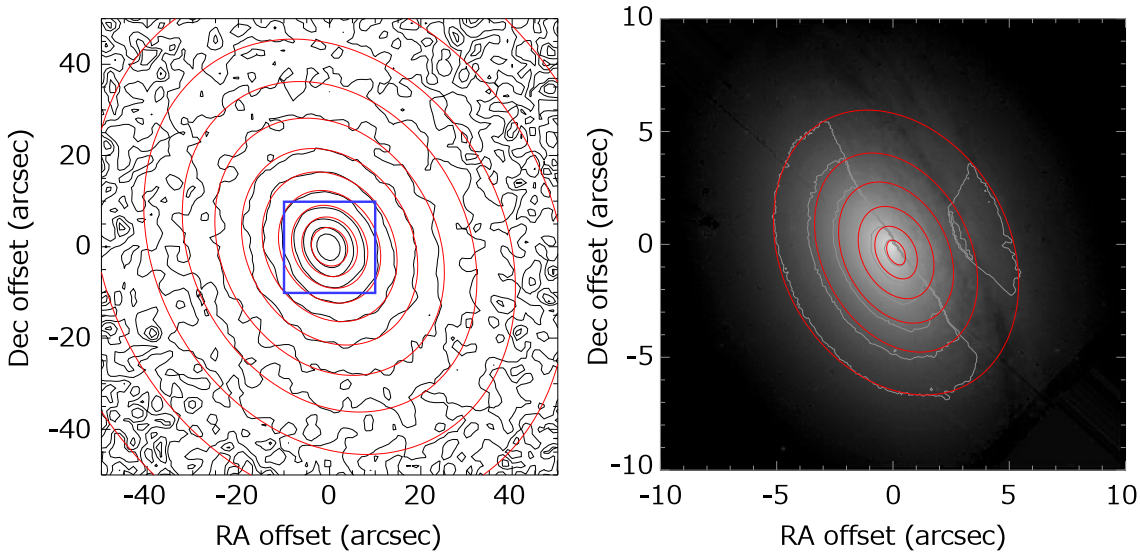

Figure 3.2: **NGC 3665 *HST* H-band Image and MGE Model:** *Left panel:* 2MASS H-band image (black contours) overlaid with our MGE model (red contours; Table 3.3). *Right panel:* Our MGE model (red contours) of the central $10''$ (blue box in the left panel), overlaid to *HST* H-band (NICMOS F160W) image (grey contours and grey scale image). The masked region (due to dust) is identified without the grey contours.

Table 3.3: MGE Components of the *HST* NICMOS F160W and 2MASS H-band Images.

j	I_j ($L_{\odot,H}$ pc^{-2})	σ_j (arcsec)	q_j
1.....	25551.5	0.227	0.515
2.....	21118.8	0.661	0.608
3.....	7436.97	1.31	0.887
4.....	12016.7	2.17	0.576
5.....	5862.67	4.76	0.837
6.....	741.344	11.3	0.441
7.....	807.669	19.2	0.780
8.....	212.118	48.6	0.821

a point like mass, by following the equation in Cappellari et al. (2002). The circular velocity curve in the equatorial plane is then calculated from this by using the ; MGE_CIRCULAR_VELOCITY procedure within the Jeans Axisymmetric Modelling (JAM) package[4] (Cappellari 2008).

Our assumption of a spatially constant M/L should be treated with caution given that the molecular gas disc (and potentially associated star formation) extends to the nucleus of NGC 3665 (Davis et al., 2014). The effect of any uniform star formation or young stellar population in the region of interest is implicitly subsumed into our adopted M/L, but a steep gradient could be problematic. However, neglecting centrally-concentrated star formation, and thus a decreasing M/L with decreasing radius, effectively overestimates the stellar contribution to the total mass in the very centre. Our SMBH mass estimates are thus conservative. The effects of a potentially varying M/L will be further explored in Davis & McDermid (2017).

3.4.2 Creating the Model Data Cube

Given the circular velocity curve obtained from the MGE formalism described above (Section 3.4.1), and the adopted molecular gas disc inclination (which is the same as that used to de-project our MGE models), we generate a model data cube using the Kinematic Molecular Simulation (KinMS) code of Davis et al. (2013)[5]. This assumes circular motions and a spatially uniform (but free) gas velocity dispersion. Instrumental effects such as beam-smearing and spatial and velocity binning are all taken into account by KinMS. For the properties of the molecular gas disc, we further assume that it has an exponential surface brightness profile with a void in the centre. The three free parameters describing the molecular gas distribution are thus its surface brightness scaling factor, radial scale

[4]http://purl.org/cappellari/software

[5]https://github.com/TimothyADavis/KinMS

Table 3.4: Model Parameters.

Parameter	Search Range	Best Fit	Error (1σ conf.)	Error (3σ conf.)
SMBH mass ($10^8 M_\odot$)	0.01–50.12	5.75	$+0.42, -0.38$	$+1.49, -1.18$
Stellar M/L ($M/L_{\odot,H}$)	0.10–4.00	1.45	± 0.01	± 0.04
Molecular gas disc:				
Centre X offset (arcsec)	-3.50–3.50	-0.25	± 0.01	± 0.02
Centre Y offset (arcsec)	-3.50–3.50	0.02	± 0.01	± 0.03
Inclination (°)	67.00–89.00	69.90	± 0.20	± 0.61
Position angle (°)	0–50	26	± 0	± 1
Centre velocity offset (km s^{-1})	-50.00–50.00	-8.12	± 0.75	± 2.50
Velocity dispersion (km s^{-1})	1.00–20.00	12.53	± 0.74	± 2.09
Luminosity scaling	10.00–200.00	86.16	± 2.91	± 8.63
Scale length (arcsec)	1.00–7.00	2.11	± 0.01	± 0.03
Central void radius (arcsec)	0.01–0.90	0.38	± 0.03	± 0.04

Notes: The prior distribution of each parameter, shown in the second column, is assumed to be uniform in linear space (logarithmic for the SMBH mass only). The posterior distribution of each parameter is quantified in the third to fifth columns (but see also Figure 3.3). Please see text for the error estimation of 1σ (68.3%) and 3σ (99.7%) confidence. The central offset (X, Y) is an offset between the model and VLBI observations (Liuzzo et al., 2009).

radius and the radius of the central hole. The other free parameters required to fully describe a model (or, rather, to allow its comparison to real data) are the kinematic centre and position angle of the molecular gas disc in the plane of the sky and the galaxy systemic velocity. The total list of 11 free parameters is given in Table 3.4.

3.4.3 Fitting

We use Bayesian analysis techniques to estimate the best-fit set of model parameters from our data cube, including the SMBH mass. Specifically, we utilize a Markov chain Monte

Carlo (MCMC) method with Gibbs sampling to explore the parameter space. The number of iterations is set to 10^6, and the first 5×10^4 iterations are ignored as a burn-in phase. The method will be fully described in Davis et al. (2016), but we provide a short summary here. The aim is to obtain the posterior distribution of the 11 model parameters: SMBH mass, stellar M/L, and the molecular gas disc kinematic centre, inclination, position angle, systemic velocity, velocity dispersion, integrated flux (CO surface brightness scaling factor), radial scalelength and void radius.

The region of the cube used for fitting covers the entire CO emitting region, and is defined to be $13''.0$ by $13''.0$, the centre coinciding with the core position observed by Liuzzo et al. (2009). Velocity channels are from -380 km s^{-1} to 380 km s^{-1} with respect to the systemic velocity of 2069 km s^{-1}.

We use a logarithmic likelihood function based on the χ^2 distribution, calculated by comparing the CO distribution in each channel of the data cube with that in the model. As our data are approximately Nyquist sampled spatially, the synthesised beam induces strong correlations between neighbouring pixels in the data cube. The likelihood function we use, $\exp(-\chi^2/2)$, takes this into account by including the full covariance matrix when calculating the χ^2. As the condition number of the covariance matrix itself is large, we do not invert it directly to calculate the likelihood, but instead introduce a modified Cholesky factorization step to avoid loss of numerical precision when calculating the inverse. The observational error on the flux in each pixel is set to the rms noise of the data cube evaluated in the central regions, in channels where no emission is detected.

We use flat priors for all the fitted parameters, within certain ranges. The prior distributions used and the posterior distributions returned are summarised in Table 3.4. The posterior distributions are also shown with greyscales in Figure 3.3. A comparison of the data and best-fit model moment 0 and moment 1 maps is shown in Figure 3.4. An

analogous comparison of the channel maps is shown in Figure 3.5.

3.4.4 Results

We take the best fit of each model parameter directly from our Bayesian analysis, as the parameter value with the smallest χ^2 in our multi-dimensional parameter space. For example, the SMBH mass is determined to be $5.75\times10^8\ M_\odot$, consistent with the predicted value from the known stellar velocity dispersion (216 km s^{-1}; Cappellari et al. 2013a) and the $M_{\rm BH}$–σ relation of McConnell & Ma (2013).

The error bars of each model parameter are computed as percentiles of the posterior. Specifically, the 1σ confidence limits are the 15.9$^{\rm th}$ and 84.1$^{\rm th}$ percentiles of the posterior, while the 3sigma limits are the 0.14$^{\rm th}$ and 99.87$^{\rm th}$ percentiles of the posterior (see the grey-shaded regions in the likelihood contours of Figure 3.3).

Using this procedure, the SMBH mass and stellar M/L are measured to be $5.75^{+1.49}_{-1.18}\times 10^8\ M_\odot$ and $1.45\pm0.04\ (M/L)_{\odot,H}$, respectively, at the 3σ confidence level. The reduced chi-square ($\chi^2_{\rm red}$) for the best fit is 0.75, indicating a good fit. The inclination angle is measured to be $69^\circ.90\pm0.61$ under the particular morphology of the molecular gas disc assumed. See Table 3.4 for the other best-fit parameters describing the molecular gas disc.

This SMBH mass gives an intrinsic SOI of $0''.3$, which is still half of the synthesized beam. This SOI radius is slightly smaller than the radius of a cavity in the best fit, $0''.38$. The SMBH mass is thus constrained to 23% at the 3σ level (7% at 1σ), although we do not detect Keplerian motion in the very centre. The error budget is comparable to that in the case of Barth et al. (2016b), who resolved the SOI ($0''.23$) of NGC 1332 using ALMA high angular resolution ($0''.044$ synthesized beam) observations. We further investigate our SMBH mass error budget in Section 3.5.3, focusing on possible systematic effects.

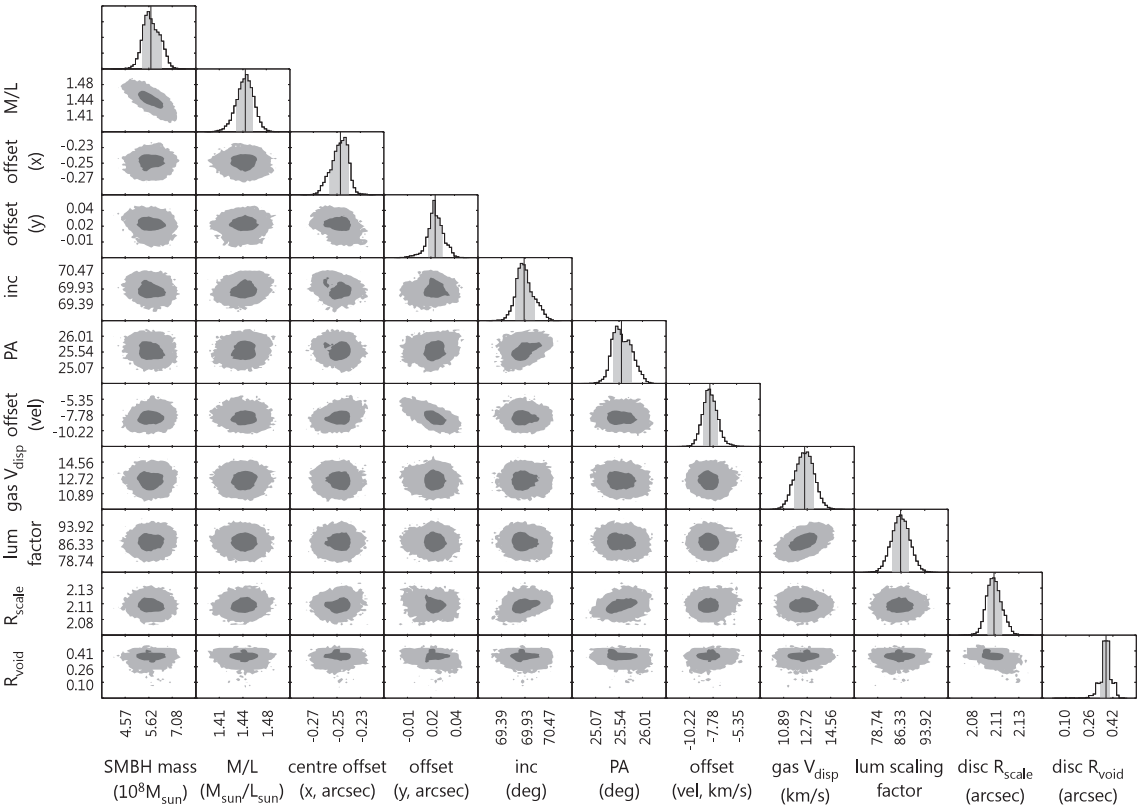

Figure 3.3: **NGC 3665 Posterior Histograms and Likelihood Contours:** Histograms showing the posterior distribution of each model parameter, with the 68.3% (1σ) confidence interval shaded in grey. Greyscales show the likelihood distribution of every pair of parameters. Regions of parameter space within the 3σ confidence level are coloured in pale grey while regions within 1σ are coloured in dark grey. Some pairs of parameters show a correlation (e.g. SMBH mass and M/L_H), but they are still tightly constrained. The vertical lines in the histograms show the best-fit value of each parameter. See Table 3.4 for a quantitative listing of the uncertainties.

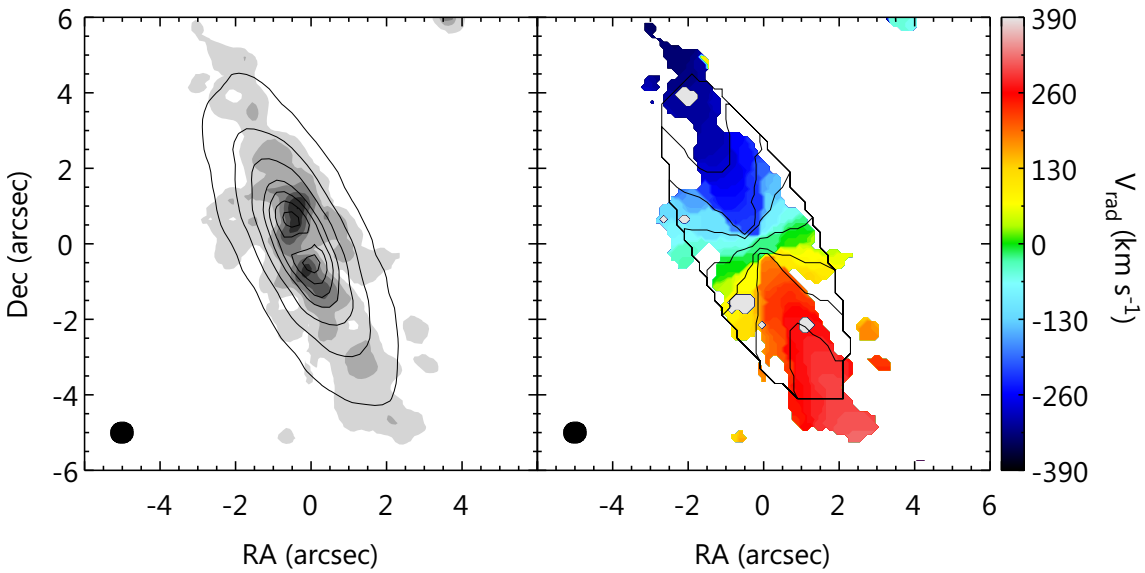

Figure 3.4: **NGC 3665 Observed and Best-Fit Model Moment 0 and 1 Maps:** *Left panel:* Integrated intensity (moment 0) map of the CARMA observations (greyscale), overlaid with that of the best-fit model (contours). Contours are set to be $1/12$, $2/12$, $3/12$, $5/12$, $7/12$, $9/12$ and $11/12$ of the peak. *Right panel:* Intensity-weighted (mean) velocity (moment 1) map of the the CARMA observations (colourscale), overlaid with that of the best-fit model (contours). Contours are spaced by 130 km s^{-1} from -390 to 390 km s^{-1}. The synthesised beam ($0''.60 \times 0''.56$ at a position angle of $-81°$) is shown in the bottom-left corner of each panel.

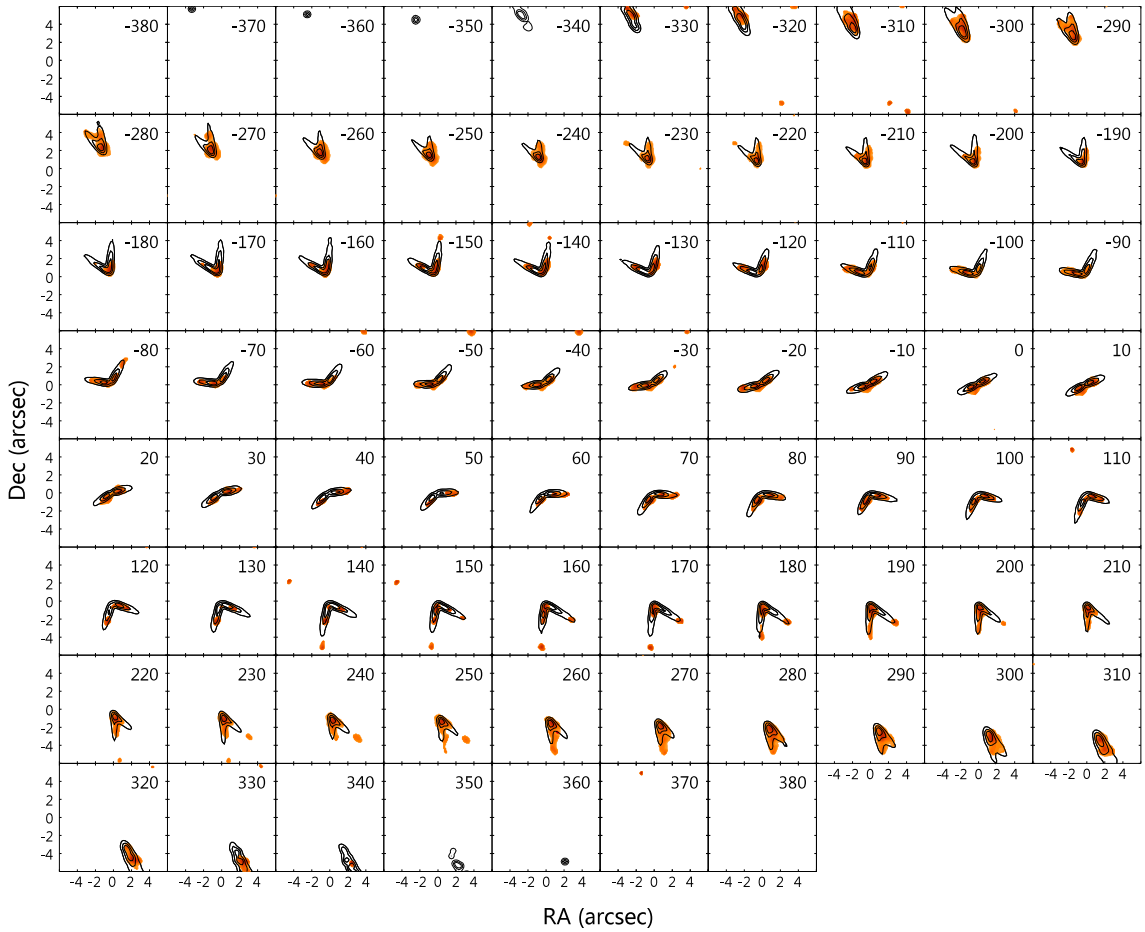

Figure 3.5: **Observed and Best-Fit Model Channel Maps:** Channel maps of the CARMA observations (colour scale), overlaid with those of the best-fit model (black contours). The velocity of each channel in km s^{-1} is indicated in the top-right corner of each panel. Contours of the observations are set to be $3/15$, $5/15$, $7/15$, $9/15$, $11/15$ and $13/15$ of the peak intensity observed in each channel. Models are plotted with contours set to be $3/15$, $7/15$ and $11/15$ of the peak intensity of the model in each channel.

3.5 Discussion

3.5.1 CO Morphology

As NGC 3665 harbours an AGN, the molecular gas could be affected by its presence and/or that of the SMBH itself. With the highest angular resolution achieved so far, our CO observations have revealed that the molecular gas disc in NGC 3665 has an unresolved central hole, the position of which coincides with that of the radio core (detected with VLBI observations; Liuzzo et al. 2009) and the peak of the stellar surface brightness (identified from *HST* observations).

The absence of molecular gas within a radius of $\approx 0''.4$ or ≈ 65 pc suggests that some mechanism may be dissociating the molecular gas or preventing it from forming or accumulating in the very centre of the galaxy. The dissociation of molecules generally has two main causes, AGN activity and UV radiation from young stars. While the former is clearly a possibility, the latter is unlikely to be significant in NGC 3665 as the star formation density is low (Davis et al., 2014). Dynamical effects can also affect the distribution and survival of molecular gas. Shocks and resonances are obvious possibilities, but it may also be that the strong shear expected near the SMBH (where the circular velocity curve varies with the radius R as $R^{-1/2}$) can destroy molecular clouds, where most molecules are generally found. Such dynamical mechanisms will be analysed further in future works. Evidently, the lack of molecular gas in the central hole also suggests that there is no current cold gas accretion in that region. Having said that, observations targeting different molecules and/or transitions are necessary to prove that the central hole is truly devoid of gas, and to explore possible mechanisms for void creation.

3.5.2 AGN Properties

As mentioned above, given NGC 3665's stellar velocity dispersion (Cappellari et al., 2013a), the best-fit SMBH mass is in agreement with the latest $M_{\rm BH}$–σ relations (e.g. McConnell & Ma, 2013). However, we can also investigate whether this SMBH mass is consistent with the known properties of the AGN. A radio jet was detected early on in NGC 3665 (Parma et al., 1986; Nyland et al., 2016), with the jet axis almost exactly perpendicular to the major axis of the central molecular gas disc. While AGN jets are generally thought to emerge perpendicularly to their accretion discs, it is also commonly accepted that there need not be a connection with the orientation of the large-scale disc of the galaxy. While the latter is the case for low-luminosity AGN such as Seyferts in late-type galaxies, the jet and large-scale molecular gas disc in NGC 3665 clearly have a connection. The kinematic position angle of the molecular gas disc is determined to be 26°, roughly perpendicular to the position angle of the jet, 137° (determined by drawing a line from the northeast to the southwest blob seen at 5 GHz by Nyland et al. 2016).

The X-ray luminosity of NGC 3665 ($L_{\rm X}$) was estimated to be $10^{40.1}$ erg s^{-1} in the 2–10 keV energy range, extrapolated from the total energy within the *Chandra* energy range of 0.3–8 keV by assuming a power-law spectrum $N(E) = \alpha\, E^{1.7}$ and a value of α derived from the same observations (Liu, 2011). Comparing this X-ray luminosity to the Eddington luminosity calculated from our best-fit SMBH mass ($L_{\rm Edd} = 1.27 \times 10^{38}\, M_{\rm BH}$ erg s^{-1} $M_\odot^{-1} = 10^{46.8}$ erg s^{-1}), we obtain an Eddington ratio of $\log(L_{\rm X}/L_{\rm Edd}) = -6.73$. This relatively low Eddington ratio suggests radiatively inefficient flows, including powerful outflows such as the radio jet observed in NGC 3665 (Merloni et al. 2003 and references therein). We therefore conclude that the AGN properties of NGC 3665 do not conflict with the derived SMBH mass nor with the observed molecular gas kinematics.

3.5.3 Other Error Sources for the SMBH Mass

Several high angular resolution observations of kinematics, aiming to measure SMBH masses, show Keplerian upturns in galaxy centres (see, e.g., Miyoshi et al., 1995; Barth et al., 2016b). Keplerian motion is expected in a potential dominated by a SMBH, where observations resolve the SMBH SOI and some emission arises from within the SOI. Spatially resolving the Keplerian region naturally allows to constrain the SMBH mass to high accuracy, as only a point mass yields such a behaviour, but our data do not show clear Keplerian motion. A possible reason for this is that CO emission is not present in the SMBH's vicinity, as our model reveals a central cavity of radius $0''.38$ (see Section 3.4.4). Even if that were not the case, the synthesized beam ($0''.60 \times 0''.56$; see Section 3.3) could have smeared out the information from within the SOI ($0''.3$; see Section 3.4.4).

Nevertheless, we measure a SMBH mass with an uncertainty of only 23% (at 3σ confidence). The stellar M/L and inclination, that have a direct influence on the SMBH mass, also have small uncertainties. Here we therefore investigate possible systematic errors on these parameters, and then discuss other possible effects that could increase the error budget.

A potential reason for the small error on the stellar M/L is the rather large fitting area, set to $13''.00$ by $13''.00$ so as to include all CO emission. A large fraction of this area is dominated by the stars rather than the SMBH. The uncertainty on the stellar M/L (and in turn the SMBH mass and inclination) may thus decrease as the number of constraints (i.e. the area) increases, irrespective of whether the fit is good or not, simply because the model looses its freedom to vary (χ^2 would otherwise increase unacceptably). We therefore narrow down the fitting area to $4''.00$ by $4''.00$, and repeat the fit described in Section 3.4. The SMBH mass is then measured to be $M_{\rm BH} = (5.37^{+1.24}_{-1.10}) \times 10^8\ M_\odot$ and the stellar $M/L = 1.49 \pm 0.05\ (M/L)_{\odot,H}$, with an inclination angle $i = 69^\circ.64 \pm 0.77$, all at 3σ

confidence level. This best-fit parameter set yields $\chi^2_{\rm red} = 1.20$. Surprisingly, with fewer data, the constraints on the SMBH mass (19% error), M/L (3% error) and inclination (1% error, all at 3σ confidence) are just as tight as the original result. Comparing these results with the ones from the original fit ($M_{\rm BH} = 5.75^{+1.49}_{-1.18} \times 10^8\ M_\odot$, $(M/L)_H = 1.45 \pm 0.04\ (M/L)_{\odot,H}$ and $i = 69\overset{\circ}{.}90 \pm 0.61$, all at 3σ; see Section 3.4.4), we nevertheless notice a possible systematic error on the stellar M/L, but not on the SMBH mass or inclination.

The systematic error of the stellar M/L could come from the MGE model (stellar luminosity profile), that has no associated errors. The stellar luminosity profile becomes degenerate with the stellar M/L when calculating the circular velocity, and thus clearly affects the uncertainty on the stellar M/L. Our MGE model also fluctuates depending on, for example, how we define the region of dust attenuation (see Section 3.4.1 and Figure 3.2 for the MGE model fitting). We thus use two more MGE models with different definitions of the region affected by dust, and fit to an area of $13''.0 \times 13''.0$. We first create a mask to cover the right half of the *HST* image, divided with a line as shown in the left-hand panel of Figure 3.6. The unmasked region within a $6''.0$ radius is used to create the new MGE. The resulting SMBH mass is $M_{\rm BH} = 5.4 \times 10^8\ M_\odot$ with $(M/L)_H = 1.41\ (M/L)_{\odot,H}$, yielding $\chi^2_{\rm red} = 0.73$. Second, we mask all the pixels with negative values in an unsharp-masked version of the *HST* image, created using a Gaussian of FWHM $0''.2$. The mask and the unsharp-masked image are shown in the right-hand panel of Figure 3.6. By using the MGE fit created from the unmasked pixels, the SMBH mass and stellar M/L are measured to be $M_{\rm BH} = 5.50 \times 10^8\ M_\odot$ and $(M/L)_H = 1.24\ (M/L)_{\odot,H}$, yielding again $\chi^2_{\rm red} = 0.73$. The best-fit values of the stellar M/L are however beyond the statistical 3σ error in both cases.

Total stellar luminosity also has some error, which is not considered in our MGE

model. Wider range of stellar M/L is expected if we allow our MGE model to vary 8 Gaussians altogether. The variation will require at least 16 more parameters to search, assuming the same central position for all the Gaussians. Given the fitting procedure will be too expensive with additional parameters for the variable MGE model, here we include the total luminosity error for the HST observation so to estimate a more realistic error of the stellar M/L.

Our tests thus indicate that systematic uncertainties on the SMBH mass are $\approx 0.4 \times 10^8\ M_\odot$, likely of the order of the quoted statistical 3σ errors. The systematic uncertainties on the stellar M/L are estimated to be $\approx 0.2\ (M/L)_{\odot,H}$, larger than the quoted statistical 3σ errors. Here we do not explicitly consider the effects of potential spatial variations of the stellar M/L onto the SMBH mass error budget. This could however lead to non-negligible uncertainties, and we plan to test for this in a future work. The uncertainties on the stellar M/L and SMBH mass would also increase by considering e.g., galaxy distance and *HST* photometric zero point uncertainties.

We further comment that the χ^2 in our fit is calculated by considering only the rms noise level in the cube as the observational error. Including other sources of error would possibly increase the error on the fitting parameters.

3.5.4 Rotation Curve Fit

CARMA and ALMA observations just recently revealed that molecular gas kinematics enables SMBH mass measurements in nearby galaxies (e.g. NGC 4526, Davis et al. 2013; NGC 1097, Onishi et al. 2015; NGC 1332, Barth et al. 2016a). However, when comparing to models, the first two studies used only a rotation curve extracted from a position-velocity diagram (PVD) taken along the galaxy major axis. The procedure can be briefly summarised: (1) determine the kinematic major axis and draw a PVD along

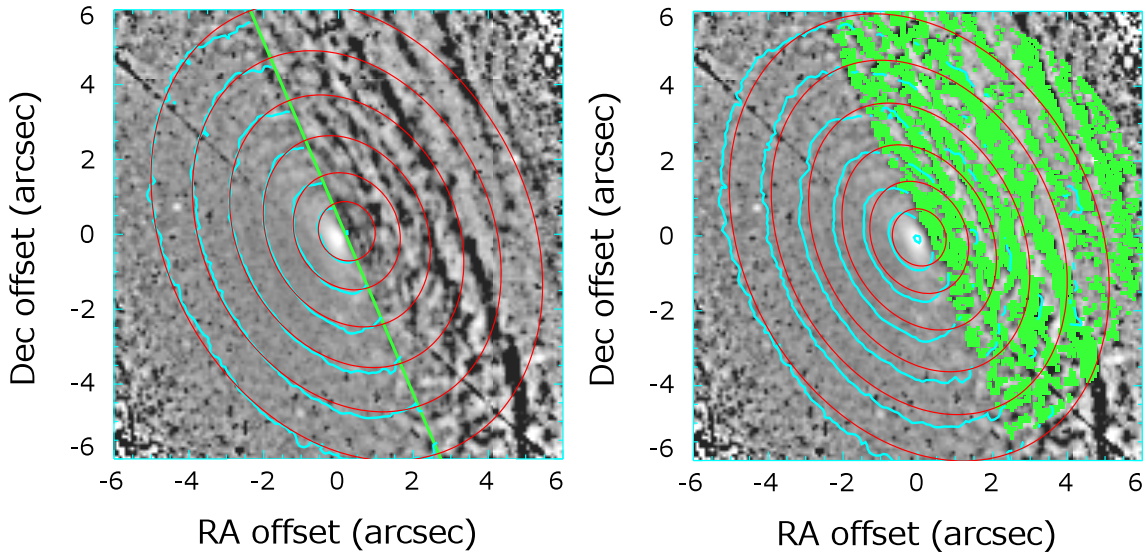

Figure 3.6: **NGC 3665 *HST* H-band Image and Alternative MGE Models:** *Left:* Alternative MGE model (red contours) created by using data only on the left side of the green line. The contours are overlaid on an unsharp-masked *HST* H-band (NICMOS F160W) image (blue contours and grey scale). *Right:* Another MGE model (red contours) created by masking all the pixels indicated in green, overlaid to the unsharp-masked *HST* H-band (NICMOS F160W) image (blue contours and grey scale).

it; (2) estimate the mean velocity at each position along the PVD to determine the rotation curve; (3) compare these velocity measurements with analogous ones made from a model rotation curve extracted from a model data cube (assuming a set of model parameters) in an identical manner; (4) identify the best-fit model parameters using a χ^2 analysis throughout parameter space.

In this sub-section, we thus re-derive the SMBH mass of NGC 3665 by fitting only the rotation curve extracted from our data, to verify that the value derived is in agreement with the full data cube fit of the previous sections. First, we fixed all molecular gas disc parameters to those obtained from the full data cube fit (see Table 3.4), leaving only the SMBH mass and stellar M/L as free model parameters. We then extracted the kinematic major-axis PVD from our data cube, and fit Gaussians to the line-of-sight velocity distribution at each position to determine the mean velocity at that position, only keeping for

the model fit measurements with a signal-to-noise ratio $S/N > 3$. The uncertainty at each position was set to the root mean square of the channel width of the observation and the FWHM of the fitted Gaussian. If the Gaussian FWHM was too large, generally indicating a bad fit, we also excluded that position from the model fit. A total of 55 mean velocity measurements were thus made along the extracted PVD, creating an observed rotation curve along the kinematic major-axis of NGC 3665.

Model data cubes were generated for a range of SMBH mass and M/L values, and model rotation curves extracted in the same manner as for the data. These were then compared to the data in a χ^2 manner, and polynomial fits to the χ^2 distribution of each model parameter (with the other parameter fixed at its best-fit value) are shown in Figure 3.7. The uncertainties on each parameter were estimated from the 99.7% confidence interval (i.e. the parameter values with $\chi^2 \leq \chi^2_{\rm min} + 9$). The best-fit SMBH mass and stellar M/L are then $(5.6 \pm 1.0) \times 10^8\ M_\odot$ and $1.48 \pm 0.02\ (M/L)_{\odot,H}$, respectively, with a $\chi^2_{\rm min}$ of 112.7 and the reduced χ^2 of 2.21 (the number of degrees of freedom here is 53, allowing for the two free parameters). We note that the minimum $\chi^2_{\rm red}$ is slightly above unity, suggesting the existence of a better fit with other molecular gas disc parameters.

A comparison of the observed and best-fit model PVD and their rotation curves are also shown in Figure 3.8. The two parameters for each panel are $M_{\rm BH} = 0$ with a best-fit $M/L = 1.48\ (M/L)_{\odot,H}$ (left panel; $\chi^2_{\rm red} = 9.12$), the best-fit $M_{\rm BH} = 5.6 \times 10^8\ M_\odot$ and $M/L = 1.48\ (M/L)_{\odot,H}$ (middle panel; $\chi^2_{\rm red} = 2.21$) and an overweight SMBH with $M_{\rm BH} = 2.8 \times 10^9\ M_\odot$ and $M/L = 1.25\ (M/L)_{\odot,H}$ (right panel; $\chi^2_{\rm red} = 24.65$).

The SMBH mass and stellar M/L derived from the rotation curve fit are both consistent with those obtained from the full data cube fit, despite the very small uncertainties on the M/L ratios. In fact, the uncertainties derived are also very similar. The two fitting methods therefore appear equally useful a priori. This is probably because the Rotation

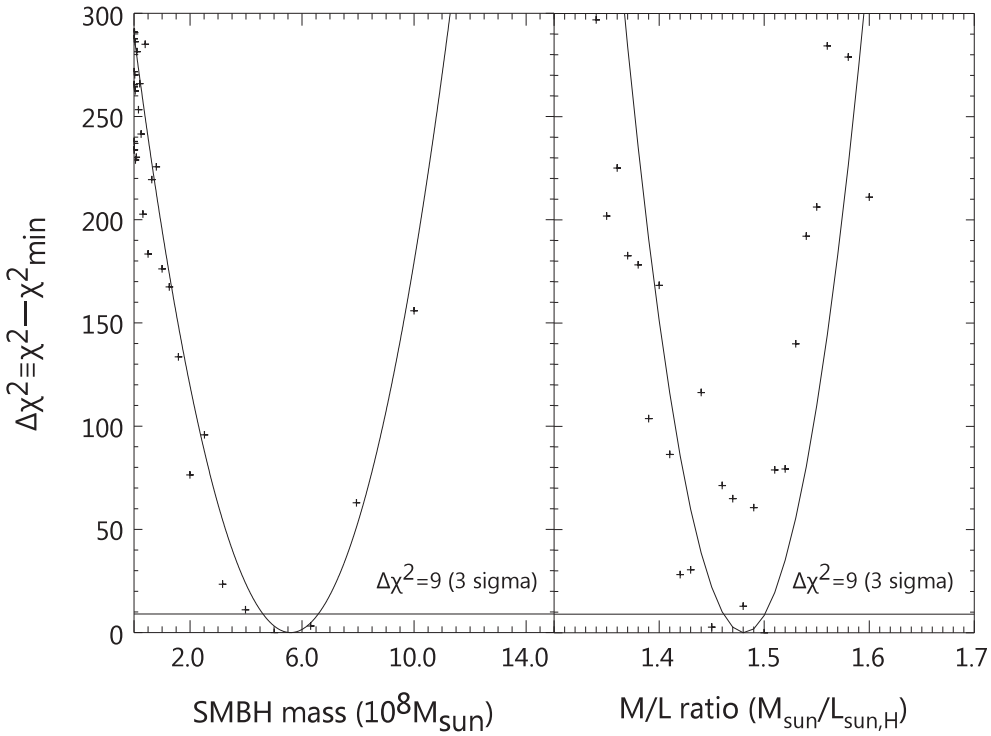

Figure 3.7: **NGC 3665 PVD Fit Uncertainties:** Distributions of the unreduced $\Delta\chi^2 \equiv \chi^2 - \chi^2_{\rm min}$ for the PVD fit model parameters, SMBH mass (left) and stellar M/L (right). Data points show the actual $\Delta\chi^2$ while solid lines are the polynomial fits. The uncertainty of each parameter (3σ confidence level) is determined by the intersection of the polynomial fits with the straight horizontal line ($\Delta\chi^2 = 9$). The best-fit model parameters are then $M_{\rm BH} = 5.6^{+1.0}_{-1.0} \times 10^8\ M_\odot$ and $M/L = 1.48 \pm 0.02\ (M/L)_{\odot,H}$.

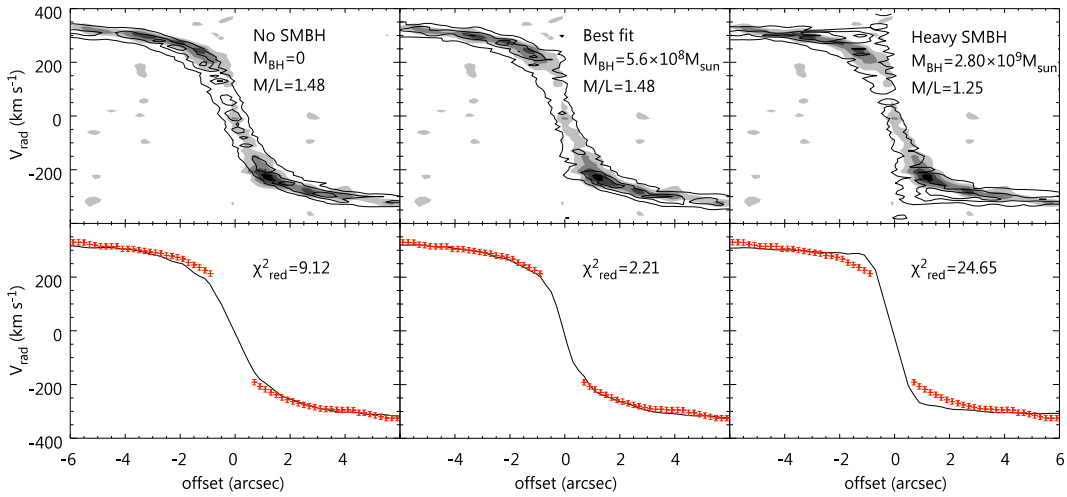

Figure 3.8: **Comparison of PVDs from Model and Observation, Both of NGC 3665:** *Upper panels:* Observed position-velocity diagram (PVD) along the kinematic major axis (greyscale), overlaid with the model PVDs (contours). The left panel shows a comparison with a model without a black hole ($M_{\rm BH} = 0$), the middle panel with the best fit, and the right panel with an overweight black hole. *Lower panels:* Extracted mean velocities along the kinematic major axis (red points with error bars), overlaid with the best-fit model velocities (black lines). The $\chi^2_{\rm red}$ of each model is 9.12 (left, $M_{\rm BH} = 0$), 2.21 (middle, best fit) and 24.65 (right, overweight SMBH).

curve fit extracts the crucial part of the data cube, most closely related to the mass of the SMBH and stellar body. However, we recall that the rotation curve fit has only 2 free parameters, compared to 11 for the data cube fit. The other parameters, taken from the data cube fit, were fixed during the rotation curve fit. The data cube thus contains a lot of information useful to constrain many other model parameters associated with the structure of the molecular gas disc itself (see Section 3.4). In addition, a major disadvantage of the rotation curve fit is that some parameters can be degenerate with the SMBH mass or stellar M/L and therefore must be independently constrained (e.g. the disc inclination, that directly affect the M/L and to a lesser extent the SMBH mass). Extracting the appropriate PVD also requires a well-defined kinematic major axis, that is difficult to specify when the velocity field shows warps and/or kinematic twists. A middle ground is to fit an extracted velocity field. For example, Neumayer et al. (2007) considered warped and misaligned ellipses to model the ionised gas velocity field of NGC 5128 (Centaurus A). In NGC 3665, however, there is no significant evidence for non-circular motions. Models with warped structures may nevertheless be required in the future, as highly detailed gas distributions gradually become available through higher angular resolution observations.

3.6 Conclusions

We presented CARMA ^{12}CO$(J = 2-1)$ observations of the early-type galaxy NGC 3665 with $0''.59$ resolution. These reveal a regularly rotating molecular gas disc in the equatorial plane of the galaxy, with an apparent void within a radius of $\approx 0''.4$ or ≈ 65 pc, potentially created by the known AGN.

Fitting the entire observed data cube of NGC 3665 with a model with free SMBH mass, stellar M/L, and numerous parameters describing the structure of the molecular gas disc, we derive a SMBH mass of $M_{\rm BH} = 5.75^{+1.49}_{-1.18} \times 10^8\ M_\odot$ and a stellar M/L

of $(M/L)_H = 1.45 \pm 0.04\ (M/L)_{\odot,H}$ at 3σ confidence levels (statistical error). This SMBH mass is in agreement with that estimated from the latest $M_{\rm BH} - \sigma$ correlations, and appears consistent with the known AGN properties of NGC 3665, such as its radio jet and X-ray luminosity. Systematic uncertainties on the stellar M/L are estimated to be $\approx 0.2\ (M/L)_{\odot,H}$, by considering smaller fitting regions and several different MGE models. We estimate the systematic uncertainties on the SMBH mass to be $\approx 0.4 \times 10^8\ M_\odot$, which is within the statistical 3σ error. The full data cube fit also yields a SMBH mass consistent with that derived from a fit to the rotation curve only, but it opens the door to SMBH mass measurements in sources with significantly more complex molecular gas discs.

This work is only the fourth SMBH mass measurement using molecular gas kinematics, following measurements in two other lenticular galaxies and one barred spiral (Davis et al., 2013; Onishi et al., 2015; Barth et al., 2016a). This method has thus proven its usefulness to derive SMBH masses in various types of galaxies. It offers exciting prospects to both calibrate SMBH masses measured with other methods, and simply increase the number of galaxies with reliable SMBH masses. Further investigations comparing SMBH masses measured using other methods (stellar kinematics, ionised-gas kinematics and/or megamasers) will be required before a proper discussion of potential systematic differences between the methods is possible.

Chapter 4

SMBH mass measurement in NGC 5064

4.1 Abstract of this Chapter

I here present a measurement of the supermassive black hole (SMBH) mass in a nearby spiral galaxy NGC 5064. The galaxy is observed with Atacama Large Millimetre/submillimetre Array (ALMA) with $\sim 0''.14$ angular resolution, which corresponds to ~ 30pc. We use ^{12}CO $(J = 2 - 1)$ emission line to trace the circular motion of molecular gas. Three-dimensional molecular gas kinematics is analysed and modelled to obtain the SMBH mass of $M_{\rm BH} = 1.61^{+1.06}_{-0.64} \times 10^8 M_{\rm odot}$, and the H-band stellar $M/L = 0.390 \pm 0.005$ ($M/L_{\odot,H}$). Other parameters are also determined to describe the geometry of the molecular gas disc (statistical errors, all at 3σ confidence). The result follows the $M_{\rm BH} - \sigma$ relation with a known $\sigma = 192$ km s^{-1}.

4.2 Introduction

We have developed and improved our SMBH mass measuring method (see Chapter 2 and 3), aiming to expand the target and thus enable to shed more light into the coevolutionary

process of galaxy and black hole. The targets (NGC 1097 and NGC 3665) were observed at a ~ 100 pc resolution at each object, and the SMBH sphere of influence (SOI; $R_{\rm SOI} \equiv GM_{\rm BH}/\sigma^2$, where G is the gravitational constant) was not resolved.

Although these two examples showcase the ability of the method of being applicable for various galaxies, measuring SMBH masses without resolving the SOI is somewhat unreliable. For example in the case of NGC 3665 (Chapter 3), our model suggested existence of a central cavity of molecular gas, with the radius larger than the SOI of the best-fit SMBH mass. This implies that we miss information inside the SOI when observing the CO$(J = 2 - 1)$ emission line. This can simply be solved by observing other molecular species, or by trying to observe other galaxies without a cavity to firstly determine if the Keplarian upturn within the SOI is really necessary for the SMBH mass accuracy.

We here observe a nearby spiral galaxy NGC 5064 at a $0''.14 \sim 28$ pc resolution. This is slightly larger or comparable to the SOI of the SMBH mass $1.6 \times 10^8 M_\odot$, estimated by a known stellar velocity dispersion (192 km s^{-1}, HyperLEDA database) and the $M_{\rm BH} - \sigma$ relation (McConnell & Ma, 2013). Aiming to detect the Keplarian motion, we reduce the data as described in Section 4.3. We report a simple analysis of the stellar mass estimation and a SMBH mass measurement by repeating the method described in Section 3.4. The SMBH mass measuring method is briefly summarized in Section 4.4. We discuss on future prospects of the method in Section 4.5 and summarize the conclusions in Section 4.6.

4.2.1 The target – NGC 5064

NGC 5064 is a nearby spiral galaxy (SA) at a distance of 43.3 Mpc (determined as a median of distance measurements in the past, Mathewson et al., 1992; Willick et al., 1997; Tully et al., 2013; Sorce et al., 2014). The source is located at $R.A. = 13 : 18 : 59.9$,

$Dec = -47:54:31.15$ (J2000.0) and known to be quiescent. There is no evidence of nuclear activity observed for this galaxy, and no dynamical mass measurements have been reported for the SMBH. The known stellar velocity dispersion (192 km s^{-1}, HyperLEDA database) and the $M_{\rm BH} - \sigma$ relation (McConnell & Ma, 2013) gives an estimate of the SMBH mass of $1.6 \times 10^8 M_\odot$, yielding the SOI radius of $\sim$ 20pc, thus $\sim 0''.1$ at the assumed distance.

4.3 Observations and Data Reduction

NGC 5064 was observed with the band 6 receiver on ALMA (Project code=2015.1.00466.S; PI: K. Onishi). The observations were carried out on 20th and 26th November, 2015, and on 5th and 27th March, 2016. The total on-source integration time of 29 minutes was acquired at the hour angle of ~ -4h and ~ -1h in November and in March, respectively. The array consisted of 43 and 42 12 m antennas in November 20 and 26, respectively, to cover the baseline length of 82 – 11053 m, and this yielded a maximum recoverable scale of $2''.0$. 38 and 41 12 m antennas were used in March 5 and 27, respectively. The baseline length was 15 – 460 m, and the maximum recoverable scale was $10''.8$. A synthesized beam realized by these configurations was $0''.05 \times 0''.04$ at a position angle of $-62^\circ.22$. This corresponds to $\sim 10 \times 8$ pc at the object. The receivers were tuned to cover the frequency range from 242.568 to 246.556 GHz (upper side band, 256 channels) and from 227.314 to 231.186 GHz (lower side band, 3840 channels till 229.189 GHz and then 128 channels for the rest). CO $(J = 2 - 1)$ emission line is detected in the upper side band from 228.51 to 227.98 GHz with a channel separation of 0.488 MHz. Calibrators used in these observations are J1427-4206 (bandpass and phase calibrator), J1307-5019 (phase calibrator) and J1107-4449 (flux calibrator).

The data were reduced and imaged by using CASA (Common Astronomy Software

Applications) Version 4.6.0. We first image the data by using the whole (u, v) components to yield a full spatial resolution. The CLEAN task in CASA with a robustness parameter of 0.5 provided the beam size of $0''.05 \times 0''.04$ ($\sim 10 \times 8$ pc) at a position angle of $-62°.22$. We binned the spectrum by 3 channels to gain the velocity width of 15.0 km s^{-1}. The rms noise was 0.31 mJy beam^{-1} for the data cube, and the signal to noise ratio was not enough to image the CO distribution (see left panels of Figure 4.1). We thus clipped the data cube at 2.7 sigma level and integrated from -280 to 280 km s^{-1}, relative to the systemic velocity of 2980 km s^{-1} to obtain the moment 0 map presented at the top left of Figure 4.1. The peak was then detected at 4.5 sigma level for the rms noise of 36.7 mJy beam^{-1} km s^{-1} (calculated from the emission-free pixels of the unclipped data), but clearly, most of the emission is below the rms noise level. Velocity map (middle left of Figure 4.1) is also created for this image with a threshold of $1/10$ of the moment 0 peak of 165 mJy beam^{-1} km s^{-1}. Kinematic major axis is then determined from the velocity map to create a Position-Velocity Diagram (PVD) along the axis, as shown in the lower left of Figure 4.1. The SMBH SOI is estimated to be ~ 20 pc $\sim 0''.1$ and is resolved in this case. Detection of Keplerian motion is thus expected, but we only see a slight kink at the centre and it is too dim due to the low signal-to-noise ratio.

We then cut out the outer (u, v) components to increase the signal-to-noise ratio, by using the UVTAPER option in CLEAN. Applying the taper with FWHM of 1000 kilo-lambda (thus ~ 1314 m) we obtained the synthesized beam of $0''.15 \times 0''.12$ at a position angle of $-66°.75$ ($\sim 30 \times 24$ pc). Binning the data by 3 channels, we gain the velocity width of 15.0 km s^{-1} and the rms noise of 0.36 (mJy beam^{-1}) per channel. We again clipped the data cube at 2.7 sigma level and integrated from -280 to 280 km s^{-1} to create a moment 0 map (top right of Figure 4.1). The peak was detected at 5.8 sigma level for the rms noise of 37.7 (mJy beam^{-1} km s^{-1}; calculated from the unclipped data). Velocity map (middle right of Figure 4.1) is also created for this image with a threshold of $1/10$ of

the moment 0 peak of 219 mJy beam^{-1} km s^{-1}. PVD (lower right of Figure 4.1) does not show clear enough Keplerian motion at this resolution, and suggests a velocity dispersion ($v_{\rm disp,gas}$) distribution for this molecular gas disc. We consider this is due to the beam size ($\sim 0''.14$) that does not resolve the SOI ($\sim 0''.1$). Moment 2 map (Figure 4.2) is created for this image with a threshold of $1/10$ of the moment 0 peak.

4.4 Method

4.4.1 The Mass Model

Stellar mass distribution of NGC 5064 is estimated from *HST* observations. We take an image obtained with the NICMOS F160W filter to model the stellar luminosity distribution by using the Multi Gaussian Expansion method (MGE, Cappellari et al., 2002). We use the central $8'' \times 8''$ of the *HST* image and first unsharp-mask the image using a Gaussian of FWHM $0''.2$. We then mask all the pixels with negative values in the unsharp-masked image (indicated in green in Figure 4.3), and use all the unmasked pixels to fit the luminosity distribution with multiple Gaussians using the MGE method.

The MGE model is summarized in Figure 4.3 and in Table 4.1. A spatially uniform stellar M/L is considered and multiplied to the modelled luminosity profile (stellar mass), and then a delta function is added at the centre (SMBH mass).

4.4.2 Velocity Model Calculation and the Result

(1) Case 1 – a thin disc

A circular motion is calculated by using the mass model described as above. Instrumental effects such as beam-smearing and spatial and velocity binning are all taken into account

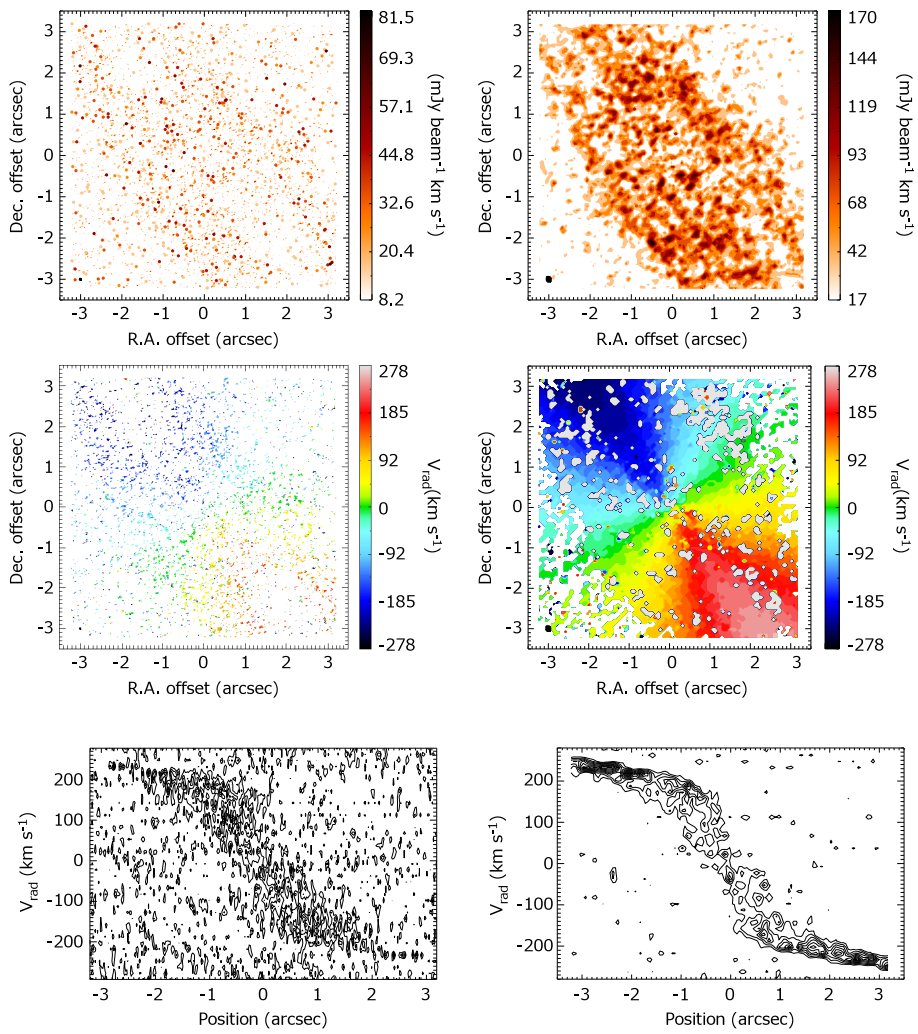

Figure 4.1: **NGC 5064 mom0, mom1 and PVD:** *L*eft: CO(2-1) image reduced by using the whole (u, v) components. The beam size is $0''.05 \times 0''.04$, shown at the lower left of the intensity distribution map (upper panel) and velocity map (middle panel). Moment 0 map is integrated from -280 to 280 km s^{-1} with respect to the systemic velocity of 2980 km s^{-1}. The rms noise for the unclipped moment 0 map is 36.7 (mJy beam^{-1} km s^{-1}). The moment 0 peak is 165 (mJy beam^{-1} km s^{-1}), thus ~ 4.5 sigma. Obviously most of the flux are resolved out. A position-velocity diagram along the galaxy major axis at its position angle of $35°$ is shown in the bottom. *R*ight:We cut out the components outer than 1000 kilolambda in the (u, v) plane to obtain $0''.15 \times 0''.12$ beam (lower left of the upper and middle panels). The moment 0 map (upper panel) yields a rms noise of 37.7 (mJy beam^{-1} km s^{-1}) with the peak of 219 (mJy beam^{-1} km s^{-1}), thus ~ 5.8 sigma. Middle is the velocity map and bottom is the PVD along the same axis as in the left.

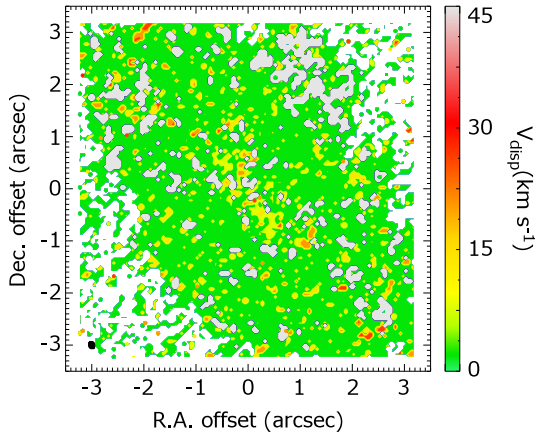

Figure 4.2: **NGC 5064 mom2:** Moment 2 map of NGC 5064 observed with $0''.15 \times 0''.12$ beam.

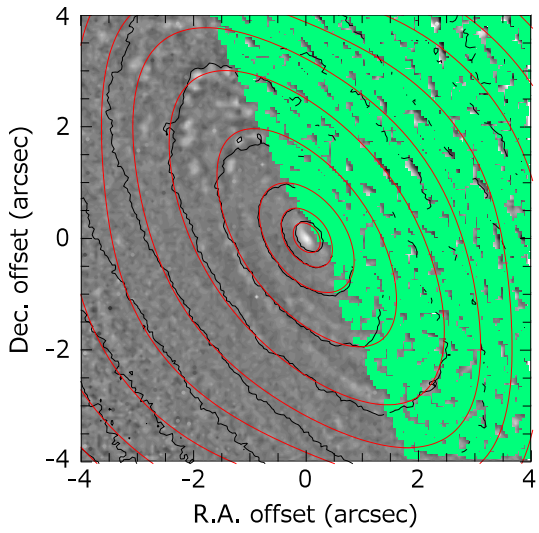

Figure 4.3: **NGC 5064 MGE model:** *HST* NICMOS F160W (H-band) image (unsharp-masked), overlaid with the MGE model (red contours). The MGE parameters are summarized in Table 4.1. Pixels coloured in green are considered to be dust attenuated region, and are not included to the MGE fitting.

Table 4.1: NGC 5064 MGE components of the *HST* NICMOS F160W image

j	I_j	σ_j	q_j
	($L_{\odot,V}$ pc^{-2})	(arcsec)	
1.....	75064.6	0.037	0.779
2.....	45582.7	0.237	1.000
3.....	60558.8	0.468	0.559
4.....	40106.7	0.978	0.648
5.....	25741.6	4.296	0.400
6.....	15237.5	4.296	0.974

by KinMS (Davis et al., 2013). We consider a spatial fitting area to be $6''.45 \times 6''.45 \sim 1300 \times 1300$ pc, with the velocity width of 585 km s^{-1}, thus 129×129 pixels $\times 39$ channels. χ^2 is calculated by using the rms per channel (0.36 mJy beam^{-1}) to compare the model and the observed data. We set 10 free parameters for the fitting process: SMBH mass, stellar M/L, and the molecular gas disc kinematic centre, inclination, position angle, systemic velocity, $v_{\rm disp,gas}$, integrated flux (CO surface brightness scaling factor) and radial scalelength. A thin disc with a spatially uniform $v_{\rm disp,gas}$ is considered in this calculation.

By repeating the process described in Section 3.4, we search the parameter space with the iteration number of 10^5 times. The first 5000 iterations were ignored as a burn-in period. The best-fit parameter set including $M_{\rm BH} = 2.63 \times 10^8\ M_\odot$ and $M/L = 0.385\ (M/L_{\odot,H})$, however, does not give a good enough model to trace what we observed. Comparison of the best-fit and the observation (Figure 4.4), particularly in a form of PVD (Figure 4.5) suggests a spatially variable $v_{\rm disp,gas}$. The SMBH mass is not too far from the one estimated by a known stellar velocity dispersion ($\sigma = 192$ km s^{-1}, HyperLEDA

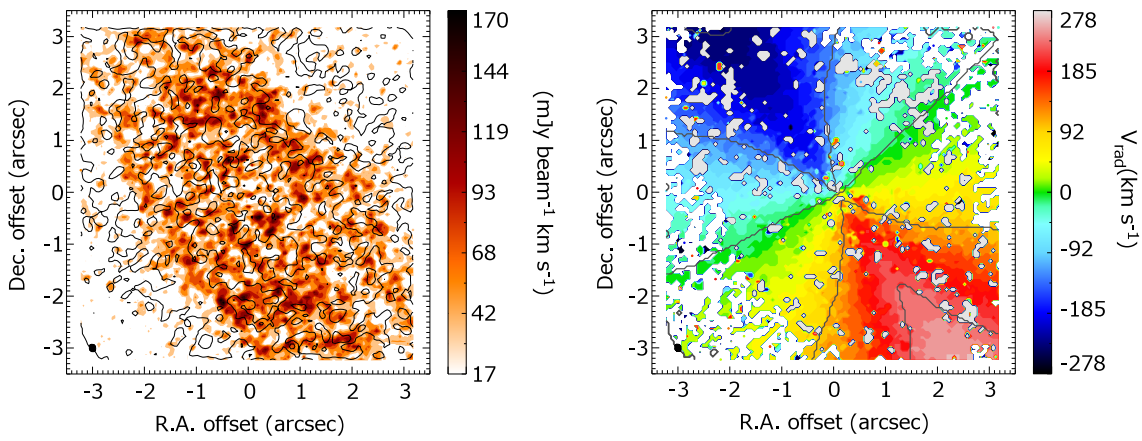

Figure 4.4: **Comparison of NGC 5064 Observation and a the best fit Model (thin disc assumption):** The best-fit model (black contours) compared with observations (colour contours) in forms of integrated intensity map (left panel) and velocity map (right panel). The model here is calculated with the mass parameters of $M_{\rm BH} = 2.63 \times 10^8 M_\odot$ and $M/L = 0.385$.

database) and the $M_{\rm BH} - \sigma$ relation (McConnell & Ma, 2013), $M_{\rm BH} = 1.6 \times 10^8 M_\odot$. The minimum reduced chi-square $\chi^2_{\rm red,min}$ realized by the best fit is 1.47, slightly above unity. In addition to the comparison of model and observation in PVD (Figure 4.5), the moment 2 map (Figure 4.2) also suggests a distribution of $v_{\rm disp,gas}$, while it is hard to model the radial dependence from the map due to its low signal to noise ratio.

(2) Case 2 – a thick disc

Spatial variation of the $v_{\rm disp,gas}$ can be explained in two ways – one is to consider a dynamically perturbed disc, and another is to consider a thick (but dynamically cold) disc. A clear rotational motion as seen in Figure 4.1 indicates a gas disc without turbulence. We thus consider the gas disc to be the latter (a dynamically cold thick disc), and add disc thickness to the free parameters.

Eleven free parameters are searched during this fitting process: SMBH mass, stellar M/L, and the molecular gas disc kinematic centre, inclination, position angle, systemic

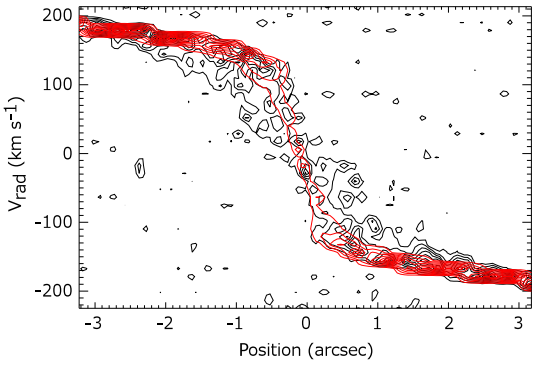

Figure 4.5: **Comparison of NGC 5064 Observation and Model (thin disc assumption) in PVD:** The PVD is taken along the kinematic major axis (Position Angle$= 34°$). Black contours are the observation and red are the best-fit model with $M_{\rm BH} = 2.63 \times 10^8 M_\odot$ and $M/L = 0.385$. The $v_{\rm disp,gas}$ seem to have a distribution, and becomes higher at central $0''.1 - 1''.0$.

velocity, $v_{\rm disp,gas}$, integrated flux (CO surface brightness scaling factor), radial scalelength, and disc thickness. By using the mass model described in Section 4.4.1, velocity model is calculated and compared with the observation by calculating the χ^2 from the rms noise level per channel (0.36 mJy beam^{-1}). Both Figure 4.6 and Table 4.2 show the posterior distributions after 10^5 times iteration of MCMC. Again the first 5×10^3 iterations are ignored here as a burn-in phase. The best-fit parameter set this time includes $M_{\rm BH} = 1.61 \times 10^8 M_\odot$ and the stellar $M/L = 0.390\ M/L_{\odot,H}$, and yields the $\chi^2_{\rm red,min} = 1.38$. The SMBH mass is consistent with the known stellar velocity dispersion ($\sigma = 192$ km s^{-1}, HyperLEDA database) and the $M_{\rm BH} - \sigma$ relation (McConnell & Ma, 2013). Comparison in forms of moment 0 and moment 1 map (Figure 4.7) traces what we observed, and more importantly, PVD (Figure 4.8) shows a better coincidence with the observation. We thus conclude that a thick disc model can provide a better model compared to the thin disc model (as in Section 4.4.1), but a spatial distribution of $v_{\rm disp,gas}$ may need to be considered in addition to the disc thickness.

Table 4.2: Model parameters (thick disc)

Parameter	Search range	Best fit	Error (68% conf.)	Error (99.7% conf.)
SMBH mass ($10^8 M_\odot$)	0.001–31.622	1.61	$+0.37, -0.30$	$+1.06, -0.64$
Stellar M/L ($M/L_{\odot,H}$)	0.100–2.000	0.390	± 0.001	± 0.005
Molecular gas disc:				
Centre X offset (arcsec)	-3.50–3.50	0.11	± 0.00	± 0.01
Centre Y offset (arcsec)	-3.50–3.50	-0.01	± 0.00	± 0.00
Inclination (°)	67.00–80.00	70.77	± 0.03	± 0.10
Position angle (°)	0–50	35	± 0	± 0
Centre velocity offset (km s^{-1})	-50.00–50.00	0.04	± 0.16	± 0.31
Luminosity scaling	50.00–200.00	78.55	± 0.99	± 2.82
Scale length (arcsec)	3.00–9.00	4.27	± 0.00	± 0.02
Disc thickness (arcsec)	0.00–3.00	0.32	± 0.00	± 0.01

Notes: The prior distribution of each parameter, shown in the second column, is assumed to be uniform in linear space (logarithmic for the SMBH mass only). Error budgets estimated from a posterior distribution of each parameter is quantified in the third to fifth columns (but see also Fig. 4.6).

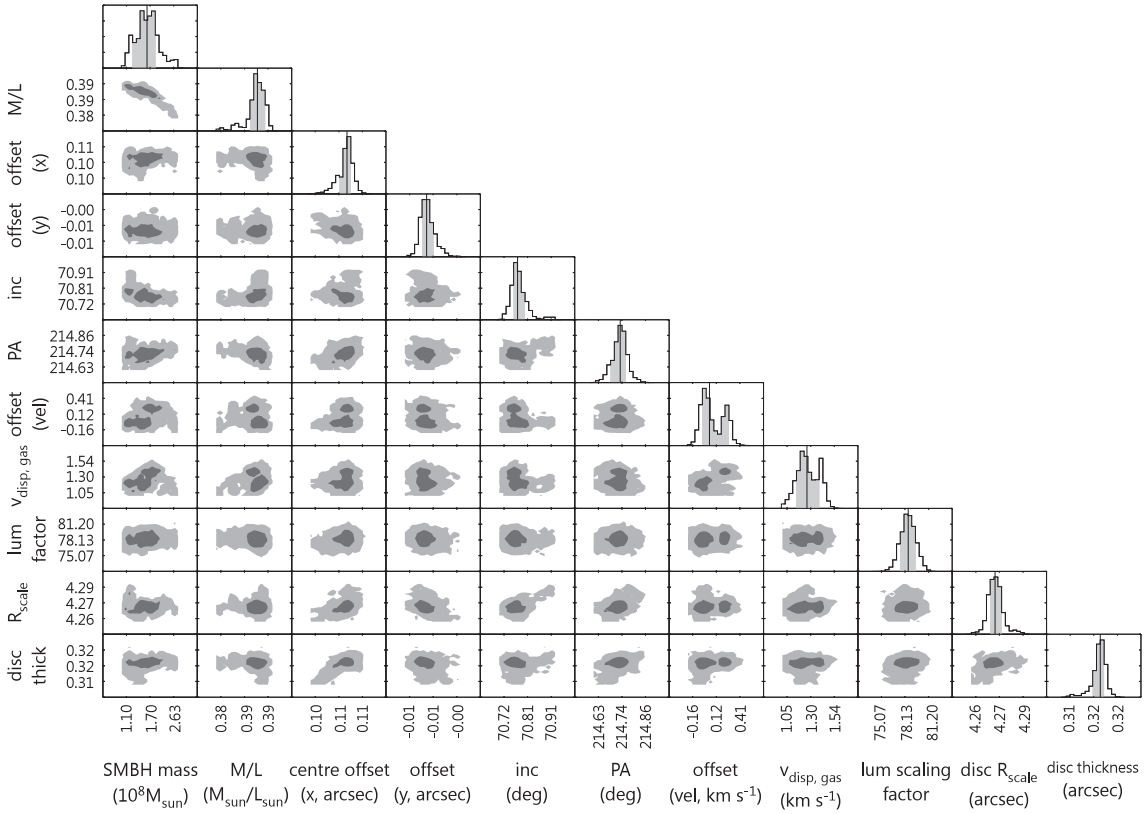

Figure 4.6: **NGC 5064 likelihood distribution (thick disc):** Histograms showing the likelihood distribution of each model parameter, with the 99.7% (3σ) confidence interval shaded in grey. Greyscales show the likelihood distribution of every pair of parameters. Regions of parameter space within the 3σ confidence level are coloured in pale grey while regions within 1σ are coloured in dark grey. The exact values are given in Table 4.2.

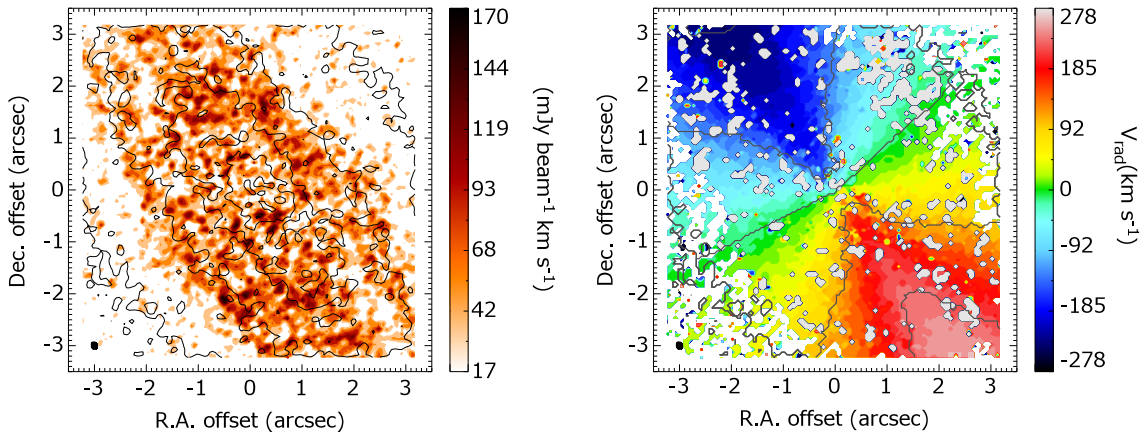

Figure 4.7: **Comparison of NGC 5064 Observation and Model (thick disc):** A best-fit model (black contours) compared with observations (colour contours) in forms of integrated intensity map (left panel) and velocity map (right panel). The model here is calculated with a set of best-fit parameters as summarized in Table 4.2. The mass parameters are given to be $M_{\rm BH} = 1.61 \times 10^8 M_\odot$ and $M/L = 0.390$.

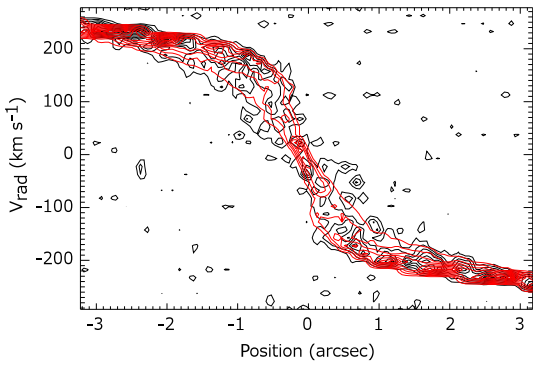

Figure 4.8: **Comparison of NGC 5064 Observation and Model (thick disc) in PVD:** The PVD is taken along the kinematic major axis (Position Angle= $35°$). Black contours are the observation and red are the best-fit model with $M_{\rm BH} = 1.61 \times 10^8 M_\odot$ and $M/L = 0.390$. The $v_{\rm disp,gas}$ seem to be traced with the thick disc model (red), but some dim velocity components are not traced even with the thick disc.

4.5 Discussion – Velocity Dispersion of the Gas Disc

Distributions of $v_{\rm disp,gas}$ were normally not considered in previous works, but Barth et al. (2016a) examined three distributions of $v_{\rm disp,gas}$ for their target with its inclination angle of $\sim 80^\circ$. Edge-on systems has a large $v_{\rm disp,gas}$, as more information is condensed in each pixel when observed. In their case, an assumption of uniform $v_{\rm disp,gas}$ constrained the SMBH mass but other distributions of $v_{\rm disp,gas}$ covered the rotational motion and only provided lower limits of SMBH mass. They concluded that the uniform $v_{\rm disp,gas}$ model was justified by observing at a higher angular resolution in Barth et al. (2016b). In our case of NGC 5064, the inclination angle is $\sim 70^\circ$ but the moment 2 map and PVD suggests a spatial distribution of $v_{\rm disp,gas}$. While we successfully traced the velocity width seen in the PVD (Figure 4.8) by considering a disc thickness, there are some dim velocity components still remaining behind. We thus do not reject the possibility of local perturbation, which can be reflecting an effect from the spiral arm structure or physical properties of each giant molecular cloud residing in the disc. The disc thickness can have a radial dependence, which is not considered in our model this time. This work proves that the thick disc model provides a realistic $v_{\rm disp,gas}$ distribution as observed. Although there are some velocity components that are not traced with the model, we consider them to be very dim (around 1 sigma at each channel) to affect the χ^2 and the result, and thus will not give further discussion.

4.6 Conclusion

The SMBH mass in a nearby spiral galaxy NGC 5064 is measured to be $M_{\rm BH} = 1.61^{+1.06}_{-0.64} \times 10^8 M_{\rm odot}$, with the stellar $M/L = 0.390 \pm 0.005$ ($M/L_{\odot,H}$). The galaxy was observed to achieve a $0''.05 \sim 10$ pc resolution, but the outer (u, v) components were cut out

with a Gaussian (FWHM=1000 kilolambda) to increase the signal-to-noise. The data thus yielded $0''.14 \sim 30$ pc resolution with a moment 0 peak of ~ 5.8 sigma. The SMBH SOI is $\sim 0''.1$ thus 20 pc, and we see a slight kink of the Keplerian component in the $0''.05$ resolution PVD. We do not detect clear enough Keplerian feature with the resolution of $0''.14$.

We first assume a dynamically cold thin disc model and measure the SMBH mass to be $M_{\rm BH} = 2.63 \times 10^8\ M_\odot$ and the stellar $M/L = 0.385\ M/L_{\odot,H}$. Suggested by the comparison of model and the data in a form of PVD, we consider a thick disc model to give a spatial distribution for $v_{\rm disp,gas}$. The resulted model with a disc thickness realized a better PVD than the thin disc model, and the $\chi^2_{\rm red,min}$ slightly decreased from 1.47 (thin disc model) to 1.38 (thick disc model). Although there are some velocity components left behind, we consider them to be very dim and do not affect very much to the result. Spatial distribution of $v_{\rm disp,gas}$ reflecting a dynamical perturbation of molecular gas may provide a better model to trace those weak components.

This study clearly indicates that the disc thickness needs to be considered in the case of NGC 5064. The reason for this thickness is unknown, but a thick molecular gas disc may be common for spiral galaxies. Late-type galaxies will be our main target in the future to balance the current bias in the sample of $M_{\rm BH} - \sigma$ relation (see Section 1.1.4), and the model of a thick (and perturbed) gas disc can be useful for many studies in the near future. A realistic distribution of $v_{\rm disp,gas}$ with the disc thickness will enable to measure more SMBH masses in spiral galaxies, and will eventually lead to the discussion of different $M_{\rm BH} - \sigma$ relations seen for early- and late-type galaxies.

Chapter 5

General Discussion – $M_{\rm BH} - \sigma$ Relation and Future Prospects

We developed and improved our SMBH mass measuring method so far (see Chapter 2, 3 and 4), aiming to expand the target and thus enable to shed more light into the coevolutionary process of galaxy and black hole. In this chapter, we update the $M_{\rm BH} - \sigma$ relation and discuss on future prospects.

Dynamical measurements of SMBH masses using molecular gas dynamics so far have been done for 5 galaxies. We here update the $M_{\rm BH} - \sigma$ relation as in Figure 5.1 by combining the data from McConnell & Ma (2013) (Figure 1.3) and a couple of other works using the molecular gas dynamics method which were not included at the time of its publication. SMBH masses measured with the molecular gas method are plotted in magenta (early-type) and cyan (late-type) squares. Additional plots seem to follow the known $M_{\rm BH} - \sigma$ relation. Two different relations between late-type and early-type were originally suggested by McConnell & Ma (2013) as plotted in red and blue in Figure 5.1, and the newly added results seem to follow the trend. We do not further comment on the difference between types, as the sample is still not decisive.

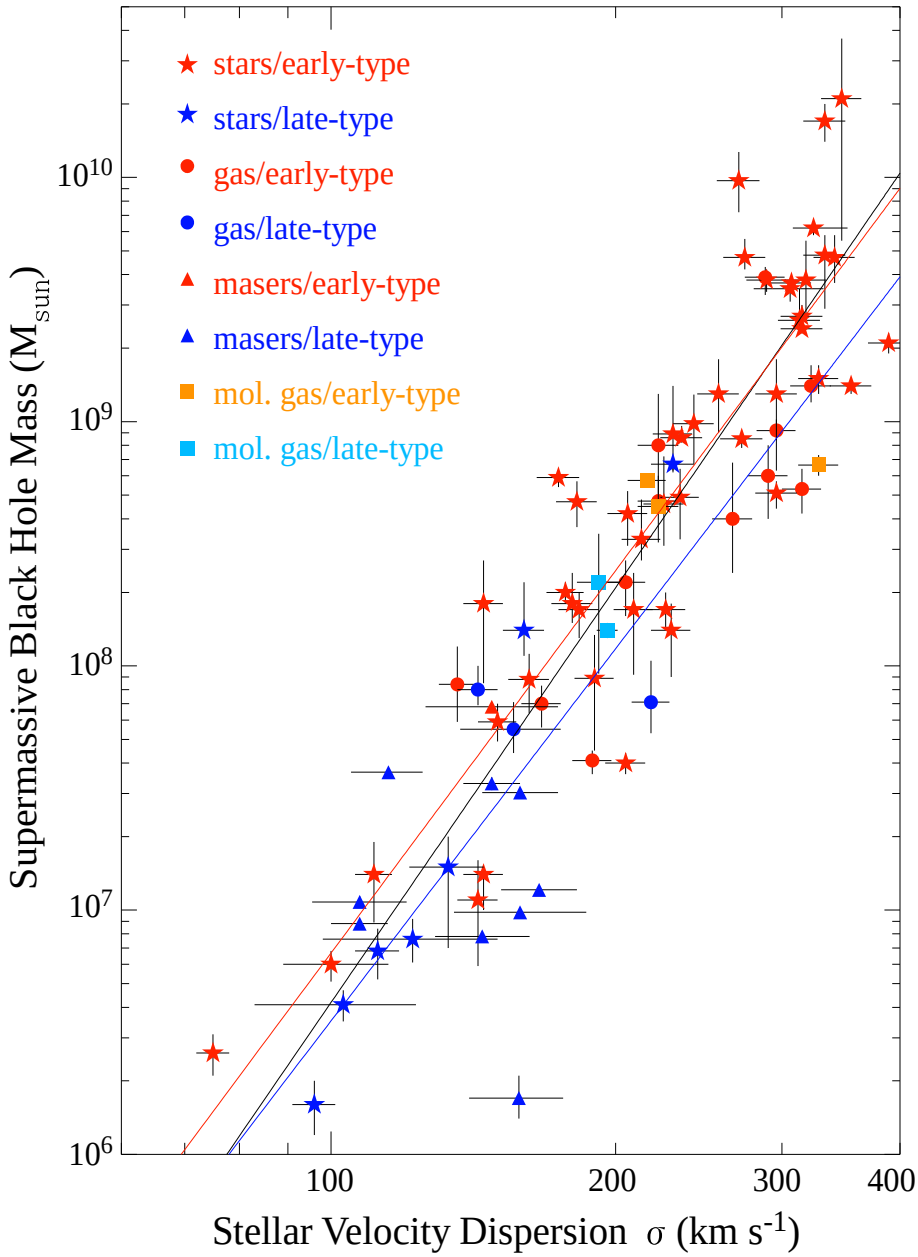

Figure 5.1: $M_{\rm BH} - \sigma$ **Relation (Updated):** The newest $M_{\rm BH} - \sigma$ plot, by using data summarized in McConnell & Ma (2013) (also shown in Figure 1.3) and other measurements using molecular gas method. Early-type galaxies are plotted in red and magenta. Late-type galaxies are plotted in blue and cyan. Symbols are used to identify the SMBH mass measuring method. SMBH masses measured with the molecular gas method (square symbols, orange and cyan) are consistent with the existing $M_{\rm BH} - \sigma$ relation. The black line ($\log_{10}(M_{\rm BH}/M_\odot) = 8.32 + 5.64 \log_{10}(\sigma/200 \text{ km s}^{-1})$) shows a fit to the entire sample. SMBH masses in each galaxy type from the molecular gas method (early-type plotted in orange, late-type in cyan) seem to follow the trend of different $M_{\rm BH} - \sigma$ relations for each type (early-type in red, $\log_{10}(M_{\rm BH}/M_\odot) = 8.39 + 5.20 \log_{10}(\sigma/200 \text{ km s}^{-1})$); late-type in blue, $\log_{10}(M_{\rm BH}/M_\odot) = 8.07 + 5.06 \log_{10}(\sigma/200 \text{ km s}^{-1})$).

The number of sample in the $M_{\rm BH} - \sigma$ relation thus becomes 83, which is still insufficient to discuss galaxy evolution. Despite the small number, the trend is clear and suggests an existence of coevolutionary process of galaxy and black hole. In order to further discuss on the evolutionary track on this $M_{\rm BH} - \sigma$ relation, we need to reduce uncertainties of measurements by investigating origins of some scatter seen in the relation. The scattered sample can be a reflection of different evolutionary stages, but it can also be caused by systematic errors among the dynamical methods. Comparison of a SMBH mass measured with multiple methods (cross checks; see also Section 1.2.7) suggests that the ionized gas method tends to derive a lower SMBH mass compared to the stellar dynamical method (see Figure 1.10). The number of cross checks are only 11, and the reason for this systematic departure is yet to be clarified. It has been hard to conduct this cross checks, as the dynamical methods do not have many targets in common (see Section 1.2 for details). We believe that the molecular gas method is capable of conducting cross checks at many SMBH masses measured with other dynamical methods. First, as shown in previous chapters, the method can be applied to various types of galaxies. Second, rotational motions of molecular gas are generally dynamically cold and less turbulent compared to ionized gas. Third, observations are normally short (100 minutes on-source in case of Barth et al., 2016b, with $0''.044$ beam using ALMA) compared to other methods. These advantages means that the method has a potential to acquire a larger sample of targets, and will dramatically increase the number of cross checks with all dynamical methods to measure SMBH mass. The cross checks will clarify the root cause of systematic error among the dynamical methods.

In case a significant systematic error is seen among the methods, one needs to avoid the systematic error and re-investigate the $M_{\rm BH} - \sigma$ relation by using a single dynamical method. In order to re-investigate the $M_{\rm BH} - \sigma$ relation, ~ 100 SMBH masses must be measured by the method, and the sample needs to be ubiquitous in evolutionary stage. We

believe the molecular gas method is the most efficient method that can provide sufficient amount of sample across the Hubble sequence, and it will be the best practice to discuss the coevolutionary process from the $M_{\rm BH} - \sigma$ relation (NB: there could be a sample bias by automatically selecting galaxies with molecular gas).

As a future work, I propose to measure SMBH masses by using dynamics of both molecular and ionized gas observed with integral field units, in order to clarify the systematic difference between ionized gas method and molecular gas method. The comparison will provide better precision to the SMBH masses measured with dynamical methods of both molecular and ionized gas. At the same time, I propose to investigate the systematic error by applying the molecular gas method to galaxies with their SMBH masses measured with other dynamical methods. These cross checks will clarify the origin of the scatter in the $M_{\rm BH} - \sigma$ relation, and will make up avenues for further research on the actual coevolutionary process of galaxy and black hole.

Evolutionary track on the $M_{\rm BH} - \sigma$ relation will be a further step to directly connect the empirical relation and the coevolution of galaxy and black hole. The coevolutionary process, particularly the black hole growth, is mainly discussed at unresolvable spatial resolution, in both theoretical and observational studies (summarized in, e.g., Alexander & Hickox, 2012). While these studies enable to estimate the exact amount of mass accretion to the SMBH, it is equally important to resolve feeding processes to the SMBH vicinity. The physical processes occur within the inner few hundred parsecs, and nearby galaxies are the only objects that allow us to spatially resolve the process. Gas transportation to the central few hundred parsecs have gradually become observable by using modern IFUs and interferometers (see, e.g., García-Burillo et al., 2003; Riffel et al., 2006; Combes et al., 2014; Smajić et al., 2015). Turbulent motions of gas are detected in several galaxies by modelling pure rotational motion and extracting the model from the

observed velocity field. The detected non-circular motions are then explained with inflow or outflow motions by modelling the galaxy morphology. Inflow and outflow rate can thus be estimated by assuming the inclination and gas density. It is clearly important to model a realistic rotational motion of gas in order to detect non-circular motions to good accuracy. Many of previous works, however, do not consider the mass distribution of the target and use observed rotation curve to model the circular motion. Aiming to obtain precise non-circular motions at the SMBH vicinity, I propose to observe gas motions at nearby galaxy centres at ~ 10 pc resolution, and to model a realistic circular motion by considering both stellar and SMBH mass, using the method described in Chapter 2, 3, and 4. Feeding rate to the SMBH vicinity gives us an idea of the SMBH growth rate, and opens possibility to constrain the mass accretion rate of SMBHs. I propose to expand this estimate in various galaxies scattered in the $M_{\rm BH} - \sigma$ relation. Inflow rates will then be compared among galaxies and will thus add another dimension to the relation. I believe that the results will connect the empirical relation and the evolutionary process of a black hole, by answering questions of the (co)evolutionary track on the $M_{\rm BH} - \sigma$ relation (e.g., Do low-mass black holes move upwards and then to the right? Do high-mass black holes have less food around them compared to the low-mass ones?).

Chapter 6

General Conclusion

We developed a new method to measure the supermassive black hole (SMBH) mass in nearby galaxies by using molecular gas kinematics observed with millimeter/submillimeter interferometers. The masses are measured to good accuracy ($\sim 20\%$ error), and follow the known empirical relation between SMBH mass and galaxy properties (e.g., $M_{\rm BH} - \sigma$ relation; correlation between SMBH mass and central stellar velocity dispersion of the host galaxy). Being considered as a key to resolve the co-evolutionary process of galaxy and black hole, the exact form of the $M_{\rm BH} - \sigma$ relation is still debated, mainly due to lack of sample. A large and various sample provided from our method (demonstrated in Chapter 2, 3 and 4) will allow detailed studies of the $M_{\rm BH} - \sigma$ relation.

In Chapter 2 we demonstrated the capability of ALMA for deriving accurate SMBH mass in late-type barred-spiral galaxy NGC 1097. We examined the precision of the result and proved that the method is applicable to both early-type and late-type galaxies. The SMBH mass was derived by using two different molecular species to assure the use of not only CO emission but HCN and HCO^+. These achievements proved the importance of the method itself, and leaded to a number of observations and publications (e.g., Barth et al., 2016a,b; Onishi et al., 2016; Davis et al. , 2016).

We then further generalized the molecular gas method in Chapter 3 by allowing more parameters (including ones to describe molecular gas disc properties) to vary and by developing a fitting method that uses a whole data cube. The new fitting method is originally developed in our work and tested by using both the data cube fitting and the PVD fitting. We demonstrated the method to be applicable to a fast-rotator with a radio jet, and proved the usefulness of this method to increase the number of sample.

We then applied the method for a nearby galaxy NGC 5064, as described in Chapter 4. This quiescent spiral galaxy shows a velocity dispersion distribution of the gas disc, and requires the gas disc model to be thick, instead of assuming to be thin as in previous works. ~ 10 pc resolution observations detected a slight evidence of Keplerian rotation, but the signal to noise was not enough to fully argue the Keplerian kink.

The $M_{\rm BH} - \sigma$ relation is updated in Chapter 5. SMBH masses measured by the molecular gas dynamics method does not conflict with the known $M_{\rm BH} - \sigma$ relation (McConnell & Ma, 2013). Cross checks between two different methods are of great importance to further clarify the $M_{\rm BH} - \sigma$ relation. Gas inflow or outflow motions are also very important to directly discuss on the SMBH growth and galaxy evolution, and thus an evolutionary track on the $M_{\rm BH} - \sigma$ plot.

These works have demonstrated the capability of the method to expand the number of dynamically-measured SMBH masses, across a much broader range of galaxies than ever before, and with little selection biases. As a future work, a better accuracy on the result with less assumptions is required. I propose to work on increasing the number of SMBH mass measurements and to cross check some of the results with other dynamical methods, so to investigate the systematic error and thus to connect the coevolutionary process and the $M_{\rm BH} - \sigma$ relation. I believe the results will eventually revolutionize our understanding on the co-evolution of galaxies and black holes.

Acknowledgment

I am greatly indebted to a main supervisor of my thesis, Professor S. Iguchi, who provided constant support, expertise, and enthusiasm throughout my Ph.D. programme at Department of Astronomical Science, SOKENDAI (The Graduate University for Advanced Studies).

I thank Dr. D. Iono for giving me constructive advices and suggestions on proposals and presentations, and on my research career. I thank Dr. Y. Matsuda for always encouraging me with positive comments. I thank Dr. S. Komugi for discussions and help throughout my Ph. D. programme. I thank Prof. N. Arimoto for being the greatest mentor of my life and giving me useful advices since I entered SOKENDAI (The Graduate University for Advanced Studies).

The research reported here would not have been possible without the support of many people in the National Astronomical Observatory of Japan (NAOJ) in Mitaka, Tokyo, Japan, Joint ALMA Observatory in Vitacura, Santiago, Chile, National Radio Astronomy Observatory (NRAO) in Charlottesville, VA, USA, the Univesity of Tokyo, Mitaka, Japan, and University of Oxford, Oxford, UK. I thank Prof. K. Kohno and Dr. K. Sheth for giving me both scientific suggestions and productive advices in my Ph. D. life. I thank Dr. H. Nagai and Dr. K. Nakanishi for helping me with data reduction. I thank Prof. M. Bureau for allowing me to visit University of Oxford, for the invaluable experience and for the productive discussions. I am grateful to Dr. T. A. Davis, Dr. M. Cappellari, Dr. M. Sarzi

and Prof. L. Blitz for all the help, discussions and advices for our research. In addition, I would like to thank all staffs in NAOJ Chile Observatory, especially Ms. N. Saito for kindly helping me with a lot of paperwork. I would also like to thank the graduate education support office at Mitaka.

This thesis would have not been completed without the support of referees, Prof. S. Kameno, Dr. M. Imanishi, Prof. K. Ebisawa, Dr. Y. Koyama, and Dr. Y. Tamura. I would like to thank them all for giving me constructive comments and taking their time to discuss on the details with me.

Outside the work, I would like to thank all the students in the Chile Observatory at NAOJ, especially Y. Aso, S. Ohashi, and T. Saito for being always cheerful and supportive. I would like to thank Dr. P. Sanhueza, Dr. N. Izumi, Dr. K. Kiyokane, C. Hara, Dr. K. Fujii, Dr. A. Matsuzawa, Kapibara-san, Y. Kato, M. Lee, T. Michiyama, T. Kurahashi, M. Ando, I. Kurose and A. Silva for their support.

I thank Dr. Y. Hamada for understanding my choices all the time, and constantly encouraging me to work on my research. I am grateful to my family for unconditional support throughout my life so far.

The research makes use of the following ALMA data: ADS/JAO.ALMA#2011.0.00108.S, #2015.1.00466.S. ALMA is a partnership of ESO, NSF (USA), and NINS (Japan), together with NRC (Canada) and NSC and ASIAA (Taiwan), in cooperation with the Republic of Chile. The Joint ALMA Observatory is operated by ESO, AUI/NRAO, and NAOJ. The NRAO is a facility of the National Science Foundation operated under cooperative agreement by Associated Universities, Inc. This work is also based on observations made with the NASA/ESA *HST*, obtained from the Data Archive at the Space Telescope Science Institute, which is operated by the Association of Universities for Research in Astronomy, Inc., under NASA contract NAS 5-26555. Support for CARMA construction

was derived from the states of California, Illinois and Maryland, the James S. McDonnell Foundation, the Gordon and Betty Moore Foundation, the Kenneth T. and Eileen L. Norris Foundation, the University of Chicago, the Associates of the California Institute of Technology and the National Science Foundation. CARMA science was supported by the National Science Foundation under a cooperative agreement, and by the CARMA partner universities. This research made use of the NASA/IPAC Infrared Science Archive, which is operated by the Jet Propulsion Laboratory, California Institute of Technology, under contract with the National Aeronautics and Space Administration. I appreciate the usage of the HyperLeda database (http://leda.univ-lyon1.fr).

Data analysis were in part carried out on common use data analysis computer system at the Astronomy Data Center, ADC, of the National Astronomical Observatory of Japan. A part of this study was financially supported by JSPS KAKENHI Grant Number 26*368.

Bibliography

Abadi, M. G., Moore, B., & Bower, R. G. 1999, MNRAS, 308, 947

Alatalo, K., Davis, T. A., Bureau, M., et al. 2013, MNRAS, 432, 1796

Alexander, D. M., & Hickox, R. C. 2012, New A Rev., 56, 93

Arimoto, N., & Yoshii, Y. 1987, A&A, 173, 23

Barai, P., Viel, M., Borgani, S., et al. 2013, MNRAS, 430, 3213

Barth, A. J., Sarzi, M., Rix, H.-W., et al. 2001, ApJ, 555, 685

Barth, A. J., Darling, J., Baker, A. J., et al. 2016, ApJ, 823, 51

Barth, A. J., Boizelle, B. D., Darling, J., et al. 2016, ApJ, 822, L28

Baskin, A., & Laor, A. 2005, MNRAS, 356, 1029

Baugh, C. M. 2006, Reports on Progress in Physics, 69, 3101

Beifiori, A., Sarzi, M., Corsini, E. M., et al. 2009, ApJ, 692, 856

Beifiori, A., Courteau, S., Corsini, E. M., & Zhu, Y. 2012, MNRAS, 419, 2497

Bell, E. F., McIntosh, D. H., Katz, N., & Weinberg, M. D. 2003, ApJS, 149, 289

Blandford, R. D., & McKee, C. F. 1982, ApJ, 255, 419

Blanton, M. R., & Roweis, S. 2007, AJ, 133, 734

Blumenthal, G. R., Faber, S. M., Primack, J. R., & Rees, M. J. 1984, Nat, 311, 517

Bouwens, R. J., Illingworth, G. D., Oesch, P. A., et al. 2012a, ApJ, 754, 83

Bouwens, R. J., Illingworth, G. D., Oesch, P. A., et al. 2012b, ApJ, 752, L5

Bower, G. A., Wilson, A. S., Heckman, T. M., et al. 2000, Bulletin of the American Astronomical Society, 32, 92.03

Cappellari, M. 2002, MNRAS, 333, 400

Cappellari, M., Verolme, E. K., van der Marel, R. P., et al. 2002, ApJ, 578, 787

Cappellari, M. 2008, MNRAS, 390, 71

Cappellari, M., Neumayer, N., Reunanen, J., et al. 2009, MNRAS, 394, 660

Cappellari, M., Emsellem, E., Krajnović, D., et al. 2011, MNRAS, 413, 813

Cappellari, M., Scott, N., Alatalo, K., et al. 2013, MNRAS, 432, 1709

Cappellari, M., McDermid, R. M., Alatalo, K., et al. 2013, MNRAS, 432, 1862

Combes, F., García-Burillo, S., Casasola, V., et al. 2014, A&A, 565, A97

Cortés, J. R., Kenney, J. D. P., & Hardy, E. 2008, ApJ, 683, 78-93

Crawford, M. K., Genzel, R., Harris, A. I., et al. 1985, Nat, 315, 467

Croton, D. J., Stevens, A. R. H., Tonini, C., et al. 2016, ApJS, 222, 22

Crowl, H. H., Kenney, J. D. P., van Gorkom, J. H., & Vollmer, B. 2005, AJ, 130, 65

Cucciati, O., Tresse, L., Ilbert, O., et al. 2012, A&A, 539, A31

Dahlen, T., Mobasher, B., Dickinson, M., et al. 2007, ApJ, 654, 172

Dalla Bontà, E., Ferrarese, L., Corsini, E. M., et al. 2009, ApJ, 690, 537

Davies, R. I., Thomas, J., Genzel, R., et al. 2006, ApJ, 646, 754

Davis, T. A., Alatalo, K., Sarzi, M., et al. 2011, MNRAS, 417, 882

Davis, T. A., Bureau, M., Cappellari, M., Sarzi, M., & Blitz, L. 2013, Nat, 494, 328

Davis, T. A. 2014, MNRAS, 443, 911

Davis, T. A., Young, L. M., Crocker, A. F., et al. 2014, MNRAS, 444, 3427

Davis, T. A., Bureau, M., Onishi, K., et al. 2016, MNRAS, accepted

Davis, T. A., & McDermid, R. M. 2017, MNRAS, 464, 453

de Francesco, G., Capetti, A., & Marconi, A. 2006, A&A, 460, 439

de Francesco, G., Capetti, A., & Marconi, A. 2008, A&A, 479, 355

Denney, K. D., Peterson, B. M., Pogge, R. W., et al. 2010, ApJ, 721, 715

de Vaucouleurs, G., de Vaucouleurs, A., Corwin, H. G., Jr., et al. 1991, Third Reference Catalogue of Bright Galaxies. Volume II: Data for galaxies between 0^h and 12^h., by de Vaucouleurs, G.; de Vaucouleurs, A.; Corwin, H. G., Jr.; Buta, R. J.; Paturel, G.; Fouqué, P.. Springer, New York, NY (USA)

Devereux, N., Ford, H., Tsvetanov, Z., & Jacoby, G. 2003, AJ, 125, 1226

Di Matteo, T., Springel, V., & Hernquist, L. 2005, Nat, 433, 604

Di Matteo, T., Colberg, J., Springel, V., Hernquist, L., & Sijacki, D. 2008, ApJ, 676, 33-53

Diniz, M. R., Riffel, R. A., Storchi-Bergmann, T., & Winge, C. 2015, MNRAS, 453, 1727

Dressler, A., & Richstone, D. O. 1988, ApJ, 324, 701

Emsellem, E., Monnet, G., & Bacon, R. 1994, A&A, 285, 723

Emsellem, E., Cappellari, M., Krajnović, D., et al. 2011, MNRAS, 414, 888

Fabian, A. C. 2012, ARA&A, 50, 455

Fathi, K., Lundgren, A. A., Kohno, K., et al. 2013, ApJ, 770, L27

Ferrarese, L., Ford, H. C., & Jaffe, W. 1996, ApJ, 470, 444

Ferrarese, L., & Ford, H. 2005, SSRev, 116, 523

Ferrarese, L., & Merritt, D. 2000, ApJ, 539, L9

García-Burillo, S., Combes, F., Hunt, L. K., et al. 2003, A&A, 407, 485

Gebhardt, K., Richstone, D., Tremaine, S., et al. 2003, ApJ, 583, 92

Gebhardt, K., & Thomas, J. 2009, ApJ, 700, 1690

Gebhardt, K., Adams, J., Richstone, D., et al. 2011, ApJ, 729, 119

Genzel, R., Hollenbach, D., & Townes, C. H. 1994, Reports on Progress in Physics, 57, 417

Genzel, R., Thatte, N., Krabbe, A., Kroker, H., & Tacconi-Garman, L. E. 1996, ApJ, 472, 153

Genzel, R., & Eckart, A. 1999, The Central Parsecs of the Galaxy, 186, 3

Genzel, R., Pichon, C., Eckart, A., Gerhard, O. E., & Ott, T. 2000, MNRAS, 317, 348

Genzel, R., Eisenhauer, F., & Gillessen, S. 2010, Reviews of Modern Physics, 82, 3121

Ghez, A. M., Salim, S., Weinberg, N. N., et al. 2008, ApJ, 689, 1044-1062

Gillessen, S., Eisenhauer, F., Trippe, S., et al. 2009, ApJ, 692, 1075

Gooch, R. 1996, in ASP Conf. Ser. 101, Astronomical Data Analysis Software and Systems V, ed. G. H. Jacoby & J. Barnes (San Francisco, CA: ASP), 80

Gould, A. 2013, arXiv:1312.6692

Greene, J. E., & Ho, L. C. 2005, ApJ, 630, 122

Greene, J. E., Peng, C. Y., Kim, M., et al. 2010, ApJ, 721, 26

Gruppioni, C., Pozzi, F., Rodighiero, G., et al. 2013, MNRAS, 432, 23

Gültekin, K., Richstone, D. O., Gebhardt, K., et al. 2009, ApJ, 698, 198

Guo, Q., White, S., Boylan-Kolchin, M., et al. 2011, MNRAS, 413, 101

Heckman, T. M., & Best, P. N. 2014, ARA&A, 52, 589

Herrnstein, J. R., Moran, J. M., Greenhill, L. J., & Trotter, A. S. 2005, ApJ, 629, 719

Heß, S., & Springel, V. 2012, MNRAS, 426, 3112

Hicks, E. K. S., & Malkan, M. A. 2008, ApJS, 174, 31-73

Hopkins, A. M., & Beacom, J. F. 2006, ApJ, 651, 142

Hopkins, P. F., & Quataert, E. 2010, MNRAS, 407, 1529

Hopkins, P. F., Kereš, D., Murray, N., Quataert, E., & Hernquist, L. 2012, MNRAS, 427, 968

Hsieh, P.-Y., Matsushita, S., Liu, G., et al. 2011, ApJ, 736, 129

Hummel, E., van der Hulst, J. M., Keel, W. C., & Kennicutt, R. C., Jr. 1987, A&AS, 70, 517

Izumi, T., Kohno, K., Martín, S., et al. 2013, PASJ, 65, 100

Kaspi, S., Maoz, D., Netzer, H., et al. 2005, ApJ, 629, 61

Koribalski, B. S., Staveley-Smith, L., Kilborn, V. A., et al. 2004, AJ, 128, 16

Kormendy, J., & Ho, L. C. 2013, ARA&A, 51, 511

Kormendy, J., & Richstone, D. 1995, ARA&A, 33, 581

Krabbe, A., Genzel, R., Eckart, A., et al. 1995, ApJ, 447, L95

Krist, J. E., Hook, R. N., & Stoehr, F. 2011, Proc. SPIE, 8127, 81270J

Kuo, C. Y., Braatz, J. A., Condon, J. J., et al. 2011, ApJ, 727, 20

Läsker, R., Ferrarese, L., & van de Ven, G. 2014, ApJ, 780, 69

Lewis, K. T., & Eracleous, M. 2006, ApJ, 642, 711

Liu, J. 2011, ApJS, 192, 10

Liu, H. B., Hsieh, P.-Y., Ho, P. T. P., et al. 2012, ApJ, 756, 195

Liuzzo, E., Giovannini, G., Giroletti, M., & Taylor, G. B. 2009, A&A, 505, 509

Macchetto, F., Marconi, A., Axon, D. J., et al. 1997, ApJ, 489, 579

Madau, P., Ferguson, H. C., Dickinson, M. E., et al. 1996, MNRAS, 283, 1388

Madau, P., & Dickinson, M. 2014, ARA&A, 52, 415

Magnelli, B., Elbaz, D., Chary, R. R., et al. 2011, A&A, 528, A35

Magnelli, B., Popesso, P., Berta, S., et al. 2013, A&A, 553, A132

Magorrian, J., Tremaine, S., Richstone, D., et al. 1998, AJ, 115, 2285

Marconi, A., & Hunt, L. K. 2003, ApJ, 589, L21

Marziani, P., Sulentic, J. W., Plauchu-Frayn, I., & del Olmo, A. 2013, A&A, 555, A89

Mathewson, D. S., Ford, V. L., & Buchhorn, M. 1992, ApJS, 81, 413

McCarthy, I. G., Frenk, C. S., Font, A. S., et al. 2008, MNRAS, 383, 593

McConnell, N. J., Ma, C.-P., Gebhardt, K., et al. 2011, Nat, 480, 215

McConnell, N. J., & Ma, C.-P. 2013, ApJ, 764, 184

McConnell, N. J., Chen, S.-F. S., Ma, C.-P., et al. 2013, ApJ, 768, L21

McLure, R. J., & Jarvis, M. J. 2002, MNRAS, 337, 109

Mejía-Restrepo, J. E., Trakhtenbrot, B., Lira, P., Netzer, H., & Capellupo, D. M. 2016, MNRAS, 460, 187

Merloni, A., Heinz, S., & di Matteo, T. 2003, MNRAS, 345, 1057

Miyoshi, M., Moran, J., Herrnstein, J., et al. 1995, Nat, 373, 127

Muñoz-Mateos, J. C., Sheth, K., Regan, M., et al. 2015, ApJS, 219, 3

Navarro, J. F., Frenk, C. S., & White, S. D. M. 1997, ApJ, 490, 493

Netzer, H., & Peterson, B. M. 1997, Astronomical Time Series, 218, 85

Netzer, H., Lira, P., Trakhtenbrot, B., Shemmer, O., & Cury, I. 2007, ApJ, 671, 1256

Neumayer, N., Cappellari, M., Reunanen, J., et al. 2007, ApJ, 671, 132

Nyland, K., Young, L. M., Wrobel, J. M., et al. 2016, MNRAS, 458, 2221

Ondrechen, M. P., van der Hulst, J. M., & Hummel, E. 1989, ApJ, 342, 39

Onken, C. A., Valluri, M., Brown, J. S., et al. 2014, ApJ, 791, 37

Onishi, K., Iguchi, S., Sheth, K., & Kohno, K. 2015, ApJ, 806, 39

Onishi, K., Iguchi, S., Davis, T., Bureau, M., Cappellari, M., Sarzi, M., & Blitz, L. 2016, MNRAS, submitted

Park, D., Woo, J.-H., Denney, K. D., & Shin, J. 2013, ApJ, 770, 87

Parma, P., de Ruiter, H. R., Fanti, C., & Fanti, R. 1986, A&AS, 64, 135

Pastorini, G., Marconi, A., Capetti, A., et al. 2007, A&A, 469, 405

Peebles, P. J. E. 1982, ApJ, 263, L1

Peng, C. Y., Impey, C. D., Ho, L. C., Barton, E. J., & Rix, H.-W. 2006, ApJ, 640, 114

Peng, C. Y., Impey, C. D., Rix, H.-W., et al. 2006, ApJ, 649, 616

Peterson, B. M., & Wandel, A. 1999, ApJ, 521, L95

Reddy, N. A., & Steidel, C. C. 2009, ApJ, 692, 778

Rieke, G. H., & Rieke, M. J. 1988, ApJ, 330, L33

Riffel, R. A., Storchi-Bergmann, T., Winge, C., & Barbosa, F. K. B. 2006, MNRAS, 373, 2

Roberts, D. A., Yusef-Zadeh, F., & Goss, W. M. 1996, ApJ, 459, 627

Rusli, S. P., Thomas, J., Erwin, P., et al. 2011, MNRAS, 410, 1223

Rusli, S. P., Thomas, J., Saglia, R. P., et al. 2013, AJ, 146, 45

Sault, R. J., Teuben, P. J., & Wright, M. C. H. 1995, Astronomical Data Analysis Software and Systems IV, 77, 433

Scharwächter, J., Combes, F., Salomé, P., Sun, M., & Krips, M. 2016, MNRAS, 457, 4272

Schenker, M. A., Robertson, B. E., Ellis, R. S., et al. 2013, ApJ, 768, 196

Schiminovich, D., Ilbert, O., Arnouts, S., et al. 2005, ApJ, 619, L47

Schwarzschild, M. 1979, ApJ, 232, 236

Serabyn, E., Lacy, J. H., Townes, C. H., & Bharat, R. 1988, ApJ, 326, 171

Shapiro, K. L., Cappellari, M., de Zeeuw, T., et al. 2006, MNRAS, 370, 559

Shen, Y., Greene, J. E., Strauss, M. A., Richards, G. T., & Schneider, D. P. 2008, ApJ, 680, 169-190

Shen, Y., & Liu, X. 2012, ApJ, 753, 125

Sheth, K., Regan, M., Hinz, J. L., et al. 2010, PASP, 122, 1397

Shields, J. C., Rix, H.-W., Sarzi, M., et al. 2007, ApJ, 654, 125

Sijacki, D., Springel, V., Di Matteo, T., & Hernquist, L. 2007, MNRAS, 380, 877

Silk, J., & Rees, M. J. 1998, A&A, 331, L1

Siopis, C., Gebhardt, K., Lauer, T. R., et al. 2009, ApJ, 693, 946

Smajić, S., Moser, L., Eckart, A., et al. 2015, A&A, 583, A104

Somerville, R. S., & Davé, R. 2015, ARA&A, 53, 51

Sorce, J. G., Tully, R. B., Courtois, H. M., et al. 2014, MNRAS, 444, 527

Springel, V., White, S. D. M., Jenkins, A., et al. 2005, Nat, 435, 629

Springob, C. M., Masters, K. L., Haynes, M. P., Giovanelli, R., & Marinoni, C. 2007, ApJS, 172, 599

Steinhauser, D., Schindler, S., & Springel, V. 2016, A&A, 591, A51

Storchi-Bergmann, T., Baldwin, J. A., & Wilson, A. S. 1993, ApJ, 410, L11

Storchi-Bergmann, T., Nemmen da Silva, R., Eracleous, M., et al. 2003, ApJ, 598, 956

Sulentic, J. W., Bachev, R., Marziani, P., Negrete, C. A., & Dultzin, D. 2007, ApJ, 666, 757

Sun, M., Donahue, M., & Voit, G. M. 2007, ApJ, 671, 190

Takeuchi, T. T., Yoshikawa, K., & Ishii, T. T. 2003, ApJ, 587, L89

Tamura, Y., Oguri, M., Iono, D., et al. 2015, PASJ, 67, 72

Tecce, T. E., Cora, S. A., Tissera, P. B., Abadi, M. G., & Lagos, C. D. P. 2010, MNRAS, 408, 2008

Thatte, D., & et al. 2009, NICMOS Data Handbook, HST Data Handbooks,

Theureau, G., Hanski, M. O., Coudreau, N., Hallet, N., & Martin, J.-M. 2007, A&A, 465, 71

Tortora, C., Napolitano, N. R., Romanowsky, A. J., et al. 2011, MNRAS, 418, 1557

Trakhtenbrot, B., & Netzer, H. 2012, MNRAS, 427, 3081

Tremaine, S., Gebhardt, K., Bender, R., et al. 2002, ApJ, 574, 740

Tully, R. B. 1988, Nearby Galaxies Catalog (Cambridge: Cambridge University Press)

Tully, R. B., Courtois, H. M., Dolphin, A. E., et al. 2013, AJ, 146, 86

Valluri, M., Ferrarese, L., Merritt, D., & Joseph, C. L. 2005, ApJ, 628, 137

van den Bosch, R. C. E., van de Ven, G., Verolme, E. K., Cappellari, M., & de Zeeuw, P. T. 2008, MNRAS, 385, 647

van den Bosch, R. C. E., & de Zeeuw, P. T. 2010, MNRAS, 401, 1770

van den Bosch, R. C. E., Gebhardt, K., Gültekin, K., et al. 2012, Nat, 491, 729

van den Bosch, R. C. E., Greene, J. E., Braatz, J. A., Constantin, A., & Kuo, C.-Y. 2016, ApJ, 819, 11

van den Bosch, R. 2016, arXiv:1606.01246

van der Marel, R. P., & van den Bosch, F. C. 1998, AJ, 116, 2220

Verdoes Kleijn, G. A., van der Marel, R. P., de Zeeuw, P. T., Noel-Storr, J., & Baum, S. A. 2002, AJ, 124, 2524

Vestergaard, M. 2002, ApJ, 571, 733

Vollmer, B., Braine, J., Combes, F., & Sofue, Y. 2005, A&A, 441, 473

Walsh, J. L., Barth, A. J., & Sarzi, M. 2010, ApJ, 721, 762

Walsh, J. L., van den Bosch, R. C. E., Barth, A. J., & Sarzi, M. 2012, ApJ, 753, 79

Walsh, J. L., Barth, A. J., Ho, L. C., & Sarzi, M. 2013, ApJ, 770, 86

Walsh, J. L., van den Bosch, R. C. E., Gebhardt, K., et al. 2015, ApJ, 808, 183

White, S. D. M., & Frenk, C. S. 1991, ApJ, 379, 52

White, S. D. M., & Rees, M. J. 1978, MNRAS, 183, 341

Willick, J. A., Courteau, S., Faber, S. M., et al. 1997, ApJS, 109, 333

Wong, K. C., Suyu, S. H., & Matsushita, S. 2015, ApJ, 811, 115

Wyder, T. K., & GALEX Science Team 2005, Bulletin of the American Astronomical Society, 37, 52.03

Young, L. M., Bureau, M., Davis, T. A., et al. 2011, MNRAS, 414, 940